UC Santa Barbara
UC Santa Barbara Electronic Theses and Dissertations

Title
Molecular beam epitaxy of wide-band gap perovskiteoxides: (Ba, Sr)TiO3 and BaSnO3

Permalink
https://escholarship.org/uc/item/3dt7q9xs

Author
Freeze, Christopher R

Publication Date
2019

Peer reviewed|Thesis/dissertation

eScholarship.org Powered by the California Digital Library
University of California

UNIVERSITY OF CALIFORNIA

Santa Barbara

Molecular beam epitaxy of wide-band gap perovskite oxides: (Ba, Sr)TiO_3 and $BaSnO_3$

A dissertation submitted in partial satisfaction of the

requirements for the degree Doctor of Philosophy

in Materials

by

Christopher Robert Freeze

Committee in charge:

Professor Susanne Stemmer, Chair

Professor James S. Speck

Professor Christopher J. Palmstrøm

Professor Robert A. York

March 2019

The dissertation of Christopher Robert Freeze is approved.

____

James Speck

____

Christopher Palmstrøm

____

Robert York

____

Susanne Stemmer, Committee Chair

February 2019

ACKNOWLEDGEMENTS

I would like to thank my advisor, Prof. Stemmer, for her support and guidance throughout my doctoral work at UCSB. Under her direction, I have learned to design and perform meaningful studies and to critically analyze and interpret data. She has always been supportive, especially when things weren't working in lab. I am also grateful for the support of the rest of my committee – Profs. York, Speck, and Palmstrøm. I'm especially grateful for the collaboration with Cedric Meyers and Prof. York, and their patience with getting samples.

I greatly appreciate the colleagues I've had over the years, many of whom have become good friends as well. I thank the past group members who passed on their extensive MBE knowledge – Pouya Moetakef, Tyler Cain, Adam Kajdos, Clayton Jackson, and Santosh Raghavan. The resources of John English and Kurt Olsson have also been crucial for the success of my research in the MBE lab. The rest of the Stemmer Group has also supported me a great deal – Jack Zhang, Gift Chobpattana, Omor Shoron, Brandon Isaac, Patrick Marshall, Jinwoo Hwang, Honggyu Kim, Timo Schumann, Luca Galletti, Adam Hauser, Manik Goyal, David Kealhofer, Kaveh Ahadi, Salva Rezaie, Mandi Buffon, Tyler Pardue, Alex Lygo, Hanbyeol Jeong, and Raj Chaklashiya. I was also fortunate to enjoy the support of a number of fabulous interns and visitors to the group - Ryota Shimizu, Eric Rappeport, Chloe Lins, Tess Winkelhorst, Billy Strickland, and Yuntian Li.

While graduate school has been, at times, stressful and frustrating, it has largely been a positive experience in which I've learned and grown tremendously. That is

thanks primarily to the number of close friends I've made through the years (some of whom are mentioned above). I am especially grateful to Chris Pynn, Ryan Need, Megan Butala, Jackie Avallone, Elayne Thomas, Michael Gaultois, Doug Fabini, Emily Wonder, Nathan Almirall, Geneva Laurita, Mandi and Josh Buffon, Brenden McDearmon, Kate Marusak, and Krystian Kozek. I am also grateful for the great pleasure of singing in a barbershop-style quartet called The Acetones for a little over a year with an amazing group of ridiculous gentlemen – Tobias Brown Heft, Tom Cristiani, and Garth Ratliff. Finally, I would like to thank my family for their love and unwavering support throughout my (extended) education.

VITA OF CHRISTOPHER ROBERT FREEZE

December 2018

EDUCATION

2018 **Doctor of Philosophy** in Materials

University of California, Santa Barbara G.P.A: 3.79/4.0

2012 **Bachelor of Science** in Materials Science and Engineering, with Honors

North Carolina State University G.P.A: 4.0/4.0

PROFESSIONAL EMPLOYMENT

Process Engineering Intern May 16 – Aug. 10, 2011

RF Micro Devices, Inc: Greensboro, NC (now Qorvo)

Process/Quality Engineering Intern May 17 – Aug. 6, 2010

Unilin Flooring NC LLC: Thomasville, NC

Process/Quality Engineering Intern May 18 – July 31, 2009

Pine Hall Brick: Madison, NC

PUBLICATIONS

2016 **CR Freeze**, S Stemmer. Role of film stoichiometry and interface quality in the performance of $(Ba,Sr)TiO_3$ tunable capacitors with high figures of merit. *Applied Physics Letters* 109 (19) 192904.

2017 CJG Meyers, **CR Freeze**, S Stemmer, RA York. Effect of BST film thickness on the performance of tunable interdigital capacitors grown by MBE. *Applied Physics Letters* 111 (26) 262902.

2017 OF Shoron, S Raghavan, **CR Freeze**, S Stemmer. $BaTiO_3/SrTiO_3$ heterostructures for ferroelectric field effect transistors. *Applied Physics Letters* 110 (23) 232902.

2016 L Bjaalie, A Azcatl, S McDonnell, **CR Freeze**, S Stemmer, RM Wallace, CG Van de Walle. Band alignments between $SmTiO_3$, $GdTiO_3$, and $SrTiO_3$. *Journal of Vacuum Science & Technology A: Vacuum, Surfaces, and Films* 34 (6) 061102.

2016 CJG Meyers, **CR Freeze**, S Stemmer, RA York. $(Ba,Sr)TiO_3$ tunable capacitors with RF commutation quality factors exceeding 6000. *Applied Physics Letters* 109 (11) 112902.

2015 E Mikheev, **CR Freeze**, BJ Isaac, TA Cain, S Stemmer. Separation of transport lifetimes in $SrTiO_3$-based two-dimensional electron liquids. *Physical Review B* 91 (16), 165125

2014 CA Jackson, JY Zhang, **CR Freeze**, S Stemmer. Quantum critical behavior in confined $SrTiO_3$ quantum wells embedded in antiferromagnetic $SmTiO_3$. *Nature Communications* 5, 4258.

2013 **CR Freeze**, X Ji, AI Kingon, DL Irving. Impact of Joule heating, roughness, and contaminants on the relative hardness of polycrystalline gold. *Journal of Physics: Condensed Matter* 25 (47) 472202.

CONFERENCE PRESENTATIONS

2017 Optimizing the performance of $(Ba,Sr)TiO_3$ tunable capacitors for high figures of merit. *International Meeting on Ferroelectricity*. San Antonio, Texas. Oral presentation.

2017 Role of stoichiometry and interface quality in the performance of $(Ba,Sr)TiO_3$ tunable capacitors with high figures of merit. *International Conference on Electroceramics*. Nagoya, Japan. Oral presentation.

2011 The Role of Trapped Contaminant Pockets in the Degradation of Ohmic Contact in RF-MEMS Switches. *Fall Meeting of the Materials Research Society*. Boston, MA. Poster.

2011 Designing Energy Efficient Wireless Communications Devices Through Multiscale Simulation. *ACC Meeting of the Minds Conference*. Coral Gables, FL. Poster.

2010 The Role of Contaminant Layers in the Degradation of Ohmic RF-MEMS Contacts. *Fall Meeting of the Materials Research Society*. Boston, MA. Poster.

AWARDS

2012 National Defense Science and Engineering Graduate (NDSEG) Fellowship Recipient

2017 DowMI/MRL Travel Fellowship

2010, 2011 Office of Undergraduate Research – Undergraduate Research Award

ABSTRACT

Molecular beam epitaxy of wide-band gap perovskiteoxides: (Ba, Sr)TiO_3 and $BaSnO_3$

by

Christopher Robert Freeze

Perovskite oxides have long been lauded for their array of technologically useful properties, along with the promise of monolithic integration due to their compatible structure. Despite this potential, few real-world applications have yet to make it to market. This work aims to demonstrate the capabilities of the perovskite family of materials through two main applications – a tunable dielectric in the radio frequency regime and a high-power-density channel material for power switching. These capabilities are largely enabled thanks to the high-quality films grown by molecular beam epitaxy (MBE).

$Ba_xSr_{1-x}TiO_3$ (BST) is a ferroelectric material with a Curie temperature tuned by the composition *x*. It has been extensively investigated as a tunable dielectric material for devices such as phase shifters, tunable antennas, and matching networks. Despite decades of work, BST grown by other methods cannot compete with the extremely high performance of MBE-grown material. This thesis considers which aspects of the MBE-grown material are most critical for this performance increase.

While extreme charge density beyond 10^{20} cm^{-3} and charge modulation above 10^{14} cm^{-2} have been achieved in oxide systems, the low mobilities of most oxides at room

temperature has limited their utility in power-switching applications. A relatively new system, $BaSnO_3$, shows great promise for this purpose, with bulk mobility above 300 $cm^2/V\cdot s$ at carrier densities of 8×10^{19} cm^{-3}. This work discusses continued efforts to understand the growth of $BaSnO_3$ by MBE. The goal is to leverage this understanding to enhance thin-film mobility and control doping to enable high-power transistors, which may even outperform state-of-the-art GaN technologies. To that end, heterostructures with perovskite titanate top gates are investigated for modulation doping and gating.

TABLE OF CONTENTS

Acknowledgements iii

Vita of Christopher Robert Freeze v

Abstract viii

Table of Contents x

List of Figures xiii

List of Tables xxviii

1 Introduction and background 1

1.1 Ferroelectricity 3

1.1.1 Ferroelectrics as tunable dielectrics 5

1.2 Previous work on BST 12

1.2.1 Device design types 14

1.2.2 Device properties made with other growth techniques 19

1.2.3 Known performance limitations 21

1.2.4 Initial efforts with MBE-grown BST 25

1.2.5 Stabilizing the (**001**) Pt surface 26

1.3 Transport in oxides 29

1.3.1 Electrical properties of $BaSnO_3$ 30

1.3.2 Mobility limiting mechanisms 33

1.3.3 Measuring mobility 38

1.3.4 Sources of error in Hall mobility measurements 40

1.3.5 Requirements for realizing all-oxide transistors 47

2 Growth, characterization, and fabrication methodologies 55

2.1 Hybrid MBE for growth of titanates 56

2.2 Parallel-plate device fabrication and characterization 59

2.3 Selecting source material for growth of stannates 60

3 Enhancing performance of $Ba_xSr_{1-x}TiO_3$ Tunable capacitors 66

3.1 Controlling composition of $Ba_xSr_{1-x}TiO_3$ by MBE 67

3.2 *A*:*B* site stoichiometry and device performance 71

3.2.1 Verification of extraordinary quality factors 76

3.3 Improving the interface between BST and top contacts 78

3.3.1 Effects of interface cleanliness on quality factor 80

3.3.2 The role of interfacial capacitance on tunability 80

3.3.3 Field dependence of *Q*, and the dip at low bias 86

3.4 Device Leakage 90

3.5 Extrinsic factors from device design 91

3.5.1 Calculating series resistance 92

3.5.2 Device size effects (*P*/*A*) 94

3.6 BST on oxide substrates for interdigitated devices 108

3.7 Conclusions 115

4 Progress in thin-film growth of degenerately-doped $BaSnO_3$ 117

4.1 Controlling growth rate 118

4.2 Identifying cation stoichiometry by SnO_x/Ba Ratio 120

4.3 Separating effects of thickness and stoichiometry 124

4.4 Structural Quality 128

4.4.1 Using rocking curves to measure structural quality 132

4.4.2 Deviation in lattice constant from bulk 134

4.5 Changing doped thickness with constant total thickness 136

4.6 Strain compensation in $BaSnO_3$ on $DyScO_3$ 140

4.7 Variations in growth rate within a single growth 144

4.8 Inconsistency and non-uniformity in Hall measurements.............. 144

4.9 Conclusions 146

5 Heterostructures with $BaSnO_3$ for charge modulation/gating 148

5.1 Attempts to modulation dope $BaSnO_3$ with La:$SrTiO_3$.....................149

5.2 Heterostructures with $BaTiO_3$ for gating 152

5.3 Conclusions 159

6 Summary and future directions 161

6.1 Summary of BST varactor work 161

6.1.1 Designing high-frequency parallel plate capacitors....................162

6.2 Summary of $BaSnO_3$ work 163

6.2.1 Consistency of $BaSnO_3$ growths 164

6.2.2 Buffer layers to reduce misfits in and $BaSnO_3$.............................165

6.2.3 $SrSnO_3$ buffers for modulation doping $BaSnO_3$...........................166

Appendix A: XRD fitting in MATLAB 169

References..176

LIST OF FIGURES

Figure 1-1: Cubic perovskite crystal structure. 2

Figure 1-2: Free energy plot as a function of polarization for a ferroelectric material. As temperature is reduced ($T_2 \rightarrow T_1 \rightarrow T_C \rightarrow T_0$), a spontaneous polarization eventually occurs in the system. Reprinted under CC BY-NC-SA 3.0 from [C. L. Wang, in *Ferroelectrics*, edited by I. Coondoo, InTech 2010]. (Ref. [4]) 4

Figure 1-3: Plot of the temperature dependence of the dielectric constant for $Ba_xSr_{1-x}TiO_3$ for ceramic materials with different Ba concentration *x*. Reprinted by permission from Springer Nature Customer Service Centre GmbH: Springer "Ferroelectric Materials for Microwave Tunable Applications," A. K. Tagantsev, V. O. Sherman, K. F. Astafiev, J. Venkatesh, and N. Setter, 2003. (Ref. [12]) 5

Figure 1-4: Comparison of ideal and real capacitors, showing the introduction of a parasitic resistance for the real capacitor, which can be measured by the angle δ. 8

Figure 1-5: $Ba_xSr_{1-x}TiO_3$ lattice constant as a function of the Ba composition, *x*. (Red from Ref. [11], yellow from Ref. [33]) 14

Figure 1-6: Diagram showing the interdigitated capacitor a) structure and b) how the applied bias generates a field within the tunable material. 15

Figure 1-7: Lattice constants of commercially-available substrates that may be appropriate for use in the growth of BST. For orthorhombic crystal structures, the pseudocubic lattice constant is shown. 16

Figure 1-8: Parallel place capacitor layout showing a) cross-section and b) top-down views. Important parameters in device design geometry are highlighted in Figure 1-8b. 18

Figure 1-9: Summary of BST device properties shown in the literature review in Ref. [48]. The green area demonstrates the desired device properties to displace current technologies. 20

Figure 1-10: A summary of intrinsic loss mechanisms is shown in (a) with three-quantum (1), four-quantum (2), and quasi-Debye (3) loss. Γ_0 and Ω_0 are the soft-mode phonon frequency and damping, respectively. Panel (a) reprinted from [K. F. Astafiev, A. K. Tagantsev, and N. Setter, "Quasi-Debye microwave loss as an intrinsic limitation of microwave performance of tunable components based on $SrTiO_3$ and $Ba_xSr_{1-x}TiO_3$ ferroelectrics," *J. Appl. Phys.*, vol. 97, no. 1, p. 014106, Dec. 2005.], with the permission of AIP Publishing. (Ref. [20]) b) Calculations of quasi-Debye loss at 10 GHz are shown as a function of field for BST (x = 0.6) at room temperature, and for $SrTiO_3$ at 80 K. (Plotted from calculations in Ref. [20]) 23

Figure 1-11: General shape for measured *Q* as a function of frequency for real parallel-plate capacitors (a). Regions I and III are limited by extrinsic device parameters (leakage and series resistance, respectively). Region II is limited by material parameters (intrinsic and extrinsic). The equivalent circuits are shown for b) region I (where series resistance has a negligible contribution) and c) region III (where parallel conductance is negligible). 24

Figure 1-12: RHEED pattern (above) and AFM (below) for 100 nm Pt (001) films on $SrTiO_3$ (001) substrates heated in the MBE to the indicated temperatures.27

Figure 1-13: Wide-angle x-ray diffraction patterns for the Pt films heated in Figure 1-12. 27

Figure 1-14: RHEED pattern from the 100 reflection of 100 nm Pt (001) films on $SrTiO_3$ (001) heated to the indicated temperatures under an oxygen plasma flow of 3×10^{-6} Torr. 28

Figure 1-15: Post-anneal atomic force microscope image of the surface of a 100 nm Pt (001) film on $SrTiO_3$ (001) heated to 810 °C under oxygen plasma. 28

Figure 1-16: Wide-angle x-ray diffraction patterns for the 100 nm Pt (001) films on $SrTiO_3$ (001) annealed in MBE under oxygen plasma flow. 29

Figure 1-17: Summary of single-crystal (and some thin-film) mobilities for La:$BaSnO_3$. "Ref. 28" refers to Ref. [74] in this work. "Reprinted figure with permission from [H. J. Kim, U. Kim, T. H. Kim, J. Kim, H. M. Kim, B. G. Jeon, W. J. Lee, H. S. Mun, K. T. Hong, J. Yu, K. Char, and K. H. Kim, Physical Review B, vol. 86, no. 16, 2012.] © 2012 by the American Physical Society. (Ref. [75]) 31

Figure 1-18: Diagram a) of van der Pauw sample geometry for measuring resistivity and Hall resistance in thin films using ohmic contacts labeled 1, 2, 3, and 4. Longitudinal resistance can be measured as shown in (b) for $R_{12,34}$, while Hall resistance can be measured as shown in (c) for $R_{13,24}$ with magnetic field out-of-plane. 39

Figure 1-19: a) Maximal error shown for the convergence of the Newton-Raphson algorithm, and b) the maximal error in the mobility measurement for selected samples..42

Figure 1-20: a) Fits to the antisymmetrized Hall resistance for two 90° rotations on each sample. Using the standard error in fits to the slope, error in mobility is shown in b) as a 95% confidence interval. 43

Figure 1-21: Correction factors to the sheet resistance are shown in a) for square and triangular contacts for contacts with size δ and sample of size l. Reprinted from [*Solid-State Electronics* vol. 17, issue 12, R Chwang, B J Smith, C R Crowell, "Contact size effects on the van der Pauw method for resistivity and Hall coefficient measurement," pp 1217-1227, Copyright 1974], with permission from Elsevier. (Ref. [90]) The effect of the sheet resistivity correction on measured mobilities is shown in b) with δ/l = 1/6. 45

Figure 1-22: Correction factors to the Hall voltage are shown in a) for triangular contacts having contacts of size δ and sample side length l. Reprinted from [*Solid-State Electronics* vol. 17, issue 12, R Chwang, B J Smith, C R Crowell, "Contact size effects on the van der Pauw method for resistivity and Hall coefficient measurement," pp 1217-1227, Copyright 1974], with permission from Elsevier. (Ref. [90]) The effect of the Hall voltage correction on measured mobilities is shown in b) with δ/l = 3/16. Note that the error for square contacts (which are used in these measurements) is actually higher than shown...47

Figure 1-23: Device simulations of heterostructure field transistors with a) a high-κ dielectric constant (e.g. $BaTiO_3$) gate and b) a low-κ dielectric constant gate. Simulation results show c) net sheet charge distribution and d) lateral electric field profiles within the device [92]. 50

Figure 1-24: Structure for calculating modulation doping with a δ-doped injection layer (a). The doping layer ($SrTiO_3$) is δ-doped at d_s from the interface with the bottom layer ($BaSnO_3$) as a result of conduction band offset ΔE_c. Charge profiles (b) and partial band diagram (c) are shown for the resulting structure [93]. Reprinted by permission from Springer Nature Customer Service Centre GmbH: Springer *Semiconductor Device Physics and Design* by Umesh K. Mishra, Jasprit Singh, 2007. 51

Figure 1-25: Calculated results for the amount of confinement of the 2DEG $(eVdi -)$ as a function of the conduction band offset, ΔE_C and the 2DEG sheet charge density. For a well depth of 0 eV or less, there is no carrier confinement within the $BaSnO_3$ layer. 53

Figure 1-26: Degree of carrier confinement in $BaSnO_3$ as a function of the conduction band offsets for various sheet carrier densities. For the calculations, carriers were placed 2 nm from the $BaSnO_3$ interface. Calculated band offsets are indicated with arrows, and results for selected polar interfaces are also shown. Reprinted from [K. Krishnaswamy, L. Bjaalie, B. Himmetoglu, A. Janotti, L. Gordon, and C. G. Van de Walle, "$BaSnO_3$ as a channel material in perovskite oxide heterostructures," *Appied*

Physics Letters, vol. 108, no. 8, p. 083501, 2016.], with the permission of AIP Publishing. (Ref. [94]) 54

Figure 2-1: Schematic of the MBE chambers used in this work. 56

Figure 2-2: Estimated MBE growth window for the growth of GaAs from solid Ga and cracked As. Each line indicates an equilibrium for the reaction shown. Plot recreated from Ref. [98] 57

Figure 2-3: Estimated MBE growth window for the growth of $SrTiO_3$ from solid Sr and Ti sources. Each line indicates an equilibrium for the reaction shown. Plot recreated from Ref. [100] 58

Figure 2-4: Vapor pressures of SnO_2 and its decomposition biproducts. Figure from [H. Paik, Z. Chen, E. Lochocki, A. Seidner H., A. Verma, N. Tanen, J. Park, M. Uchida, S. Shang, B.-C. Zhou, M. Brützam, R. Uecker, Z.-K. Liu, D. Jena, K. M. Shen, D. A. Muller, and D. G. Schlom, "Supplementary material: Adsorption-controlled growth of La-doped $BaSnO_3$ by molecular-beam epitaxy," *APL Materials*, vol. 5, no. 11, p. 116107, 2017.] is licensed under CC BY 4.0. (Ref. [76]) 63

Figure 3-1: Strained out-of-plane lattice constants (determined by XRD) for ~60 nm BST grown on $SrTiO_3$ (001) with Ba content of a) 12%, b) 46%, c) ~60%, and d) ~65%. At each composition, *A*:*B*-site flux ratio is varied. 69

Figure 3-2: Reciprocal space map of the (103) reflection of a 60 nm $Ba_{0.6}Sr_{0.4}TiO_3$ film on $SrTiO_3$ demonstrating the film is fully strained to the substrate in-plane lattice constant 71

Figure 3-3: Measured lattice constant from XRD as a function of flux ratio for BST with x = 0.3 on a) $SrTiO_3$ (001) (~60 nm thick) and on b) 100 nm Pt (001)/$SrTiO_3$ (001) (~280 nm thick). 72

Figure 3-4: RHEED and atomic force micrographs of the BST series (x ~ 0.3) grown on 100 nm Pt (001)/$SrTiO_3$. AFM was taken after the post-growth oxygen anneal. 74

Figure 3-5: Q as a function of frequency for 45 × 45 μm^2 devices with sputtered top contacts under no DC bias. Measured data is shown with a solid line, while the dotted line shows calculated Q from eq. (3-5). 75

Figure 3-6: Measured Q as a function of applied field for (a) e-beam-deposited Pt top contacts and (b) sputtered top contacts at 1 MHz. Negative field is plotted since application of bias in this direction probes the breakdown from injection by the top interface. While zero-field Q is highest for stoichiometric samples (36, 40), A-rich stoichiometries can be biased further. 76

Figure 3-7: Measured capacitance as a function of frequency for films with different stoichiometry. Fitting to eq. (3-4), we can calculate expected Q. 78

Figure 3-8: Tunability measured in the dielectric constant for devices with stoichiometric BST at 1 MHz. Solid lines indicate measured data, while dotted lines show fits to tunable capacitance as described by the empirical relation given in eq. (1-4) and (3-8). Reprinted from [C. R. Freeze and S. Stemmer, "Role of film stoichiometry and interface quality in the performance of (Ba,Sr)TiO_3 tunable capacitors with high figures of merit," *Applied Physics Letters*, vol. 109, no. 19, p. 192904, 2016.], with the permission of AIP Publishing. 82

Figure 3-9: Tunability measured in the dielectric constant for devices with stoichiometric BST at 1 MHz. Solid lines indicate measured data, while dotted lines show fits to tunable capacitance as described by Landau-Devonshire-Ginzburg theory in eq. (1-5). Reprinted from [C. R. Freeze and S. Stemmer, "Role of film stoichiometry and interface quality in the performance of (Ba,Sr)TiO_3 tunable capacitors with high figures of merit," *Applied Physics Letters*, vol. 109, no. 19, p. 192904, 2016.], with the permission of AIP Publishing. 85

Figure 3-10: Q as a function of bias for samples with flux ratios of 32, 36, and 40 at f = 1 MHz. In these sweeps, AC probe amplitude is varied from as low as 25 mV to 500 mV. Scans are typically done with V_{AC} = 50 mV... 88

Figure 3-11: Dielectric constant as a function of applied DC field measured at 1 MHz for samples with varying cation stoichiometry. 89

Figure 3-12: Parallel conductance for measured from 0 V to 13 V (only odd integers and zero shown). The device measured is the sample with flux ratio of 36 with sputtered top contacts. 91

Figure 3-13: Qs as a function of frequency shown in the high-frequency range, where series resistance dominates the device properties..................................... 92

Figure 3-14: Equivalent circuit model for the periphery-dependent leakage described by 95

Figure 3-15: Effects of device periphery on Q (at 1 MHz) for $Ba_{0.5}Sr_{0.5}TiO_3$ parallel plate capacitor devices grown by Nadia Pervez ranging in size from 12×12 μm^2 to 45×45 μm^2. L_m indicates the spacing between the edge of the top contact and the etched

mesa edge, or "mesa ledge width" (as depicted in Figure 1-8b). Reprinted with permission from [N. K. Pervez and R. A. York, "Geometry-Dependent Quality Factors in $Ba_{0.5}Sr_{0.5}TiO_3$ Parallel-Plate Capacitors," *IEEE Transactions on Microwave Theory and Techniques*, vol. 55, no. 2, pp. 410–417, 2007.] © 2007 IEEE. (Ref. [127]) 96

Figure 3-16: Wide-angle XRD demonstrating the presence of additional orientations in the BST/Pt films after BST growth. The new sample has a re-optimized Pt (001) back contact (on an $SrTiO_3$ substrate) to reduce the off-orientation BST grown on it. The previous sample is from the series discussed earlier with a TTIP/(Sr+Ba) flux ratio of 36. 97

Figure 3-17: Atomic force micrographs of the BST sample surface used to investigate how the degree of etch damage effects the device-size effects described in eq. (3-10). 98

Figure 3-18: Plots of Q as a function of frequency for parallel-plate devices of varying size (in μm) with mesas etched by a) Ar ion mill and b) 1:20 $HF:H_2O$. 99

Figure 3-19: Measured Q (at 1 MHz) as a function of the ratio of perimeter length to contact area for devices fab ricated with the BST mesa etched by either a) ion milling or b) wet etch with 1:20 $HF:H_2O$. Fits to eq. (3-10) are also plotted for both sets. 100

Figure 3-20: Impedance resolution limits to Keysight 4294A Impedance analyzer, as given in the user manual. Lines are drawn which show the approximate impedances for 12×12 μm^2 and 45×45 μm^2 BST parallel plate capacitors [128]. 101

Figure 3-21: Q calculated at 1 MHz using fits to capacitance as a function of frequency as described by eq. (3-4) and (3-5). A fit to eq. (3-10) is plotted for the set with the ion-milled mesa, along with fitted parameters. Error bars are shown according to a 95% confidence interval for the fitted value of n for eq. (3-4)................. 102

Figure 3-22: Capacitance density (at 1 MHz) as a function of perimeter length to device area for devices with mesas etched by ion mill and wet etch processes. ..103

Figure 3-23: Fits (gray dashed lines) to the measured (solid lines) capacitance as a function of applied DC field for different device sizes without including a fringing capacitance. First V_2 (here, 0.400 MV/cm) is fitted to the 45 × 45 μm² device, and this value is used for all sizes. 105

Figure 3-24: Fits to tunable capacitance including a fringing capacitance term according to eq. (3-11) (left). This fit uses the same V_2 (0.400 MV/cm, fitted to the 45 × 45 μm² device) as in Figure 3-23). Fitted fringing capacitance is shown on the right for each device... 106

Figure 3-25: Fits to tunable capacitance including a fringing capacitance term according to eq. (3-11) (left). This fit set C_{max} to the peak value for each device but allowed C_f and V_2 to vary (V_2 still remains the same for all devices). Fringing capacitance is shown on the right. 107

Figure 3-26: Lattice parameters of commercially-available substrates, compared with the range of possible $Ba_xSr_{1-x}TiO_3$ lattice constant. Pseudocubic lattice constants are shown for non-cubic crystal structures (averaging $d110$ and $d110$). 109

Figure 3-27: Atomic force microscopy images of 300 nm $Ba_{0.12}Sr_{0.88}TiO_3$ grown on oxide substrates a) $DyScO_3$ (110) and b) $LaAlO_3$ (001). (c) demonstrates how film cracking and delamination causes the raised features seen in (a)............ 110

Figure 3-28: Atomic force micrographs of (300 nm thick) BST surfaces grown on a) $LaAlO_3$ (x = 0.29) and b) $DyScO_3$ (110) (x = 0.46).................................... 111

Figure 3-29: Reciprocal space map of a) 300 nm BST (x = 0.29) grown on $LaAlO_3$, demonstrating a fully-relaxed film lattice constant and b) 300 nm BST (x = 0.46) grown on $DyScO_3$ (110). The cubic condition (in-plane spacing = out-of-plane spacing) is indicated with a black line. 112

Figure 3-30: X-ray diffraction pattern (a) and atomic force micrograph (b) of 150 nm of BST (x = 0.29) on $LaAlO_3$ (001)...113

Figure 3-31: A demonstration a) of how a Soller slit used in powder x-ray diffraction reduces axial divergence, and b) how the Soller slit improves the diffraction pattern when multiple crystal orientations are present. In b), data are represented by squares, a symmetric pseudo-Voigt profile by a dashed line, and an asymmetric profile by a solid line. (b) reproduced under open access from [L. W. Finger, D. E. Cox, and A. P. Jephcoat, "A correction for powder diffraction peak asymmetry due to axial divergence," *Journal of Applied Crystallography*, vol. 27, no. 6, pp. 892–900, 1994.]. (Ref. [129])... 114

Figure 4-1: $BaSnO_3$ growth rate as a function of a) Ba flux and b) SnO_2 flux for samples grown on $DyScO_3$ with substrate heater power of 432 or 456 W. The growth rate increases linearly with Ba flux, and it does not change systematically with SnO_x

flux. While most samples were grown for 90 minutes, samples grown for 150 and 210 minutes are also marked (indicated in the legend). Samples were grown and measured by Santosh Raghavan and Omor Shoron. 119

Figure 4-2: Electron mobility of $BaSnO_3$ on $DyScO_3$ (001) as a function of a) SnO_x/Ba flux ratio and b) Ba flux with a substrate output power of 456 W. Note that SnO_x flux is not held constant for these growths. Selected samples grown with higher SnO_x flux are highlighted in both (High ~ 2.5×10^{-6}, Low ~ 5×10^{-7}). Samples were grown and measured by Santosh Raghavan and Omor Shoron. 123

Figure 4-3: Sample thickness and electron mobility as a function of flux ratio for $BaSnO_3$ samples grown on $DyScO_3$ (001) by Santosh Raghavan and Omor Shoron.125

Figure 4-4: Mobility for the $BaSnO_3$ series grown attempting to keep thickness and doping constant. Ba-rich conditions are indicated by the blue shading. The sample denoted with a star had a lower thickness (see Figure 4-5), explaining a portion of the reduction in mobility. 126

Figure 4-5: Carrier density and total thickness for the $BaSnO_3$ series grown on at relatively consistent thickness and doping (grown on $DyScO_3$ (001)). The Ba-rich condition with low mobility (see Figure 4-4) is highlighted at the right in blue.127

Figure 4-6: X-ray diffraction of Ba-rich (blue), stoichiometric (green), and Sn-rich (red) $BaSnO_3$ on $SrTiO_3$. Samples grown and measured by Santosh Raghavan and Timo Schumann. 129

Figure 4-7: Wide-angle XRD scans of $BaSnO_3$ grown with near-constant thickness and doping. Samples within the growth window, as defined by mobility (see Figure

4-4), are shown in green. Unlabeled peaks are from the $DyScO_3$ substrate 002 and 004 reflections. 132

Figure 4-8: Rocking curve of $BaSnO_3$ (002) peaks for the growth series with thickness and doping held constant. Intensities shifted to have same peak intensity to facilitate comparison. 133

Figure 4-9: Plot showing the rocking curve width at 1/20th of the maximum for the rocking curves shown in Figure 4-8. 134

Figure 4-10: Lattice constant as a function of flux ratio for the growth series holding thickness and doping constant. The Ba-rich condition (determined from mobility) is shown in blue. The bulk value of 4.116 Å is indicated with the dashed line. 135

Figure 4-11: Out-of-plane lattice constant as measured by XRD and mobility as a function of flux ratio for various substrate temperatures. Samples grown and measured by Santosh Raghavan, Timo Schumann, and Omor Shoron. 136

Figure 4-12: Sample structures for investigating potential causes of reduced mobility for thin samples. 137

Figure 4-13: Variation of mobility and 2D carrier density based upon how much of the 60 nm $BaSnO_3$ film is doped. Doped film percentage based on growth times for UID and doped layers. The dashed line indicates the expected n_{2D} based on La content. 139

Figure 4-14: Plan-view transmission electron microscopy of 50 nm $BaSnO_3$ grown on $DyScO_3$ $(001)_o$. Dislocation cores are marked by white arrows. TEM courtesy of Honggyu Kim. 141

Figure 4-15: Cross-section transmission electron microscopy of 50 nm $BaSnO_3$ grown on $DyScO_3$ $(001)_o$. TEM courtesy of Honggyu Kim. 143

Figure 4-16: Asymmetry in the sheet resistance and Hall resistances for $BaSnO_3$ films on $DyScO_3$ (001). The 23.6 ratio sample with anisotropic $R_{longitudinal}$ is shown with hollow markers. 145

Figure 5-1: Atomic Force Microscopy images of multiple regions (a and b vs. c and d) of a $GdScO_3$/~25 nm $BaSnO_3$/~20 nm La:$SrTiO_3$ sample, demonstrating non-uniformity in the growth. There is also a large density of pinholes, and in some regions there appears to be cracking...152

Figure 5-2: Atomic force micrograph of the heterostructure with 20 nm $BaTiO_3$/30 nm $BaSnO_3$/$DyScO_3$. 154

Figure 5-3: X-ray diffraction pattern for the 20 nm $BaTiO_3$/30 nm $BaSnO_3$/$DyScO_3$ (001) heterostructure 154

Figure 5-4: Atomic force microscopy of a representative $BaTiO_3$/La:$BaSnO_3$/$DyScO_3$ heterostructure. $BaTiO_3$ thickness is 20 nm on ~60 nm of $BaSnO_3$..........156

Figure 5-5: Atomic force microscopy of a bare 60 nm $BaSnO_3$ film grown under the same conditions as the heterostructure shown in Figure 5-4. 157

Figure 5-6: Sample surface of 20 nm $BaTiO_3$ grown on previously measured La:$BaSnO_3$ films on $SrTiO_3$ substrates by atomic force microscopy............................158

Figure 5-7: X-ray diffraction patterns for $BaTiO_3$/La:$BaSnO_3$/$DyScO_3$ (top) and for $BaTiO_3$/La:$BaSnO_3$/$SrTiO_3$ (bottom) heterostructures. 159

Figure 6-1: Plan-view transmission electron microscopy (courtesy of Honggyu Kim) of a non-conductive La:$SrSnO_3$ film grown on $DyScO_3$ (110) by MBE. The micrograph presents an extremely high density of antiphase boundaries with significant disorder at the boundary..168

LIST OF TABLES

Table 1-1: Summary of loss mechanisms and how they scale with frequency and permittivity. 11

Table 1-2: Summary of Q-factors and dielectric constants for a variety of viable substrates for fabricating BST interdigitated capacitors [40]–[45]. 17

Table 3-1: Extracted exponent from fits to capacitance as a function of frequency for the stoichiometry series grown on Pt. 77

Table 3-2: Extracted material parameters and interfacial capacitances for the curves shown in Figure 3-8 and Figure 3-9. Also shown is the measured tunability of each device $n = CE = 0CE$ at a field of 0.25 MV/cm to demonstrate the impact of the interfacial capacitance. Reprinted from [C. R. Freeze and S. Stemmer, "Role of film stoichiometry and interface quality in the performance of $(Ba,Sr)TiO_3$ tunable capacitors with high figures of merit," *Applied Physics Letters*, vol. 109, no. 19, p. 192904, 2016.], with the permission of AIP Publishing. 86

Table 3-3: Extracted series resistance (R_s) for devices extracted from impedance analyzer measurements at high frequencies according to eq. (3-9) (measured in Ω). 93

1 INTRODUCTION AND BACKGROUND

Perovskite oxides, with chemical formula ABO_3, shown in Figure 1-1 (where *A* and *B* can be a variety of cations), contain an enormous breadth of material properties with relatively minor differences in crystal structure. Perovskites can be metals, semiconductors, band insulators, or Mott insulators. They can be nearly all forms of ferroelectric, magnetic, and superconducting. Most importantly, these properties can be tuned by simple substitution of the *A* and *B* sites.

$SrTiO_3$ represents the prototypical semiconducting perovskite, with cubic crystal structure (a = 3.905 Å) [1] and an indirect band gap of 3.2 eV [2]. Most properties of the perovskite structure are linked to the oxygen octahedron surrounding the *B*-site cation (as seen in Figure 1-1). As such, it is often constructive to compare the structure of perovskites with novel properties with that of cubic $SrTiO_3$. With a valence band largely

defined by the stable oxygen 2p orbital, the perovskite band gap can be tuned through substitution of the *B*-site [3]. For instance, in $SrTiO_3$, the valence band has largely Ti 3d character, while for the $SrZrO_3$, the higher energy Zr 4d orbital raises the conduction band minimum by 1.74 eV.

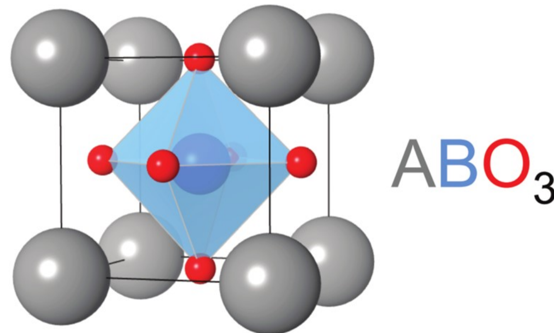

Figure 1-1: Cubic perovskite crystal structure.

Through substitution of the *A*-site species, the ionic size ratio can alter the perovskite structure to induce structural tilts and/or extensions to the reduce symmetry in the unit cell. This distortion can stabilize electric dipoles, leading to ferroelectricity [4]. The introduction of rotations changes the overlap between neighboring *B*-site electronic orbitals, effectively tuning bandwidth, which can enhance electron-electron correlations and create Mott insulators [5]. These Mott insulators can even be ferrimagnetic or antiferromagnetic [6]. There is even interest in perovskites for high-temperature superconductivity [7].

While the materials systems discussed in this work have similar structures and chemistries, the reasons for interest in them are quite varied. This chapter is broken down into a section on the physics required to understand each system, followed by a

discussion of previous works that have been done on each system, beginning with $Ba_xSr_{1-x}TiO_3$ for tunable dielectrics and ending with $BaSnO_3$ as a high-mobility oxide.

1.1 Ferroelectricity

Similar to ferromagnets which spontaneously form a magnetic dipole, ferroelectrics form a spontaneous *electrical* dipole below the material's Curie temperature, T_C. The magnitude and direction of this dipole are related to a distortion in the crystal structure, along with an associated phase transition. For most useful ferroelectrics, such as $PbZr_xTi_{1-x}O_3$ (PZT) and $BaTiO_3$ (BTO), this transition is first order [4]. Importantly, this phase transition breaks the crystals centrosymmetry since, by definition, a centrosymmetric crystal cannot be polar. By extension, the more general cases of piezoelectrics (dipole coupled to strain and temperature) and pyroelectrics (dipole coupled to temperature) also cannot be centrosymmetric.

Based on Landau theory, the free energy (ΔG) of a ferroelectric material without an applied electric field or stress can be written as a Taylor expansion in terms of the polarization, P [4]. For a ferroelectric transition with only one axis of polarization (e.g. cubic to tetragonal), the one-dimensional expression of the free energy is

$$\Delta G = \frac{1}{2}\alpha_0(T - T_0)P_x^2 + \frac{1}{4}\alpha_{11}P_x^4 + \frac{1}{6}\alpha_{111}P_x^6 \tag{1-1}$$

Figure 1-2 shows the shape of the free energy at different temperatures for a first order phase transition. Here, parameters were set as $\alpha_0 = 1$, $\alpha_{11} = -1$, $\alpha_{111} = 1$, and $T_0 = 0$ for simplicity. In this plot, there are 4 characteristic temperatures. The Curie-Weiss temperature can be accessed experimentally through

$$\epsilon_p = \frac{C}{T - T_0} \tag{1-2}$$

where C is the Curie-Weiss constant and ϵ_p is the dielectric constant of the paraelectric phase. T_0 is the temperature at which the system spontaneously transitions to the ferroelectric structure. T_C is the temperature at which the ferroelectric and paraelectric phases have the same free energy. The ferroelectric limit temperature, T_1, is upper limit where the ferroelectric phase is metastable, but the paraelectric phase is stable. Below T_2, the field-induced phase transition limit temperature, the ferroelectric structure can still be stabilized under the application of field, but it is unstable.

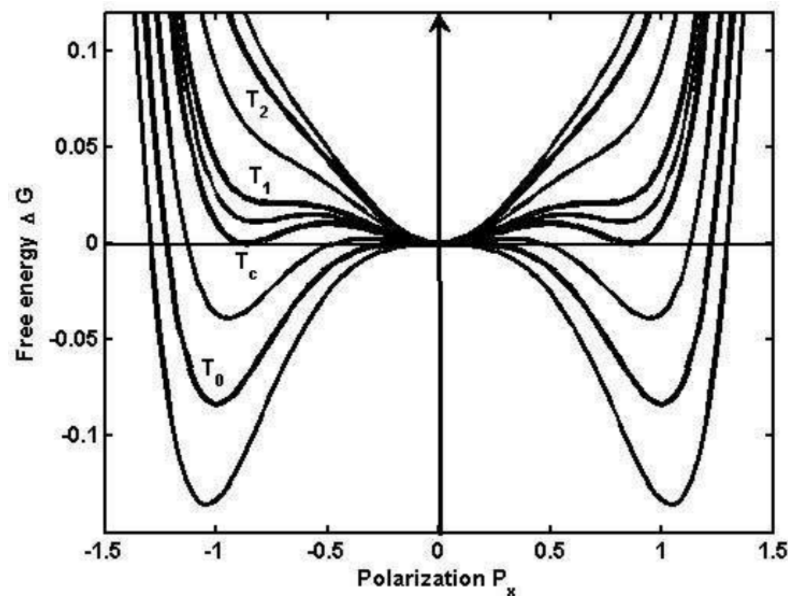

Figure 1-2: Free energy plot as a function of polarization for a ferroelectric material. As temperature is reduced ($T_2 \rightarrow T_1 \rightarrow T_C \rightarrow T_0$), a spontaneous polarization eventually occurs in the system. Reprinted under CC BY-NC-SA 3.0 from [C. L. Wang, in *Ferroelectrics*, edited by I. Coondoo, InTech 2010]. (Ref. [4])

As seen from eq. 1-2, the dielectric constant of the paraelectric phase diverges at T_0 (note though, that at T_0 the material is not in the paraelectric phase). For $BaTiO_3$, the

Curie temperature is 120 °C [8], while $SrTiO_3$ is an quantum paraelectric. This is s subset of incipient ferroelectrics where $T_C > 0$ K, but quantum fluctuations prevent order [9], [10]. By alloying $SrTiO_3$ and $BaTiO_3$ (to make $Ba_xSr_{1-x}TiO_3$, or BST), the temperature at which the dielectric constant diverges can be tuned as shown in Figure 1-3. BST has a Curie temperature at room temperature for a composition $x \sim 0.7$ [11].

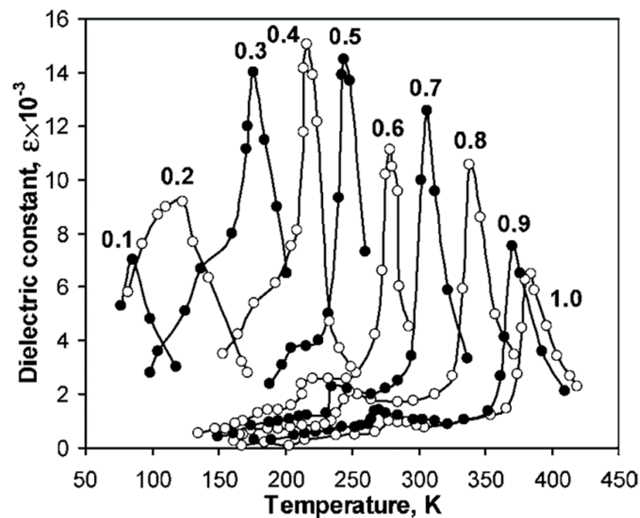

Figure 1-3: Plot of the temperature dependence of the dielectric constant for $Ba_xSr_{1-x}TiO_3$ for ceramic materials with different Ba concentration x. Reprinted by permission from Springer Nature Customer Service Centre GmbH: Springer "Ferroelectric Materials for Microwave Tunable Applications," A. K. Tagantsev, V. O. Sherman, K. F. Astafiev, J. Venkatesh, and N. Setter, 2003. (Ref. [12])

1.1.1 Ferroelectrics as tunable dielectrics

A material's dielectric constant is a measure of its ability to generate an internal dipole in response to an external field. In practical application, it is measured by the applying a small AC bias and measuring the the phase and magnitude of the current to calculate impedance. This is the basic operating principle of the impedance analyzer.

(At higher frequencies, e.g. above 100 MHz, a network analyzer must be used to measure reflection coefficients [12]) In the context of Figure 1-2, this small AC signal effectively provides a small excitation from the energy minimum, and the dielectric constant is a measure of how far the polarization can be switched from this small excitation. High above the Curie temperature, and far below the Curie temperature, this small excitation only sees a single, deep energy well, giving a small dielectric constant. However, near T_C, this well is relatively flat, and extremely high polarizations can be achieved with relatively little excitation. This yields the enormous dielectric constants seen near T_C.

By applying a comparatively large DC bias, a line (with slope proportional to the field strength) is added to the free energy plots in Figure 1-2. This external field effectively acts to modify the shape of the potential well. Since the far edges have slope far greater than can be induced by applied field (otherwise the crystal would be ripped apart), this field serves to effectively narrow the size of that well accessible to the small AC excitation, thereby suppressing the measured dielectric constant. It is this suppression that we call dielectric tunability:

$$n = \frac{\epsilon(0)}{\epsilon(E)} \quad (1\text{-}3)$$

For a tunability $n = 2$, for instance, this would imply that the applied DC field is large enough to suppress the dielectric constant to half the value at zero bias. These sorts of tunable dielectrics have attracted attention as variable capacitors at RF frequencies. Among the highest-performing candidates is the perovskite $Ba_xSr_{1-x}TiO_3$ (BST) [12]–[14]. A myriad of useful devices can be made with a tunable capacitor, including tunable

band pass filters [15], phase shifters [13], matching networks, and resonators [16]. This work will focus on the fundamental building block for all of these devices, which is the tunable capacitor.

1.1.1.1 Tunability relations

The field dependence of a tunable dielectric, like BST, is well described by the empirical relation:

$$\epsilon_B(E) = \frac{b}{\sqrt{a+E^2}} \tag{1-4}$$

where $\epsilon_B(E=0) = \frac{b}{\sqrt{a}}$ [17]. Here, ϵ_B is the dielectric constant of the tunable material, and b and a are temperature-dependent constants. While the simplistic model for tunable capacitance such as the one in eq. (1-4) is convenient for quick calculations, this nonlinearity can also be thermodynamically determined. This thermodynamic relation is derived from the third-order term in the polarization with applied field, or the Landau-Devonshire-Ginzburg (LDG) model [18]. Using only up to the third order term, the equation simplifies:

$$\epsilon(V) = \frac{\epsilon_{\max}}{2\cdot\cosh\left(\frac{2}{3}*\sinh^{-1}\left(2\cdot\frac{V}{V_2}\right)\right)-1} \tag{1-5}$$

Where $\epsilon_{\max}$ is the peak dielectric constant (i.e. at zero bias) and V_2 is the voltage required to achieve a capacitance tuned to half of the zero-field capacitance. According to this model, any additional series capacitance (such as stemming from an interface) should be incorporated into the model without modifying the general shape of the curve. Instead, $\epsilon_{\max}$ and V_2 are rescaled to accommodate the change.

1.1.1.2 Dielectric loss and its origins

Dielectric loss is a measure of how close a capacitor's behavior is to an ideal capacitor. For an ideal capacitor, the impedance lies directly along the reactive (imaginary) axis. However, any real-world capacitor also has additional series resistance, or parallel conductance, which contributes an additional real component to the impedance (Figure 1-4). To measure how closely a real capacitor behaves to an ideal capacitor, we consider the angle δ between the measured impedance and the imaginary axis. Dielectric loss is often reported as loss tangent, or tanδ, or its inverse – quality factor $Q = 1/\tan\delta$.

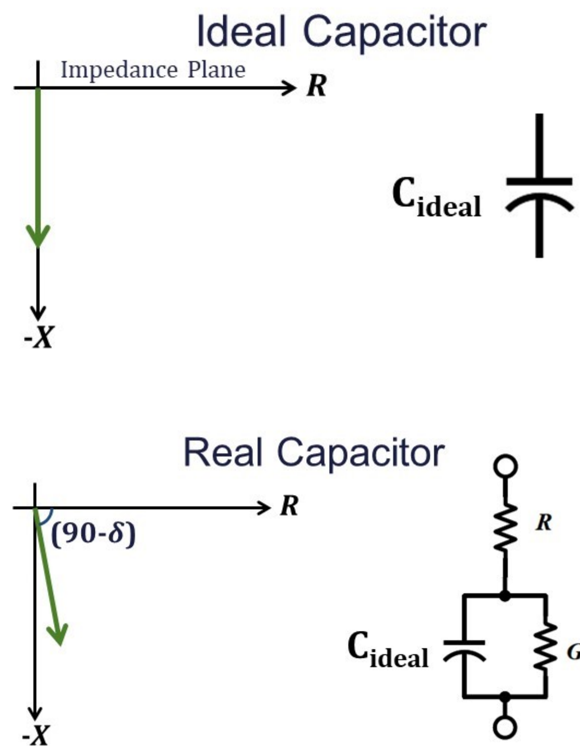

Figure 1-4: Comparison of ideal and real capacitors, showing the introduction of a parasitic resistance for the real capacitor, which can be measured by the angle δ.

Dielectric loss mechanisms can be grouped based on whether they are inherent to the material used (intrinsic) or dependent upon defects or other present in the material (extrinsic). A great deal of the analysis of loss is discussed in literature [12], [19], [20], but only a relatively small background will be covered here. Intrinsic loss stems from the interaction of the AC signal with phonons in the material. 3-quantum and 4-quantum mechanisms both involve the adsorption of an $\hbar\omega$ quantum by thermal phonons. The difference is that the 3-quantum involves two phonons of similar energy to satisfy conservation laws, where 4-quantum allows contributions from nearly the entire excited part of k-space.

The third intrinsic mechanism, quasi-Debye loss, stems from the time-dependent relaxation of the phonon distribution in non-centrosymmetric crystals. In these crystals and for small fields, phonon frequencies are roughly linear functions of electric field. As a result, the small signal amplitude can be enough to cause a shift in the equilibrium phonon distribution. This relaxation gives rise to loss in the same manner as the relaxation of a dipole distribution function gives rise to loss in the Debye theory [20]. It is important to note that even for ferroelectric crystals in their paraelectric phase (which have a center of symmetry), an applied electric bias is sufficient to break this symmetry [20]. It can be shown that for not too-large frequencies (i.e. below 100 GHz for $SrTiO_3$), the quasi-Debye contribution to the loss is

$$Q_{QD}(E_0) \;\propto\; \frac{1}{\omega * n_r} \tag{1-6}$$

As mentioned previously, extrinsic loss stems from defects present in imperfect material. One such case is that of charged defects. The applied AC field results in

oscillation of charged defects (acoustic waves) with the same frequency as the applied field. This loss mechanism can be approximated as

$$Q_{charge} \quad \propto \quad \frac{1}{\epsilon n_d \omega Z^2}, \tag{1-7}$$

where Z is the charge of the defect and n_d is the concentration. Polar regions also contribute to loss by locally activating the quasi-Debye mechanism. A variety of defects (with differing dimensionality) can induce this loss, which can be approximated as

$$Q_{polar} \quad \propto \quad \frac{1}{\epsilon^{4.5-d}}, \tag{1-8}$$

where d is the dimensionality (d = 0 for point defects, 1 for line defects, 2 for planar defects). The strong permittivity dependence of this loss contribution means it is expected to decrease strongly as electric field is applied (thereby suppressing the dielectric constant).

Each of the previously described loss mechanisms has a Q that is inversely proportional to the AC signal frequency (at or below microwave frequencies). Another extrinsic loss mechanism that is sometimes discusses, termed the "universal relaxation law" is different in that it is nearly frequency-independent [12], [13], [21]. This law gives an expression for complex permittivity

$$\epsilon(\omega) - \epsilon_\infty = G(j\omega)^{n-1} = G\left(\cos\left(\frac{n\pi}{2}\right) - j\sin\left(\frac{n\pi}{2}\right)\right)(\omega)^{n-1}, \tag{1-9}$$

where $0 < n < 1$, ϵ_∞ is the high-frequency asymptote, and G is a frequency-independent constant. In practice, the value of n is between 0.99 and 1 for BST [13], [21]. This gives

$$Q(\omega) = \frac{C(\omega)}{C(\omega)-C_\infty}\tan n\pi/2 \approx \tan\frac{n\pi}{2} = Q_f. \tag{1-10}$$

The physical origin of this loss mechanism is sometimes attributed to creep of the depletion layer boundary in electrodes or to variation in charge transport barriers (such as grain boundaries) [12]. However, this fit to the Q seems to remain true for most cases when extrinsic device factors (such as device leakage and series roll-off, discussed in Section 1.2.3.2) [22], [23]. It may be dangerous to consider this a loss mechanism though, rather than an empirical observation. It does, however, provide a convenient tool for predicting the properties at a frequency that is not easily accessible to measurement. A summary of these loss mechanisms is given in Table 1-1.

Table 1-1: Summary of loss mechanisms and how they scale with frequency and permittivity.

Mechanism	**Type**	**Proportionality of Quality Factor**	
		With frequency	With permittivity
3-Quantum	Intrinsic	$1/\omega$	$\sim\epsilon^{-n}$ (2.5 < n < 5)
4-Quantum		$1/\omega$	$\sim\epsilon^{-1.5}$
Quasi-Debye		$1/\omega$	$1/n_r \sim \epsilon$
Charged Defects	Extrinsic	$1/\omega$	$1/\epsilon$
Polar Regions			$\sim\epsilon^{\mathrm{d}-4.5}$ (0<d<2)
DC Leakage	Device	ω	ϵ
Electrode Resistance		$1/\omega$	$1/\epsilon$

More than understanding which loss mechanisms can occur, the utility comes only if we can understand which mechanisms are dominant in overall device properties. A

theoretical analysis for $SrTiO_3$ shows that, among the intrinsic loss mechanisms, the quasi-Debye loss dominates until well above 100 GHz [20]. In general, higher frequency, higher DC field, and higher permittivity increase the relative importance of intrinsic loss mechanisms. As expected from the nature of extrinsic loss, it is highly dependent upon growth and processing. In high quality devices at microwave frequencies, however, the intrinsic and extrinsic mechanisms can be of comparable relevance [12].

While it is important to consider both loss and tunability in the overall performance of a material, a figure of merit still proves a useful metric to compare multiple works. For tunable capacitors, a good figure of merit is the Commutation Quality Factor, or CQF.

$$CQF = \frac{(n-1)^2}{n^2} Q(0)Q(E) \tag{1-11}$$

Here, $Q(0)$ is the Q at zero field, and $Q(E)$ is the Q at the field used for the tuning. Thus, Commutation Quality Factor can be plotted as a function of applied electric field E.

1.2 Previous work on BST

Before beginning with individual devices, a general survey of BST, $SrTiO_3$, and $BaTiO_3$ as bulk ceramics is needed. As discussed, $BaTiO_3$ is a ferroelectric at room temperature, with some of the highest performing piezoelasticity among lead-free piezoceramics [24]. It is a paraelectric above its Curie temperature of 120 °C with cubic m3m symmetry [8]. Below 120 °C, the symmetry shifts to tetragonal 4mm, marked by an extension of the lattice parameter in the c-direction. At 0 °C, $BaTiO_3$ undergoes

another phase transition to orthorhombic mm2 symmetry, at which point the polarization points along <110>. Below -90 °C, another phase transition to rhombohedral 3m symmetry occurs, and the ferroelectric polarization can be along <111>. For all of these phase transitions, the changes to the crystal lattice are all relatively small (<0.1 Å), but the polarization can be quite large (0.16 $\mu C/cm^2$ for $BaTiO_3$ at room temperature [25], and higher with applied stress [26]). As for the phase transition to the ferroelectric phase itself, there is evidence of both order-disorder and displacive character in the ferroelectric transition [27], [28].

In contrast, $SrTiO_3$ is an incipient ferroelectric, with only a single phase transition from cubic to tetragonal at 105 K [29]. This transition is not to a ferroelectric state, and only sees a slight rotation in the oxygen octahedron. There has also been evidence which points to a transition to an orthorhombic phase under high pressure [30], but this transition has not been observed up to 53 GPa [31]. The $SrTiO_3$ - $BaTiO_3$ phase diagram is investigated further in Ref. [32]. The lattice constant for BST is summarized for bulk ceramics in Figure 1-5.

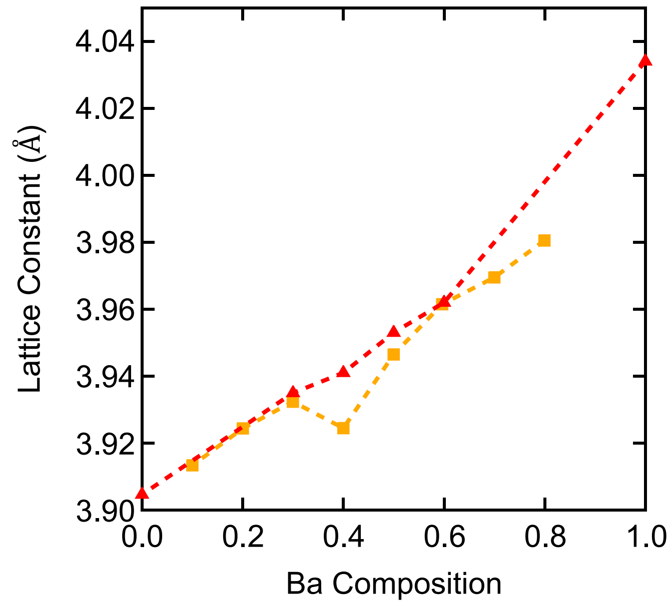

Figure 1-5: $Ba_xSr_{1-x}TiO_3$ lattice constant as a function of the Ba composition, *x*. (Red from Ref. [11], yellow from Ref. [33])

1.2.1 Device design types

While there are many methods by which to measure dielectric constant and loss [12], the ones discussed here will focus on device designs for making real world (thin film) devices with measurable properties. For this, there are two main device types: interdigitated capacitors and parallel plate capacitors. Generally, producing parallel plate capacitors is more challenging than interdigitated devices, but analysis and material evaluation is also much easier for parallel plate capacitors than interdigitated. While other planar capacitors can be made, the capacitance density is generally not high enough to be practical [12]. For this work, only a lumped element model is considered. When pushing to higher frequencies, the dimensions of the capacitors

eventually become comparable to the wavelength of the electromagnetic wave used to probe them, requiring a number of other considerations [12].

1.2.1.1 Interdigitated Capacitors

A large portion of literature on BST tunable capacitors utilizes an interdigital device capacitor (IDC) layout [34]–[39]. The primary advantage of this layout, shown in Figure 1-6a, is the planar nature of the device. In its simplest realization, an IDC only requires processing of metallic top contacts. A drawback to the interdigitated structure is the complicated and non-uniform nature of the electric-field lines under application of bias (Figure 1-6b). This requires complicated analysis to appropriately extract material properties and limits tunability since a large portion of the field is applied across an air gap [12]. Additionally, the non-uniform nature of the field means that the tuning is non-uniform for the BST even within the same device, and device failure occurs most often with the breakdown of the BST in the regions with highest field (edges and corners immediately underneath the fingers). This problem is especially exacerbated if the processing introduces additional defects or damage near those areas.

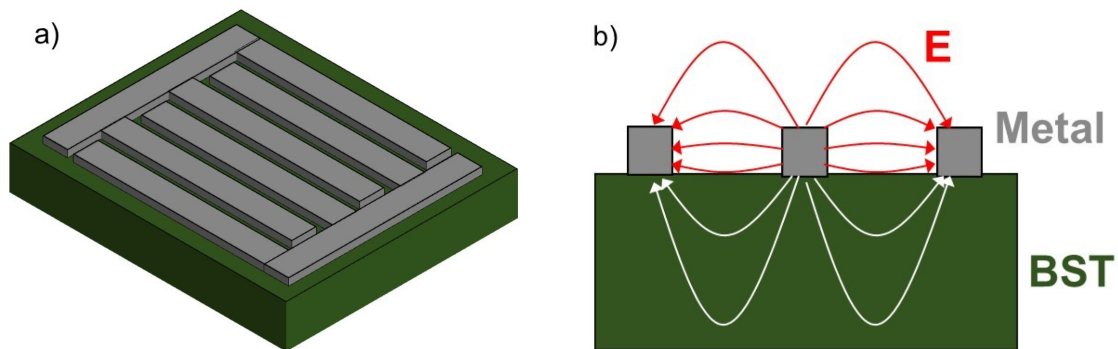

Figure 1-6: Diagram showing the interdigitated capacitor a) structure and b) how the applied bias generates a field within the tunable material.

For an interdigitated device, substrate selection becomes very important. Not only is lattice matching and registry to the BST film important, but the fringing fields shown in Figure 1-6b mean that substrate loss is also important. Figure 1-7 demonstrates the lattice constant range of BST (depending on composition between $BaTiO_3$ and $SrTiO_3$), and the array of commercially available substrates on which BST can be grown. Table 1-2 also shows dielectric loss and dielectric constants for some of these substrates. It is important to select a substrate with low loss and dielectric constant. $SrTiO_3$, for instance, would not make a good substrate for interdigitated capacitors because of its exceptionally high dielectric constant. Using this would make extraction of dielectric properties of the BST even more challenging and would also reduce the device performance since $SrTiO_3$ is not as strongly tunable.

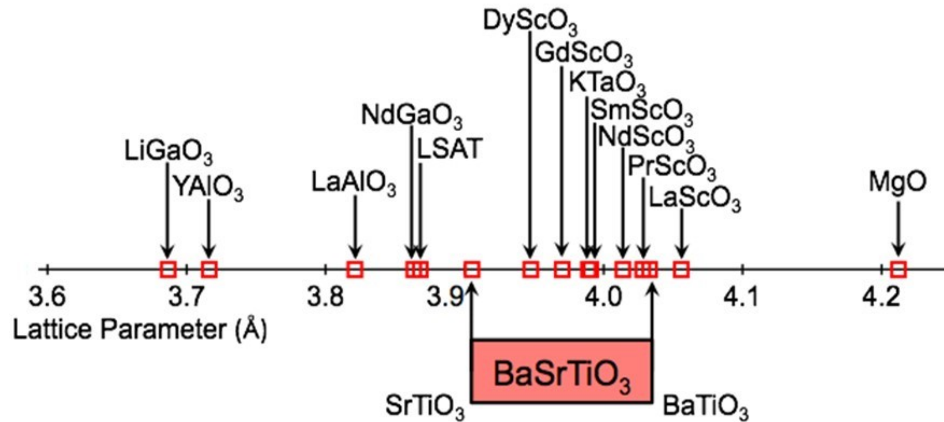

Figure 1-7: Lattice constants of commercially-available substrates that may be appropriate for use in the growth of BST. For orthorhombic crystal structures, the pseudocubic lattice constant is shown.

Table 1-2: Summary of Q-factors and dielectric constants for a variety of viable substrates for fabricating BST interdigitated capacitors [40]–[45].

	Q	f (GHz)	ϵ_r
$LaAlO_3$	50,000 30,000	6 10	24
$DyScO_3$ (110)	1000	12	27
LSAT	5000 3000	15.8 10	22.5
$NdGaO_3$	14000 5000	6.5 10.6	22
$SrTiO_3$	1667	2.9	314
$SmScO_3$	3333	10.5	25.2

1.2.1.2 Parallel Plate Capacitors (PPCs)

While interdigitated capacitors allow simpler processing, parallel plate capacitors require much simpler analysis to extract material properties. This is due to the simplified electric field profile through the active region of the device (shown in Figure 1-8). This structure can effectively be treated as two infinite charged plates, meaning the field is also uniform throughout the material. The obvious exception to this uniform field is at the periphery of the device, which can be accounted for with the addition of a fringing capacitance term [13]. An additional benefit of parallel plate capacitors is

reduced device footprint, since the capacitance density can be much higher. This reduced size does come with a trade-off, as discussed in Section 3.5.2.

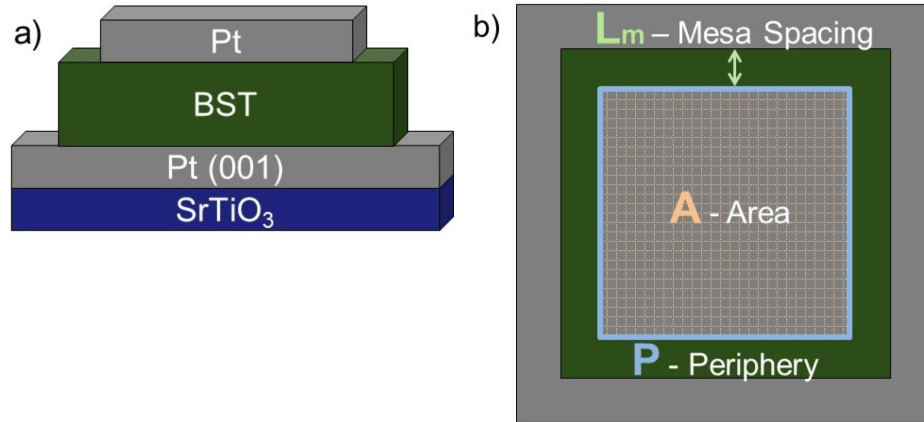

Figure 1-8: Parallel place capacitor layout showing a) cross-section and b) top-down views. Important parameters in device design geometry are highlighted in Figure 1-8b.

While analysis is much simpler, making these devices is more challenging than interdigitated structures. The primary reason is the bottom electrode, which is usually Pt. It is critical that this electrode have as low resistance as possible to reduce the device series resistance (See Section 1.2.3.2). Pt prefers strongly to have (111) surfaces, but BST grows rough on this orientation [46]. Since irregularities in the smoothness of the interfaces will lead variation in electric field across the device, this roughness will directly contribute to irregular device performance and premature breakdown. BST does grow smooth on the (001) face, though it is difficult to get Pt to grow in this orientation [47]. The growth and processing of Pt by sputtering in order to maintain the (001) orientation is discussed further in Section 1.2.5.

1.2.2 Device properties made with other growth techniques

An extensive summary of the microwave properties of BST films is made in Ref. [48], as summarized in Figure 1-9. From this work there are several main takeaways. For these devices to displace the current state of the art, there need to be devices with Qs above 200 and tunability above 2:1 [13]. While this review shows devices with Qs close to 200, and tunability of 2, they are not achieved in the same device. For instance the devices which actually have Q around 200 have a tunability of only 1.25, while those with tunabilities of 2 only have Qs around 20 [48]. This has not necessarily been the case for bulk ceramics or single crystals [33], indicating that improvements can still be made to thin film devices.

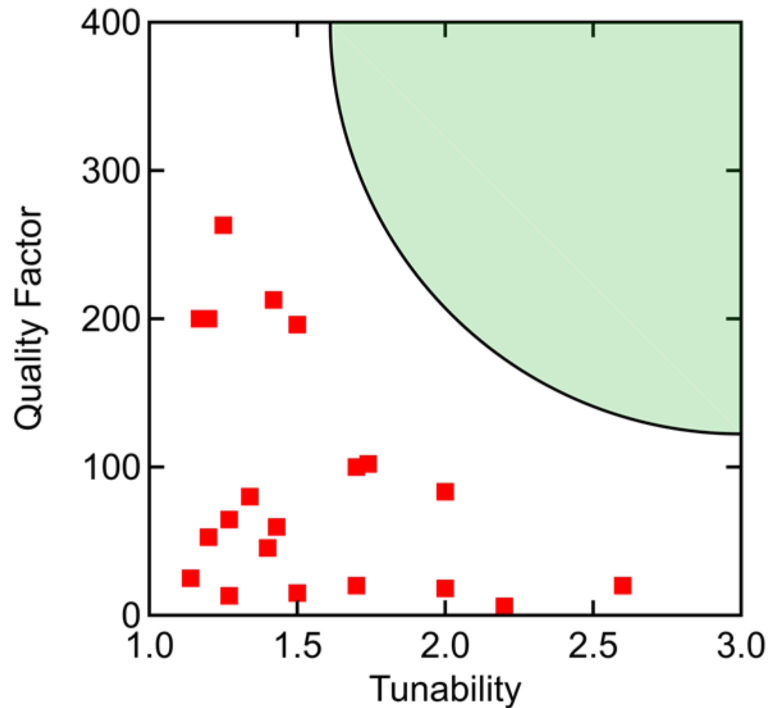

Figure 1-9: Summary of BST device properties shown in the literature review in Ref. [48]. The green area demonstrates the desired device properties to displace current technologies.

The bulk of the work done on thin film BST has been grown by pulsed laser deposition or sputtering. For these techniques, deposition is rather energetic, and this high-energy impact of atoms on the surface can generate additional defects, even very deep within the material [49]. Additionally, BST stoichiometry is coarsely controlled by changing the target material, which is often a bulk ceramic. As such, varying the target stoichiometry requires making a new target, the stoichiometry of which is also fairly coarsely controlled. Instead, some studies have demonstrated that modifying sputtering conditions can have an effect on the final sample stoichiometry by modifying the degree of incorporation of different atomic species [50]–[52]. These studies generally find that slight titanium excess is helpful in increasing the serviceable bias range of fabricated devices. Oxygen vacancies are also cited as a source of additional dielectric loss, and

divalent cations (such as Mg^{2+}) sitting on the Ti^{4+} site have been used to mitigate the effects of oxygen vacancies to limited success [48].

Another proposed method for the improvement of performance is the use of composites of BST and other materials [12]. In this investigation, it was shown that a layered ferroelectric composite (with field running perpendicular to the layering) behaves similar to a pure ferroelectric with a decreased Curie temperature (i.e. reduced dielectric constant and tuning). More interestingly, columnar composites and spherical inclusions should theoretically have lower effective dielectric constants without greatly affecting tunability.

1.2.3 Known performance limitations

While the usefulness of ferroelectric materials in tunable high-frequency devices dates back to the 60's, materials technology and device electronics meant it was not feasible at the time [53]. It is only in the past 25 years that intensive research efforts began demonstrating useful devices [12]. While we have not reached the maximum achievable performance for BST devices, this section discusses where those limits are expected to be.

1.2.3.1 Intrinsic

Generally speaking, device tunability will be highest when the dielectric constant is highest, or near the ferroelectric transition temperature. For BST, this transition occurs at room temperature near a composition *x* of around 0.7 [11]. This is the point at which tunability should also be highest. However, the motion of ferroelectric domain

boundaries are a source of loss, and due to local disorder, such as strain and composition, there can be regions which are polar even above the curie temperature. Thus, for loss considerations, it is better to be well above the Curie temperature. A diagram of intrinsic loss mechanisms is shown for the underdamped case ($\Gamma_0 \ll \Omega_0$) in Figure 1-10a. The soft mode phonon (is underdamped for $SrTiO_3$ at 80 K ($\Gamma_0/\Omega_0 \approx 0.02$) [12], whereas for $BaTiO_3$ it is overdamped ($\Gamma_0/\Omega_0 \approx 2.23$). It is estimated that tanδ follows Γ_0 as long as this soft-mode stays underdamped. Thus, as composition x of BST is increased, the loss should be expected to increase dramatically [12]. This follows well with observed trends [11]–[13], [33], [54].

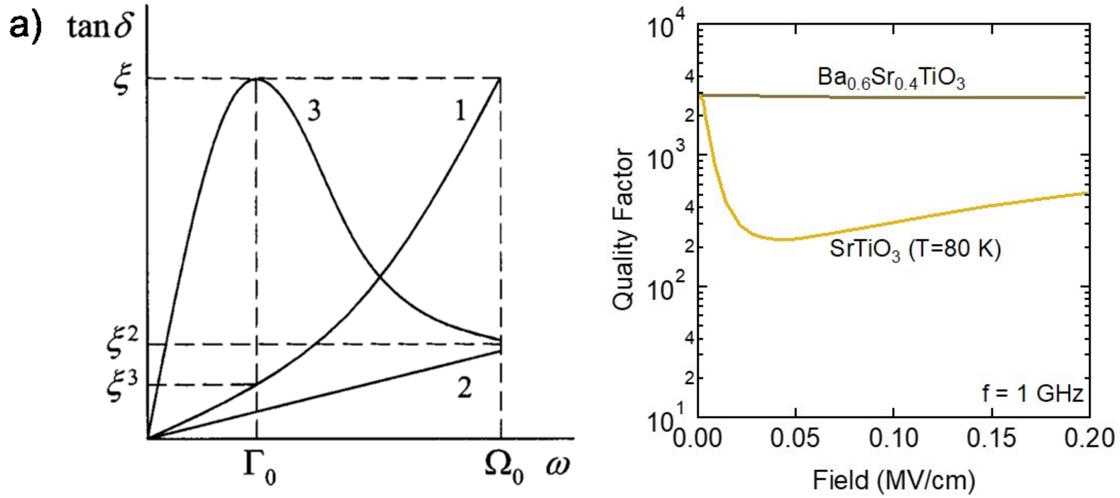

Figure 1-10: A summary of intrinsic loss mechanisms is shown in (a) with three-quantum (1), four-quantum (2), and quasi-Debye (3) loss. Γ_0 and Ω_0 are the soft-mode phonon frequency and damping, respectively. Panel (a) reprinted from [K. F. Astafiev, A. K. Tagantsev, and N. Setter, "Quasi-Debye microwave loss as an intrinsic limitation of microwave performance of tunable components based on $SrTiO_3$ and $Ba_xSr_{1-x}TiO_3$ ferroelectrics," *J. Appl. Phys.*, vol. 97, no. 1, p. 014106, Dec. 2005.], with the permission of AIP Publishing. (Ref. [20]) b) Calculations of quasi-Debye loss at 10 GHz are shown as a function of field for BST (x = 0.6) at room temperature, and for $SrTiO_3$ at 80 K. (Plotted from calculations in Ref. [20])

1.2.3.2 Extrinsic

For any real capacitor, the capacitance and *Q* vary as a function of frequency because of the series resistance and parallel conductance present in any real device. For a typical device, the shape of the *Q* is shown in Figure 1-11a. This general shape can be separated into three main regions, denoted with I, II, and III [13]. In region I, the parallel conductance dominates the electrical properties, and the equivalent circuit can be simplified as shown in Figure 1-11b. Similarly, in Region III the parallel conductance does

not contribute significantly to the measured Q, and the properties can be described by the equivalent circuit shown in Figure 1-11c. While we are most interested in the properties of the material, as measured in region II, it is still important to understand the behavior in regions I and III. It is region III where a roll-off in Q is observed, which is inversely proportional to the applied frequency. This high frequency roll-off is one of the most important hurdles that thin-film BST needs to overcome to make it soundly outcompete other technologies.

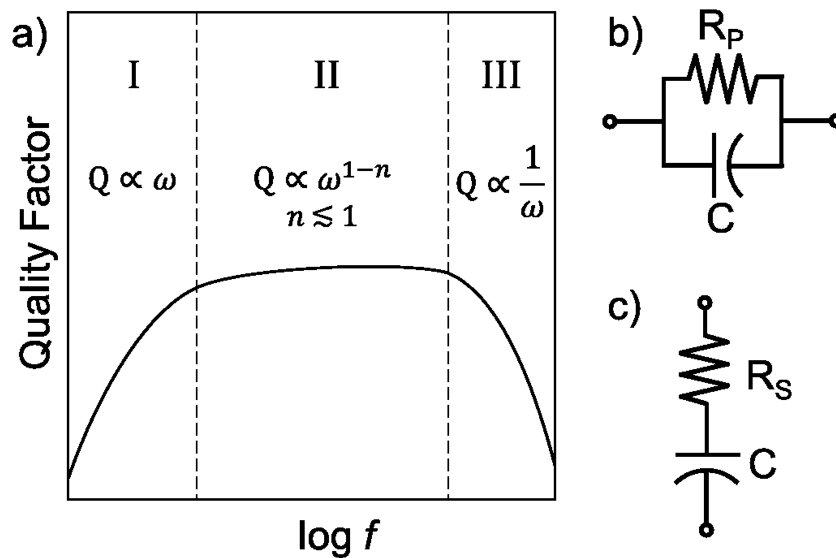

Figure 1-11: General shape for measured Q as a function of frequency for real parallel-plate capacitors (a). Regions I and III are limited by extrinsic device parameters (leakage and series resistance, respectively). Region II is limited by material parameters (intrinsic and extrinsic). The equivalent circuits are shown for b) region I (where series resistance has a negligible contribution) and c) region III (where parallel conductance is negligible).

At higher frequencies, the Q rolls off as $1/\omega$. At least three explanations are possible – limits of the instrumentation, a frequency-dependent Q from high-frequency

relaxation, or a series resistance due to extrinsic effects [13]. For a frequency-dependent loss tangent, one would also expect a corresponding change in the frequency-dependent capacitance. For instance, for the Debye law,

$$\epsilon(\omega) = \epsilon_{base} + \frac{\Delta\epsilon}{1+j\omega\tau} \quad \rightarrow \quad Q \approx \frac{\epsilon_{base}}{\omega\tau\Delta\epsilon} \tag{1-12}$$

However, for ferroelectric devices, with large dielectric permittivity, the change in permittivity may be comparably small.

Though series resistance contributions from the contacts do exist, they are not sufficient to describe the full 'apparent' series resistances seen in real devices. (The resistance contribution from the electrodes can be directly measured or modeled) [12], [55] One explanation for the remaining resistance is an interfacial 'dirt' layer between the BST and contacts. It is well-understood that photoresist is nearly impossible to completely remove from a wafer surface once spun on, and most devices considered use a liftoff process to deposit top metal contacts. Indeed, it has been shown for a series of cleaning strategies that a dirty surface dramatically alters the contact properties of Pt on Nb:$SrTiO_3$ [56], and the observed interfacial layer becomes thicker as the pre-deposition conditions are less-pristine.

1.2.4 Initial efforts with MBE-grown BST

For many years, researchers struggled to achieve simultaneous high *Q*s while also maintaining tunability above 2:1 at RF frequencies [13]. A recent study in our group achieved simultaneous high *Q* and tunability above 3:1 at 1 MHz by utilizing low-energetics deposition with molecular beam epitaxy (MBE) [57]. For some devices,

tunability of almost 7:1 were achieved, but this was with higher loss. This provides the ground work for the work on BST by MBE, with exceptional performance at these frequencies. Other work making tunable $SrTiO_3$ has been done by MBE through the formation of Ruddlesden-Popper type defects [58]. While some tunability was achieved, it was only about 20%. Unfortunately, dielectric loss was also relatively high at this tunability.

1.2.5 Stabilizing the (001) Pt surface

Though issues with growth of (001) Pt by DC sputtering has largely been solved [47], there remains a challenge of maintaining the (001) surface orientation in the high-temperature, high-vacuum environment required for MBE growth. In this study, we are investigating 100 nm of Pt sputtered onto $SrTiO_3$ (001) substrates. With a lattice constant of 3.92 Å, Pt is relatively closely matched with $SrTiO_3$ (3.905 Å). Additionally, Pt can provide a good Schottky contact to $SrTiO_3$ and $BaTiO_3$ above 1.2 eV after annealing in oxygen [59]. In the absence of oxygen plasma, a change in the surface reconstruction of Pt can be observed around 750 °C, with changes continuing as the substrate is heated as high as 900 °C (Figure 1-12). In addition to changes in RHEED, an increase in the intensity of the Pt 111 peak can be observed in XRD (Figure 1-13), as well as roughening in the surface structure by AFM (Figure 1-12). Note that 220 Pt reflection is also present, but it is not shown in this range of 2θ. Below 750 °C, the growth window for BST is too small to ensure high quality growth for the entire duration of the 300 nm film growth.

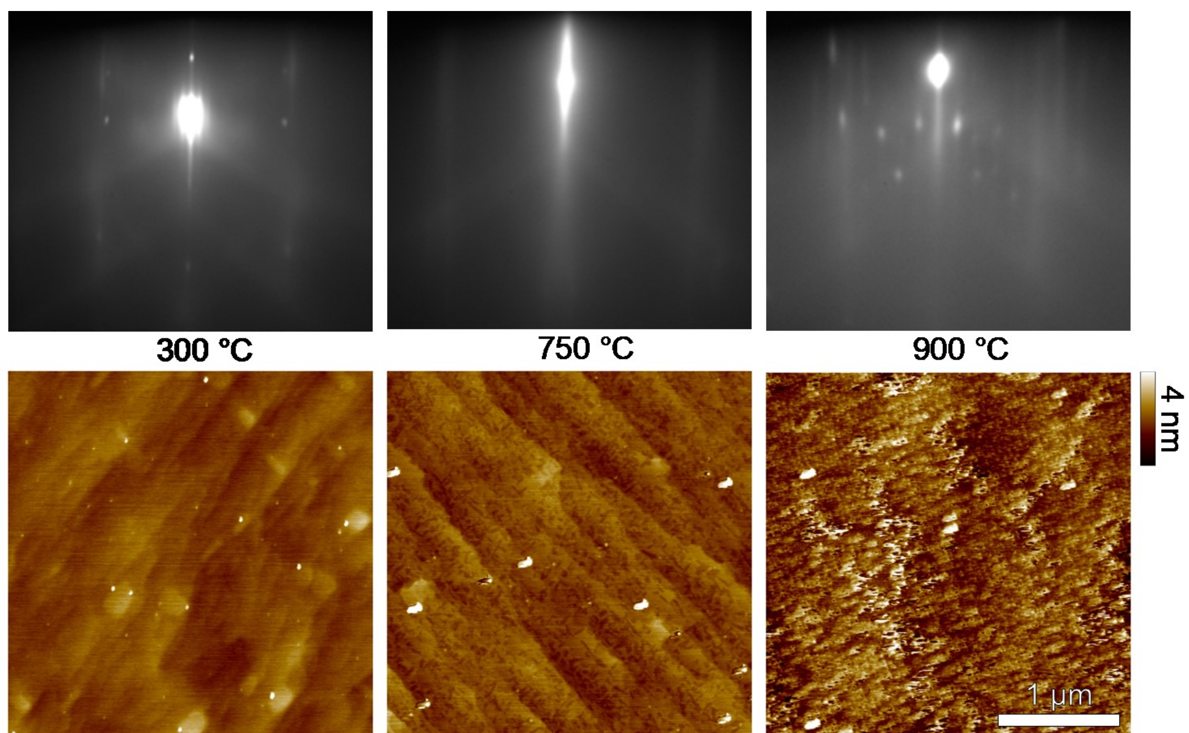

Figure 1-12: RHEED pattern (above) and AFM (below) for 100 nm Pt (001) films on $SrTiO_3$ (001) substrates heated in the MBE to the indicated temperatures.

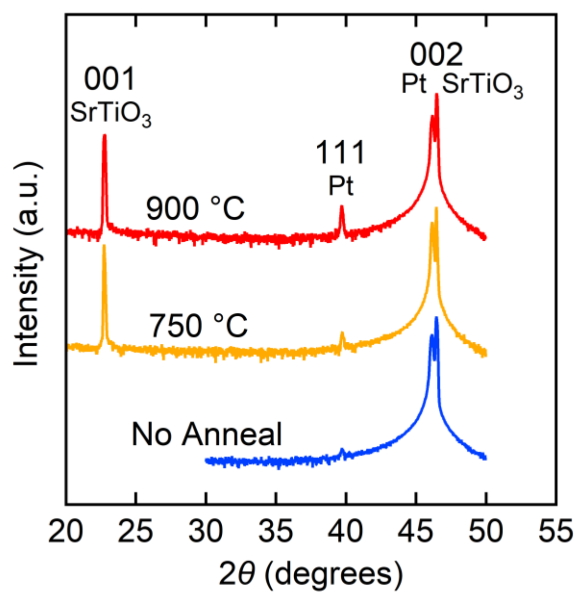

Figure 1-13: Wide-angle x-ray diffraction patterns for the Pt films heated in Figure 1-12.

This same annealing study was conducted in the presence of oxygen plasma, and RHEED, AFM, and XRD were again used to characterize the films (Figure 1-14, Figure 1-15, and Figure 1-16). As seen by these figures, the use of oxygen plasma stabilizes the (001) Pt surface. It should also be noted that cation stoichiometric BST can be grown with and without oxygen plasma, so the observed differences are expected to be due primarily to the different Pt film morphologies prior to the start of growth.

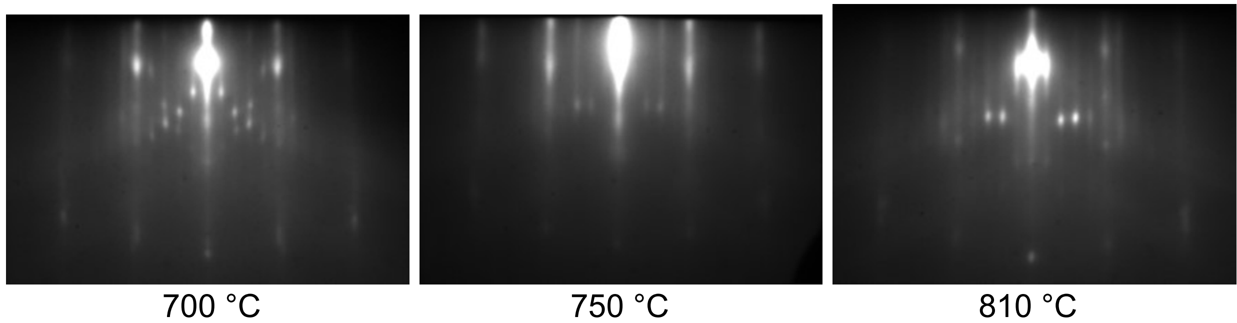

Figure 1-14: RHEED pattern from the 100 reflection of 100 nm Pt (001) films on $SrTiO_3$ (001) heated to the indicated temperatures under an oxygen plasma flow of 3×10^{-6} Torr.

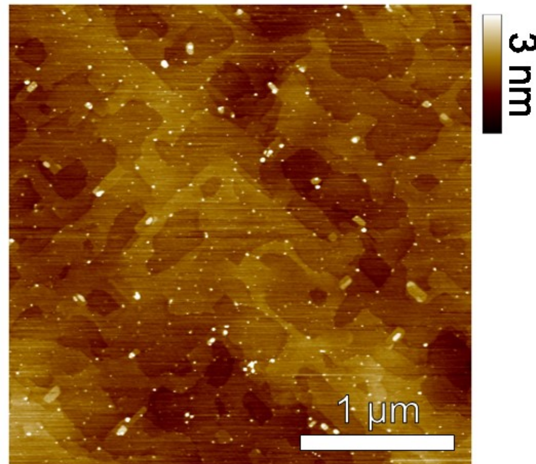

Figure 1-15: Post-anneal atomic force microscope image of the surface of a 100 nm Pt (001) film on $SrTiO_3$ (001) heated to 810 °C under oxygen plasma.

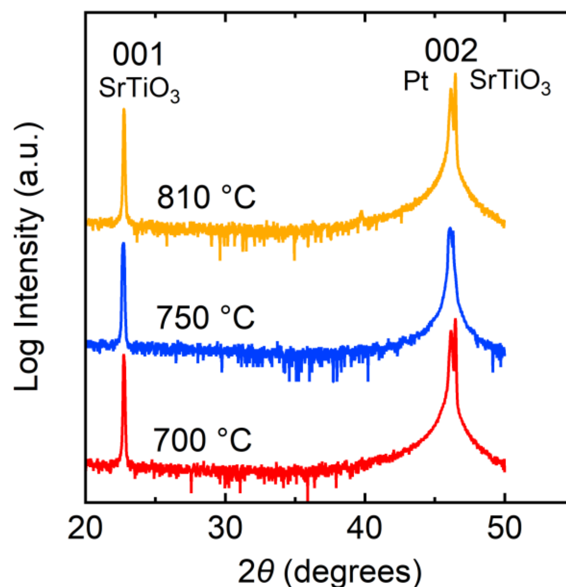

Figure 1-16: Wide-angle x-ray diffraction patterns for the 100 nm Pt (001) films on $SrTiO_3$ (001) annealed in MBE under oxygen plasma flow.

1.3 Transport in oxides

As mentioned in Section 1, electrical transport in perovskites is primarily controlled by the highest partially-filled orbital of the *B*-site cation, which forms the conduction band. For $SrTiO_3$, one of the most-discussed semiconducting oxides, the conduction band is primarily dictated by the Ti 3d orbitals. These are relatively close to the Ti^{4+} atom, and directional. For most transparent conducting oxides (TCOs), conduction is determined by a closed-shell $4s^0$ or $5s^0$ configuration [60]. The best-known of these TCOs is indium-doped tin oxide (ITO), which has demonstrated carrier concentrations of up to 10^{21} cm^{-3} and mobilities above 100, giving conductivities up to 10^3 $S{\cdot}cm^{-1}$. $BaSnO_3$ has a conduction band determined by the Sn 5s orbital as well, with the Sn^{4+} having a relatively disperse band [61]. For this reason, $BaSnO_3$ has drawn great interest

not only as a TCO, but also for its potential use as a channel material in all-oxide transistors [62], [63]. Some have even gone so far as to suggest that $BaSnO_3$ and other alkaline earth stannates may be able to eventually become the next silicon [64].

1.3.1 Electrical properties of $BaSnO_3$

$BaSnO_3$ is has an indirect band gap of 3.1 eV, and a direct gap of 3.36 eV [65]. Effective masses between 0.03 and 0.6 times the electron mass have been calculated [60], though more recent predictions of 0.22 [66] and 0.26 [67] are more reasonable. Indeed, an effective mass of 0.19±0.01 was measured optically in films grown at UCSB [68]. Other studies with lower-quality sputtered $BaSnO_3$ have measured an effective mass of 0.396 [69]. Dielectric constants of $BaSnO_3$ are consistent with other non-ferroelectric perovskites, with measured values of 15-17 [70] and 20 [61]. A common dopant source is La, which sits on the Ba site as a donor atom [71]. There was also a demonstration of p-type $BaSnO_3$ with K doping on the Ba site, but carrier activation energies were on the order of 0.5 eV [72]. At extreme carrier densities used in these systems, there is sometimes a band gap renormalization. While some works see evidence of this shift [66], films grown at UCSB have not shown evidence of this renormalization [65]. Notably, the earlier work that saw this renormalization was done using $BaSnO_3$ on $TbScO_3$ with a lower mobility of 81 $cm^2/V{\cdot}s$, though it was grown by MBE.

A large motivation for the continued work on $BaSnO_3$ thin films is the high performance demonstrated in single crystals, as shown in Figure 1-17. Mobilities above

300 cm^2/V·s were demonstrated at carrier densities near 10^{20}cm^{-3}, giving resistivities lower than 0.1 mΩ·cm. This remains the highest reported mobility at carrier densities this high. Even GaN, one of the highest-performing materials for high-power applications, has room temperature mobilities below 100 cm^2/V·s at these carrier densities [73].

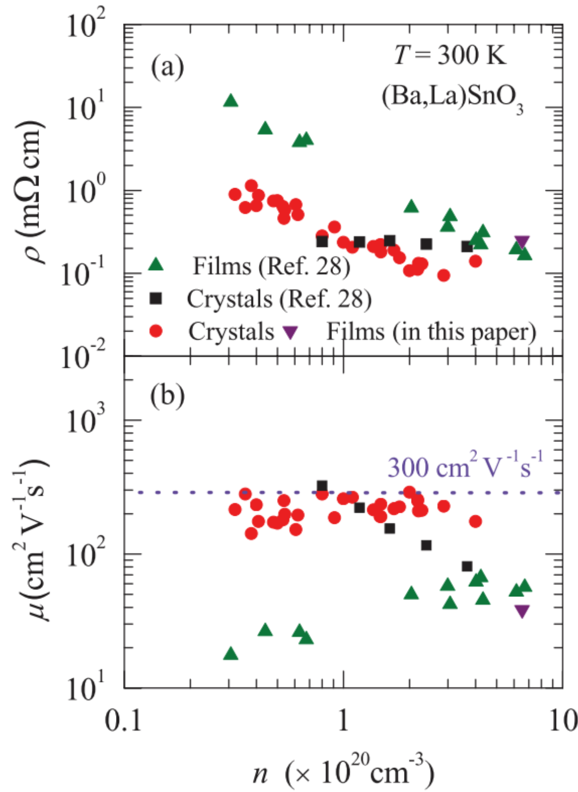

Figure 1-17: Summary of single-crystal (and some thin-film) mobilities for La:$BaSnO_3$. “Ref. 28” refers to Ref. [74] in this work. "Reprinted figure with permission from [H. J. Kim, U. Kim, T. H. Kim, J. Kim, H. M. Kim, B. G. Jeon, W. J. Lee, H. S. Mun, K. T. Hong, J. Yu, K. Char, and K. H. Kim, Physical Review B, vol. 86, no. 16, 2012.] © 2012 by the American Physical Society. (Ref. [75])

While extensive work has been done to replicate this performance in thin films, progress has been limited. While growth of $BaSnO_3$ by MBE has achieved the highest

mobilities for thin films, the highest measured mobilities are around 180 $cm^2/V{\cdot}s$ in a very thick film [76]. These films were grown using SnO_2 powder as a source for Sn and a highly reactive ozone source to supply additional oxygen. (For further discussion of the SnO_2 material, see Section 2.3) Work at UCSB has achieved comparable mobilities of 170 $cm^2/V{\cdot}s$, using SnO_2 and activated oxygen supplied by RF plasma. There has also been successful work using a metalorganic compound, hexamethylditin [77]. For this work, mobilities of 120 $cm^2/V{\cdot}s$ have been achieved for thick films. As will be discussed in Section 1.3.4, there may be significant systematic error in these measured mobility numbers that mean an absolute comparison of these mobilities may not be as meaningful as one would hope.

Dislocation densities in $BaSnO_3$ films are a challenge for improving mobility (see Section 4.6). Because of large lattice mismatch between $BaSnO_3$ and commercially available substrates, dislocation densities tend to be very high. For films on $SrTiO_3$, which has 5.1% mismatch, enormous dislocation densities of $1.5{\times}10^{12}$ cm^{-2} were measured [78]. For $DyScO_3$, with a mismatch of about 4%, dislocation densities between $1.2{\times}10^{11}$ and $3{\times}10^{11}$ cm^{-2} were measured [76], [78]. Some $BaSnO_3$ films have also been grown on $PrScO_3$ substrates, and though the lattice mismatch is lower than $DyScO_3$ (2.2%), dislocation densities are only slightly lower ($1.1{\times}10^{11}$ to $2.5{\times}10^{11}$ cm^{-2}).

1.3.2 Mobility limiting mechanisms

Any discussion of electronic devices requires some consideration of electronic conductivity. Mobility is a fundamental piece of that discussion, with conductivity (σ) described as:

$$\sigma = q_e(n\mu_e + p\mu_h), \tag{1-13}$$

where q_e is the electron charge, n and p are electron and hole concentration, and μ_e and μ_h are the electron and hole mobilities, respectively. Mobility is effectively a measure of the speed with which carriers can be transported under an applied electric field. Because the valence band of complex oxides is mostly composed of O 2p states, which are very deep, it is extremely difficult in most cases to dope them p-type. As such, we can disregard hole conduction, and only need to consider electron conduction.

For most real materials, multiple scattering mechanisms are at play, each with their own dependencies on temperature, carrier density, etc. Note that mobility can be related to the time between scattering events through the effective mass:

$$\mu = {}^{e\tau}/_{m^*} \tag{1-14}$$

It is typically safe to assume the weak scattering limit, such that total mobility can be calculated by knowing the mobility limit from each independent mechanism by Matthiessen's rule, which by extension gives

$$\frac{1}{\mu_{tot}} = \sum_i \frac{1}{\mu_i} \tag{1-15}$$

Where i is an index to indicate each independent mechanism. A discussion of some of these mechanisms is discussed below. In a non-degenerate semiconductor, the Fermi-Dirac distribution can be approximated with Maxwell-Boltzmann statistics, as

described thoroughly in [79]. $BaSnO_3$ is a degenerate semiconductor at reported carrier densities [78], [80], however, so this approximation is not valid.

1.3.2.1 Phonon scattering

Because electronic conduction relies on the periodicity of the unit cell, deviations from average crystal positions contribute to scattering. One of the largest contributions to scattering in perovskite structures is the interaction of lattice vibrations, which disturb this order locally, with itinerant electrons. Conversely, as a charge carrier moves through a material, its Coulomb force also interacts with ions in the lattice, adding additional lattice vibrations. In cubic perovskites, there are 3 acoustic modes and 12 optical modes [79]. For acoustic phonons, the mobility can be calculated as follows [81]:

$$\mu_{\mathrm{AC}} = \frac{2e\hbar\rho v_{\mathrm{s}}^2}{3\pi n_{\mathrm{3D}} m_e^* a_{\mathrm{C}}^2} \ln\left(1 + e^{E_{\mathrm{F}}/k_{\mathrm{B}}T}\right) \quad (1\text{-}16)$$

where e is the electron charge, $\hbar$ is the reduced Planck's constant, ρ is mass density, v_s is the velocity of sound in the medium, a_C is the acoustic deformation potential, m_e^* is the electron effective mass, and k_B is the Boltzmann constant.

For polar optical phonons, such as the LO phonon mode, the polaron model for polar crystals is used to describe mobility. Mobility can be approximated as

$$\mu_{\mathrm{LO}} = \frac{\hbar}{2\alpha\hbar\omega_{\mathrm{LO}}} \frac{e}{m_P} \left(\frac{m_e^*}{m_P}\right)^2 f(\alpha) \left(\mathrm{e}^{\hbar\omega_{\mathrm{LO}}/k_{\mathrm{B}}T} - 1\right) \quad (1\text{-}17)$$

where $\hbar\omega_{LO}$ is the energy of the LO phonon mode, α is the electron-phonon coupling constant, and $f(\alpha)$ is a slowly varying function ranging from 1.0 to 1.4. The polaron quasiparticle mass is given as

$$m_P = m_e^*\left(1+\frac{\alpha}{6}\right), \tag{1-18}$$

and the (dimensionless) electron-phonon coupling constant is

$$\alpha = \frac{e^2}{\hbar}\sqrt{\frac{m_e^*}{2\hbar\omega}}\left(\frac{1}{\epsilon_\infty}-\frac{1}{\epsilon}\right). \tag{1-19}$$

For non-polar optical phonons, such as the transverse optic (TO) mode in cubic perovskites, the atomic motion does not produce macroscopic electric fields. As a result, it can only scatter electrons through local distortions in the lattice, shifting the conduction band. The mobility limit due to this scattering is calculated as follows [79]:

$$\mu_{\mathrm{TO}} = \frac{\sqrt{2}\backslash pi\; e\hbar^3\rho v_s^2}{(m_e^*)^{5/2}\omega_{\mathrm{TO}} d_0^2}\frac{e^{\hbar\omega_{\mathrm{TO}}/k_{\mathrm{B}}T}-1}{\sqrt{E+\hbar\omega_{\mathrm{TO}}}} \tag{1-20}$$

where $\hbar\omega_{\mathrm{TO}}$ is the TO phonon energy, d_0 is the optical phonon deformation potential, and E (=E_{F}) is the electron energy.

From these relations, electron-phonon scattering increases (thereby lowering mobility) as temperature increases. The acoustic phonon scattering is expected to be a strong contribution to the mobility of single crystal $BaSnO_3$ at room temperature, setting a theoretical upper limit for the room temperature mobility around 600 $cm^2/V\cdot s$ [60].

1.3.2.2 Ionized impurity scattering

The other suspected contribution to the limit to single crystal mobilities is ionized impurity scattering. While electron-phonon scattering is highly temperature dependent, due to the phonon distribution changes with temperature, ionized impurity scattering is effectively temperature independent for degenerate semiconductors [60].

$$\mu_{\mathrm{II}} = \frac{3(\epsilon_r\epsilon_0)^2 h^3}{Z^2 m^* e^3}\frac{n}{N_i}\left[\ln(1+\xi) - \frac{\xi}{1+\xi}\right]^{-1}, \quad (1\text{-}21)$$

$$\xi = (3\pi^2)^{1/3}\,\frac{\epsilon_r\epsilon_0 h^2 n^{\frac{1}{3}}}{m^* e^2}, \quad (1\text{-}22)$$

where ϵ_r is the relative dielectric constant, N_i is the density of ionized impurities, and Z is the effective charge of these impurities. Because ionized impurity scattering requires dopant atoms to be present, alternative doping schemes such as modulation doping or polarization doping present a chance to dramatically diminish the effects of this scattering mechanism in thin films.

1.3.2.3 Neutral impurity scattering

While ionized impurities scatter very strongly, neutral impurities also contribute to scattering – though not as strongly. While typically much lower in density than ionized dopants, the choice of deeper dopants, such as Sb (which dopes as Sb^{5+} + e^- on the Sn-site), leave a significant portion unionized (or effectively neutral Sb^{4+}) in the crystal [60]. Another example would be slight alloying of an isovalent ion, such as Sr on the Ba site. Because transport in $BaSnO_3$ is dominated by the *B*-site cation (e.g. Sn 5s orbitals), alloying on the Sn site could affect mobility more than alloying on the Ba site. Mobility as limited by neutral impurities can be calculated as

$$\mu_{\mathrm{N}} = \frac{2\pi e}{10 a_{\mathrm{B}} h}\frac{1}{N_{\mathrm{N}}} \quad (1\text{-}23)$$

where $a_{\mathrm{B}} = \frac{\epsilon_r\epsilon_0 h^2}{\pi m^* e^2}$ and N_{N} is the density of neutral impurities.

1.3.2.4 Scattering from other sources of disorder

A significant source of scattering in thin films that is not present in bulk comes from heterointerfaces within a film. This interfacial roughness scattering has been investigated for GaAs/InAs quantum wells, with the finding that mobility is dependent upon the size of the well (L_w) and the height/lateral size of size fluctuations at the interface (Δ and Λ, respectively) [82]:

$$\mu_{\mathrm{IRS}} \propto \frac{L_{\mathrm{w}}^{6}}{\Delta^2 \Lambda^2} g(\Lambda), \tag{1-24}$$

where $g(\Lambda)$ is a function of Λ, N_s, and T. Interface and surface scattering are also further discussed in Ref. [83].

Because of the large strains discussed in 1.3.1, $BaSnO_3$ films relax at extremely low thicknesses. This results in significant dislocation densities, which are also a source of scattering. For GaN, dislocation scattering is shown to affect mobility with a $n^{1/2}$ dependence [73]. Like ionized impurity scattering, scattering from dislocations also tends to be relatively independent of temperature. In a degenerate semiconductor like La:$BaSnO_3$, the mobility limit associated with dislocation scattering is described as [84]:

$$\mu_{\mathrm{DIS}} = \frac{8ea^2}{\pi h N_{\mathrm{dis}}} \left(\frac{3n}{\pi}\right)^{\frac{2}{3}} (1+\xi_0)^{\frac{3}{2}}, \qquad \text{1-25}$$

where

$$\xi_0 = \frac{\epsilon_s \epsilon_0 h^2}{m_e^* e^2} (3\pi^2 n)^{\frac{1}{3}}. \qquad \text{1-26}$$

and a is the lattice parameter, N_{dis} is the dislocation density.

1.3.3 Measuring mobility

Two types of electrical mobility are usually discussed – Hall mobility μ_H and drift mobility μ_d. For this thesis, all measured mobilities are Hall mobility. Hall mobility is measured by the Hall effect, by which a voltage difference is produced transverse to a supplied electric current and an applied magnetic field perpendicular to that current. The Hall coefficient R is inversely proportional to carrier concentration – $R = 1/N_e e$ for electrons and $R = 1/N_h e$ for holes. To calculate Hall mobility, we combine Hall coefficient with conductivity: $\mu_H = |R|\sigma$.

Drift mobility defines a velocity v_d with which the charge carrier moves under an applied electric field E. Drift mobility is then defined as

$$\mu_d = \frac{v_d}{E} \tag{1-27}$$

To calculate drift mobility, we can use Ohm's law:

$$J = \sigma E = nqv_d \tag{1-28}$$

where n is carrier density and q is carrier charge. If the average time between consecutive scattering events is τ, and carrier's effective mass is m^*, drift mobility simply becomes

$$\mu_d = \frac{q\tau}{m^*}. \tag{1-29}$$

Measuring mobility and carrier density requires the combination of resistivity and Hall measurements. In thin films, these measurements can be done with minimal processing using the van der Pauw technique [85], [86]. This versatile technique only requires that the sample be uniform thickness and be simply connected (e.g. no non-conducting islands or holes in the sample). The sample can be arbitrarily shaped, but

for our purposes we consider a square sample, as shown in Figure 1-18a. After placing very small ohmic contacts in the four corners, longitudinal resistance and Hall resistance can be measured according to Figure 1-18 b and c, respectively.

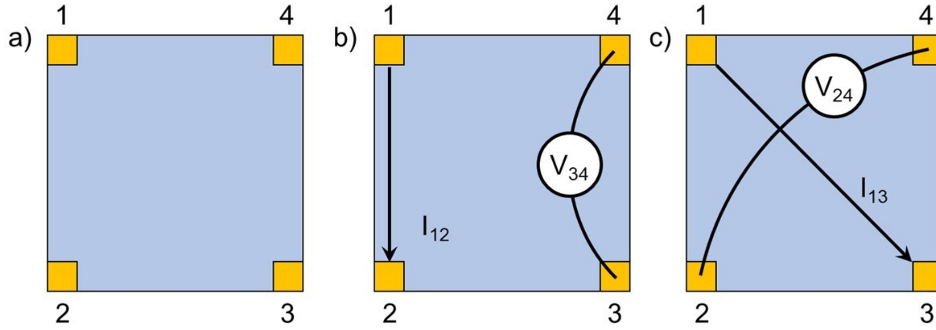

Figure 1-18: Diagram a) of van der Pauw sample geometry for measuring resistivity and Hall resistance in thin films using ohmic contacts labeled 1, 2, 3, and 4. Longitudinal resistance can be measured as shown in (b) for $R_{12,34}$, while Hall resistance can be measured as shown in (c) for $R_{13,24}$ with magnetic field out-of-plane.

To calculate sheet resistance R_s from longitudinal resistance, one has to measure the longitudinal resistance in the horizontal (as shown in Figure 1-18b) and vertical directions to get R_h and R_v, respectively. Here, R_h is measured as $R_{12,34} = {V_4 - V_3}/{I_{12}}$, and R_v is $R_{14,32} = {V_2 - V_3}/{I_{14}}$. These two resistances then fulfill the van der Pauw relationship [85],

$$e^{-\frac{\pi R_h}{R_s}} + e^{-\frac{\pi R_v}{R_s}} = 1. \tag{1-30}$$

Note that this may only be solved analytically for $R_h = R_v$. Numerically solving for R_s can be done using the Newton-Raphson method, as described in Ref. [87].

Hall resistance, R_H, results from the Lorentz force on mobile carriers generating a potential change orthogonal the applied current and an applied magnetic field [87]. The

measurement geometry in shown in Figure 1-18c. From the geometry shown, $R_{\mathrm{H}} = R_{13,24} = {V_4 - V_2}/{I_{13}}$. To calculate sheet carrier density, we can use

$$n_{\mathrm{s}} = \frac{B}{qR_H}, \tag{1-31}$$

where n_s is the net sheet carrier density, B is the magnitude of applied magnetic field, and q is the elementary charge. The Hall effect distinguishes between electrons and holes, such that if the Hall voltage in the geometry described is positive, there are more holes than electrons, and vice-versa. To calculate electron (or hole) mobility, we combine longitudinal and transverse resistance measurements:

$$\mu = \frac{1}{qn_{\mathrm{s}}R_{\mathrm{S}}} \tag{1-32}$$

1.3.4 Sources of error in Hall mobility measurements

While drift mobility and Hall mobility are typically similar, carriers with different energies can experience different Lorenz forces, making the measured values of mobility slightly different [67]. Hall mobility can be related to drift mobility through the Hall factor r_{H}, which is close to unity.

$$\mu_{\mathrm{H}} = r_{\mathrm{H}}\mu_{\mathrm{d}} \tag{1-33}$$

Deviation from unity stems from carriers having a relaxation time dependent upon the energy of the carriers. For non-degenerate semiconductors, Hall factor can vary from unity, especially if the Fermi level is within an impurity band, though it typically remains between 1 and 2 [88]. For highly degenerate semiconductors [88] (like $La:BaSnO_3$) or at high magnetic field [89], Hall factor is unity.

In addition to Hall factor, there are a number of factors related to the longitudinal and transverse resistances and sample geometry that can influence the measured mobilities. A few of these, and their significance, are discussed below.

1.3.4.1 Error in the sheet resistance measurement

As mentioned previously, sheet resistance is can only be solved analytically if longitudinal resistances are identical in both vertical and horizontal directions. In real measurements, this is often not the case. To numerically solve (1-30), we use the Newton-Raphson algorithm [87]. This iterative algorithm approaches a root by taking an initial guess, calculating a line tangential to that guess, and finding the intercept of that line. This pattern, repeated, leads to a solution which alternatively underpredicts and overpredicts the actual value, as shown in Figure 1-19a. By taking the difference between the last two estimates, we can get the maximal error for the calculation. The effects of this error on the measured mobility is shown for several samples in Figure 1-19b. In these cases, the error is nearly zero, showing that there is minimal effect on the actual measured mobility ($< 1\%$) due to uncertainty in the convergence of R_S.

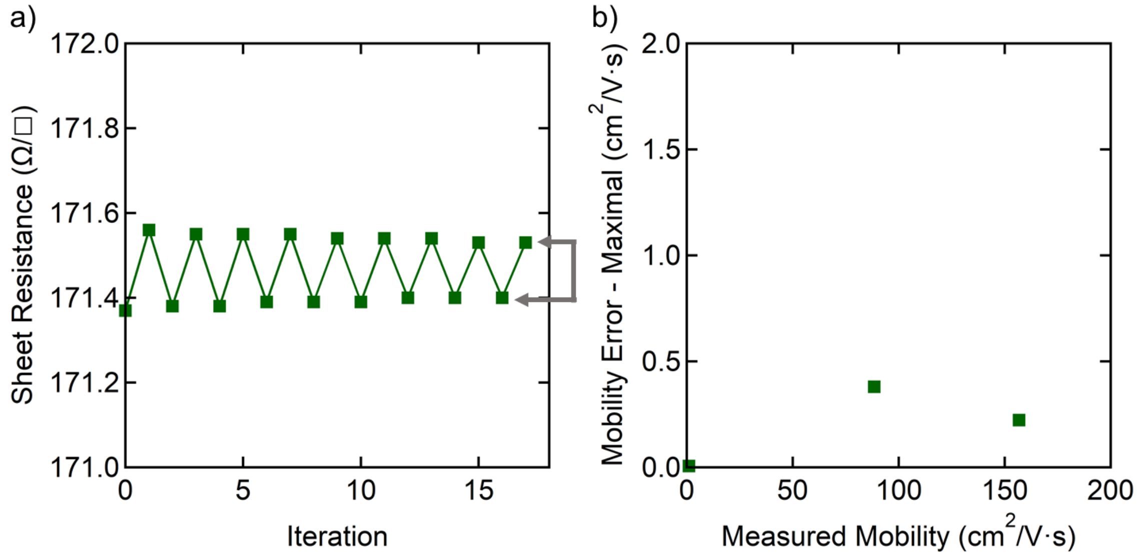

Figure 1-19: a) Maximal error shown for the convergence of the Newton-Raphson algorithm, and b) the maximal error in the mobility measurement for selected samples.

1.3.4.2 Error in the Hall resistance measurement

Another source of error is the standard error in fitting the slope of the Hall resistance as a function of magnetic field. To account for any component of longitudinal resistance in the measurement, each measurement is first antisymmetrized by averaging the magnitude at each field intensity. That is, $R_{\mathrm{H,antisym}}(B) = \frac{R_{\mathrm{H}}(B) - R_{\mathrm{H}}(-B)}{2}$. Fits to this line (shown in Figure 1-20a) give a slope which can be used to calculate sheet carrier density according to eq. (1-31). These three samples are shown because they each have either high measured mobility (μ = 156 cm^2/V·s) or comparatively large error (μ = 1.0 and 88 cm^2/V·s). Thus, this error should be considered close to the upper bounds found in the data presented in this work. The error is shown as a 95% confidence interval for these three samples in Figure 1-20b. While the error is just above 1% for the sample with moderate mobility (88 cm^2/V·s), it is much lower for the measured sample with the

highest mobility. As such, the standard error in the Hall resistance should not be a significant contributor to error in the measured mobility either.

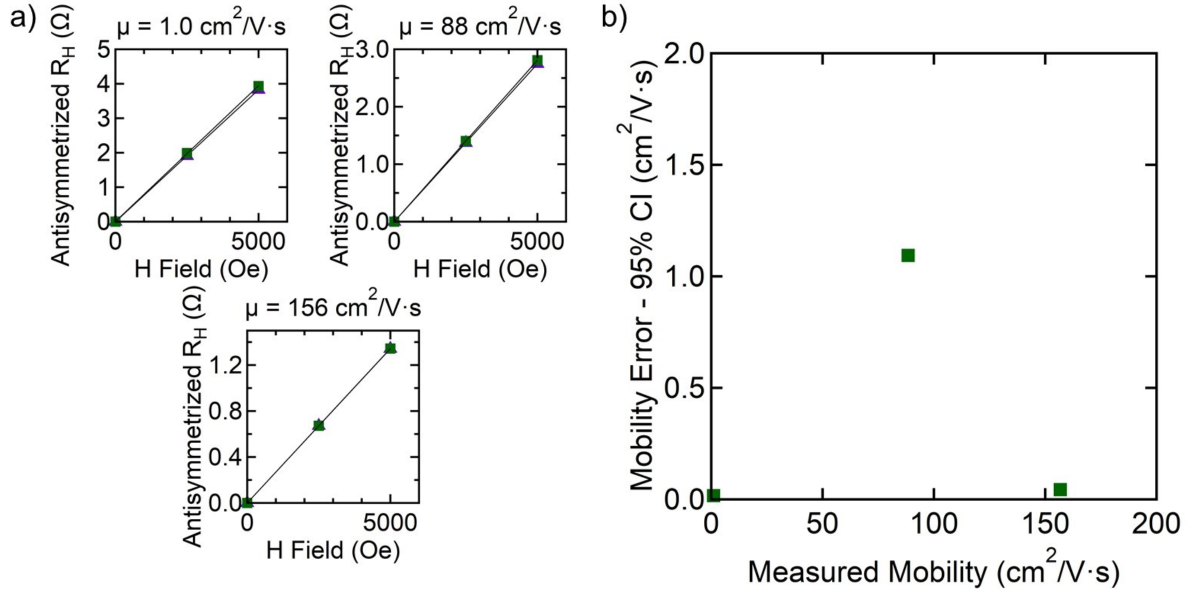

Figure 1-20: a) Fits to the antisymmetrized Hall resistance for two 90° rotations on each sample. Using the standard error in fits to the slope, error in mobility is shown in b) as a 95% confidence interval.

1.3.4.3 Effect of finite contacts on sheet resistance

While measurement error does not play a major role in inaccuracy in the mobility measurement, the van der Pauw geometry can have a more pronounced effect. As mentioned in Section 1.3.3, use of the van der Pauw geometry assumes extremely small contact areas. However, for many of our samples, which are 5 × 5 mm^2, the square van der Pauw contacts in the corners are relatively macroscopic at around 0.5–1.0 mm on a side. Macroscopic contacts cause the measured sheet resistance to be slightly lower than the true sheet resistance, which can be corrected for with a correction factor shown

in Figure 1-21a [90]. Taking a contact which is 1/6 the length of the sample's side (e.g. ~0.83 × 0.83 mm^2), this gives an offset of about 2%. The measured mobility is slightly over-inflated, and the impacts are summarized in Figure 1-21b. While the error does influence the measured mobilities, it is systematic in nature, and any trends observed in mobility will still hold regardless of the geometry (assuming geometry is consistent within the series). Note that this error is dramatically reduced by switching from square contacts in the corners to triangular contacts.

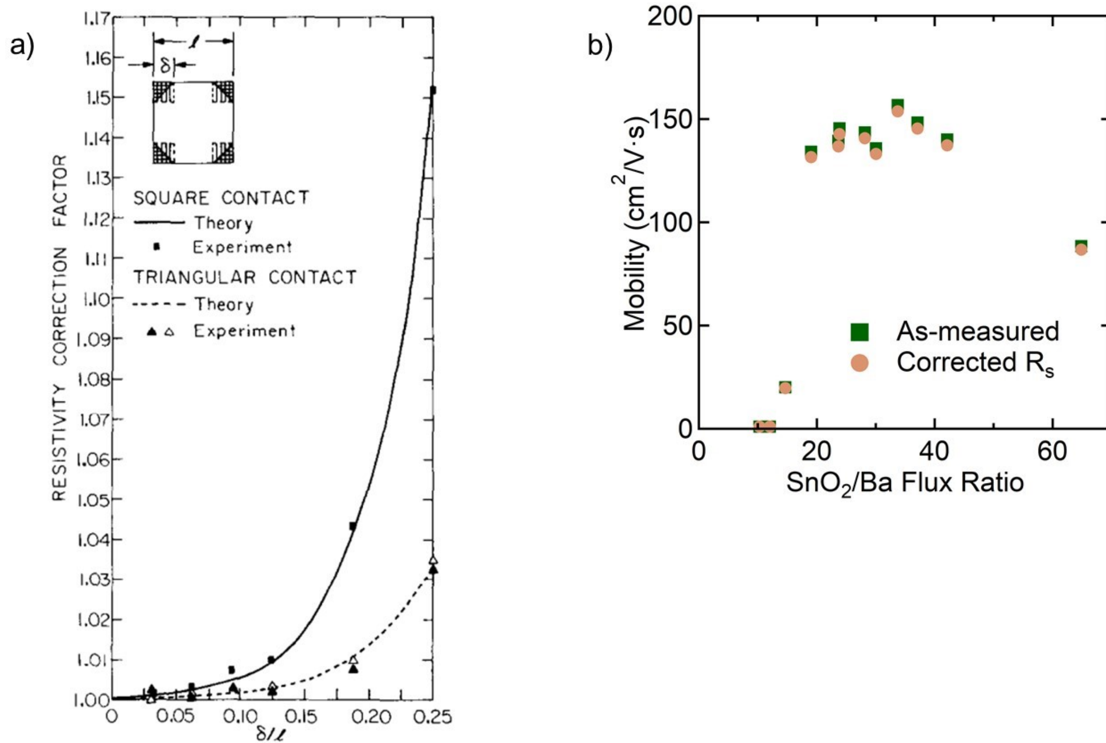

Figure 1-21: Correction factors to the sheet resistance are shown in a) for square and triangular contacts for contacts with size δ and sample of size l. Reprinted from [*Solid-State Electronics* vol. 17, issue 12, R Chwang, B J Smith, C R Crowell, "Contact size effects on the van der Pauw method for resistivity and Hall coefficient measurement," pp 1217-1227, Copyright 1974], with permission from Elsevier. (Ref. [90]) The effect of the sheet resistivity correction on measured mobilities is shown in b) with $\delta/l = 1/6$.

1.3.4.4 Effect of finite contacts on Hall resistance

While there is a noticeable effect on finite contact size on sheet resistance, the effect is even more pronounced in the Hall voltage [90]. The calculated correction factor is shown for triangular contacts in Figure 1-22a. For a 0.94 mm contact on a 5 × 5 mm^2 sample (e.g. $\delta/l = 3/16$), this amounts to an error above 20%. Here, $\tan\theta$ is the Hall angle,

defined as μ_H/H where H is the magnetic field in Oersted. In the samples measured here, the maximum field is only around 5 kOe, giving a Hall angle well below 0.5. Note also that the calculated correction factor is only given for triangular contacts, and it should be much larger for the square contacts used in this work. Once again, this error is systematic and does not interfere with drawing conclusions from trends in mobility. However, care must be taken when comparing measured/reported film mobilities that the reported error may differ from the true values.

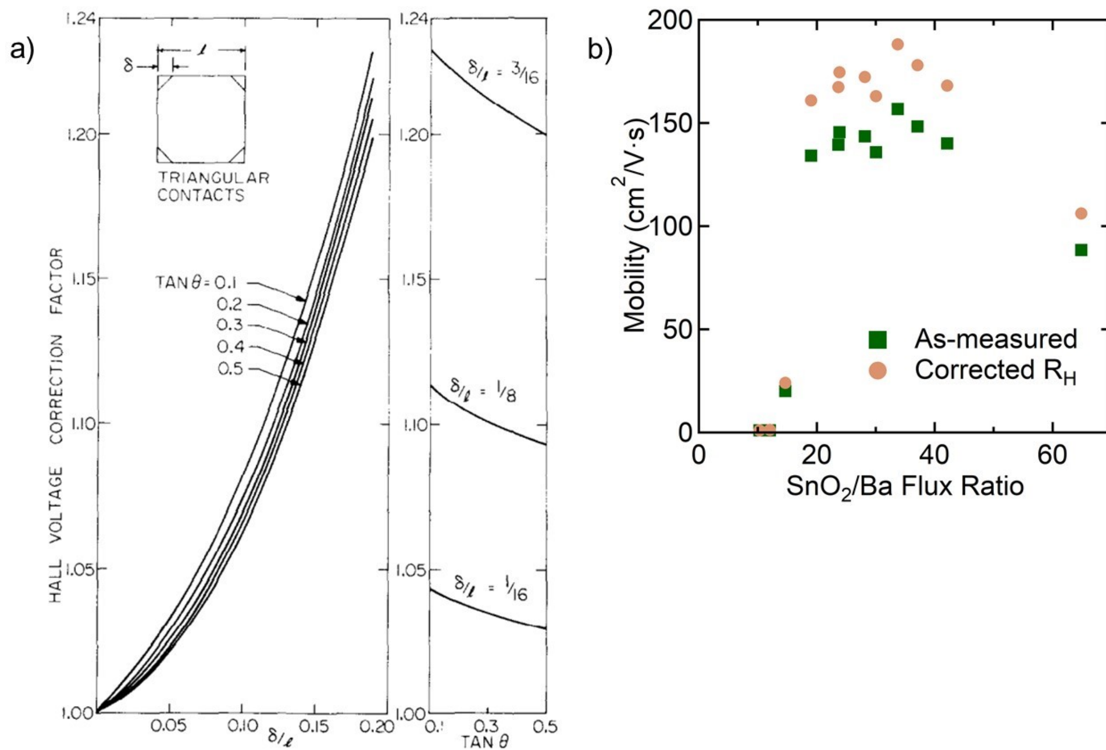

Figure 1-22: Correction factors to the Hall voltage are shown in a) for triangular contacts having contacts of size δ and sample side length l. Reprinted from [*Solid-State Electronics* vol. 17, issue 12, R Chwang, B J Smith, C R Crowell, "Contact size effects on the van der Pauw method for resistivity and Hall coefficient measurement," pp 1217-1227, Copyright 1974], with permission from Elsevier. (Ref. [90]) The effect of the Hall voltage correction on measured mobilities is shown in b) with δ/l = 3/16. Note that the error for square contacts (which are used in these measurements) is actually higher than shown.

1.3.5 Requirements for realizing all-oxide transistors

For realizing all-oxide transistors, we first need a high-mobility $BaSnO_3$ channel. While the goal is to eventually reach (and surpass) single-crystal mobilities, channel mobilities of 100 would still be higher than GaN at these carrier densities [73]. Another

important consideration is the modulation of the large charge densities achievable in this material. Because of the additional carrier density, larger modulation is also required for this system. Fortunately, the high dielectric constant observed in materials like BST or $BaTiO_3$ provides an effective gate dielectric with similar crystal structure for high-quality heterostructures. Using a $BaTiO_3$ gate, charge modulation upwards of 10^{14} cm^{-2} has been achieved in $SrTiO_3$ [91]. This charge density effectively sets an upper bound for the charge density within the channel, which at a density of 10^{20} cm^{-2} gives a maximum thickness of 10 nm. Charge modulation becomes more effective for charges which are closer to the gate, which also supports this push towards thin $BaSnO_3$ channels. For this to be effective, a high degree of carrier confinement is required, meaning a suitable back barrier with relatively high conduction band offsets is needed.

In addition to larger gating with its high dielectric constant, a $BaTiO_3$ gate also has the benefit of reducing the field within the device. A simulation of device properties was done for field effect transistors with $BaSnO_3$ channels, and is shown in Figure 1-23 [92]. From simulating two devices, one with high-κ and one with low-κ gate materials, the resultant charge and field profiles are demonstrated. As seen in Figure 1-23d, the peak lateral field within the device is much lower for the device with a high-κ gate. This directly translates to pushing the device breakdown voltage to higher biases.

Modulation doping has long been a pivotal factor in achieving record mobilities in III-V systems. The fundamental concept is that dopants in the crystal lattice have a different charge than the atoms they replace. This charge disrupts the periodicity locally and introduces a scattering site that interacts more readily with flowing electrons, as

discussed in Section 1.3.2.2. Modulation doping is a means to separate the scattering center (i.e. the charged dopant ion) from the free carriers it is meant to introduce. By interfacing the intended charge channel (undoped) with a system having a higher conduction band level (doped), electrons can fall into the conduction band of the intended channel material. This is depicted in Figure 1-24. Moreover, this structure demonstrates delta doping, which is the concentration of all dopant sources within a very narrow range of the film thickness. Doing this changes the band bending from gradual to the kink shown, and it allows for more carriers to be injected through the interface at a given barrier height.

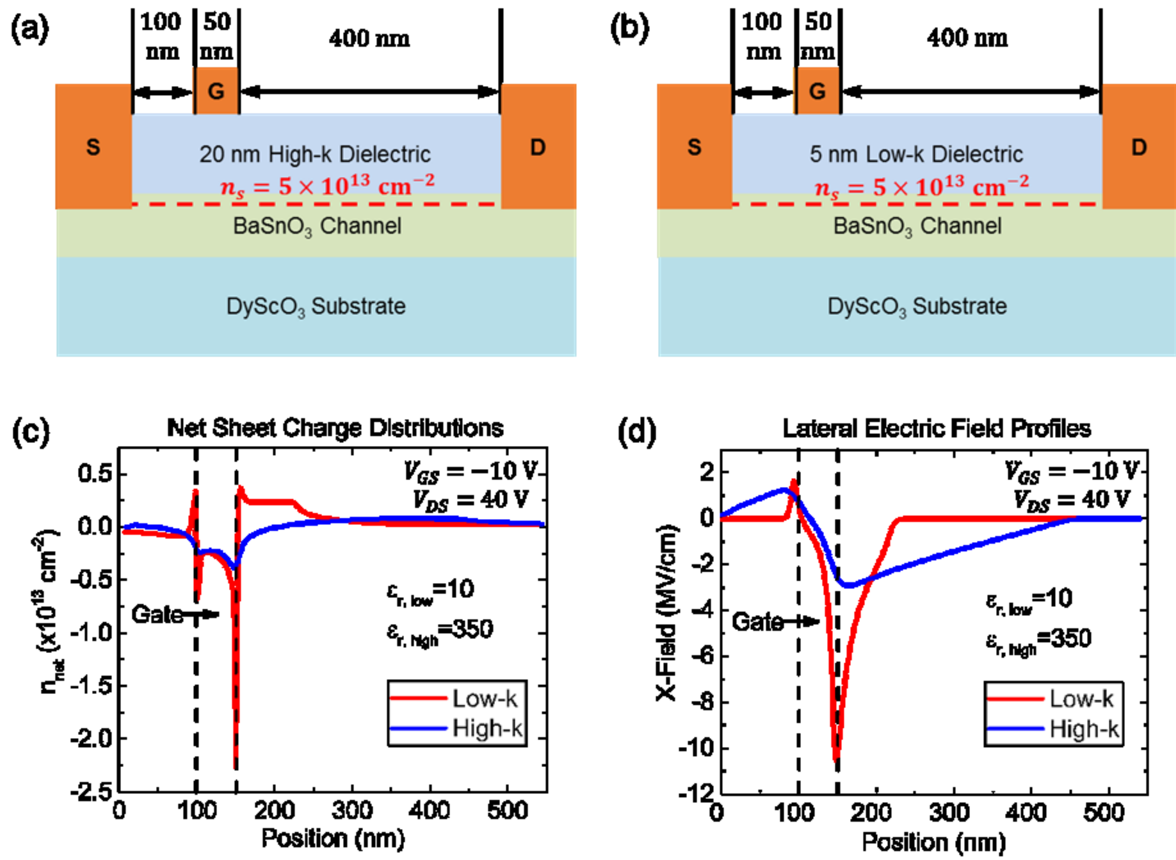

Figure 1-23: Device simulations of heterostructure field transistors with a) a high-κ dielectric constant (e.g. $BaTiO_3$) gate and b) a low-κ dielectric constant gate. Simulation results show c) net sheet charge distribution and d) lateral electric field profiles within the device [92].

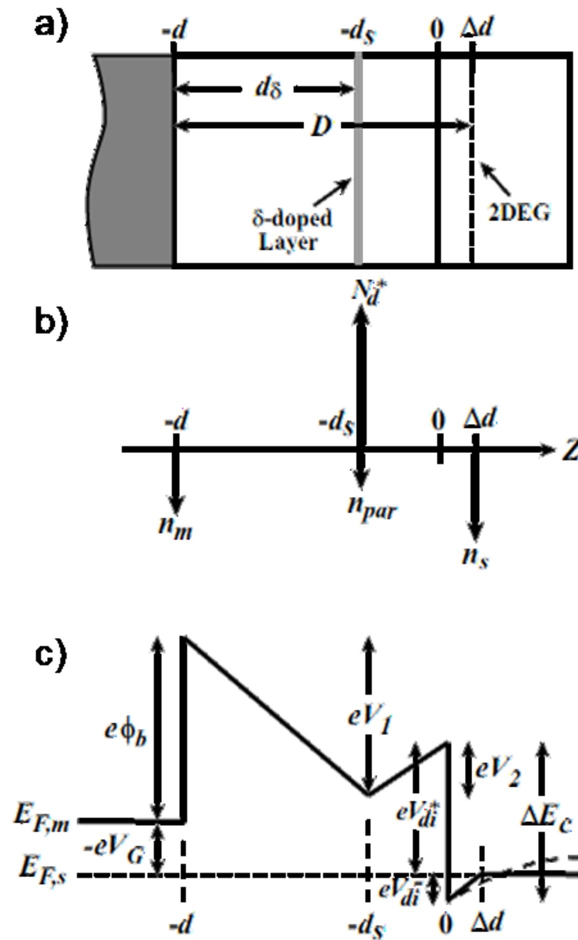

Figure 1-24: Structure for calculating modulation doping with a δ-doped injection layer (a). The doping layer ($SrTiO_3$) is δ-doped at d_s from the interface with the bottom layer ($BaSnO_3$) as a result of conduction band offset ΔE_c. Charge profiles (b) and partial band diagram (c) are shown for the resulting structure [93]. Reprinted by permission from Springer Nature Customer Service Centre GmbH: Springer *Semiconductor Device Physics and Design* by Umesh K. Mishra, Jasprit Singh, 2007.

By setting the difference between the valence band of the channel (right side of the figure) and the metal Fermi level to V_G, we can calculate sheet charge density in the 2DEG:

$$n_s(V_G) = \frac{eN_d^+ d_\delta + \epsilon\left[V_G - \left(\phi_b - \frac{\Delta E_C}{e}\right)\ \right]}{eD} \tag{1-34}$$

If we treat the 2DEG confinement well as triangular (as shown with the solid line), and define the sub-band energies associated with this well as E_i, where i is an index, the existence of this 2DEG requires $E_F - E_0 > 0$. Assuming only the first sub-band is dominant, we get

$$E_F - E_0 = \frac{e}{D_S} n_S = \frac{\pi\hbar^2}{m^*} n_S, \tag{1-35}$$

where Ds is the 2D density of states, $D_S = \frac{em^*}{\pi\hbar^2}$. From this, we can calculate the degree of confinement, eV_{di}^-, as a function of the 2DEG density (at zero gate voltage) based on the conduction band offset between $BaSnO_3$ and the material used to modulation dope it, as seen in Figure 1-25. For this calculation, D = 10 nm, d_s = 2 nm, and $m^* = 0.2 \cdot m_e$. As seen in Figure 1-25, the degree of confinement is low for the 2DEG densities shown here, which are well below 10^{14} cm^{-2}. Note that this does not indicate the condition where a parasitic channel begins forming (indicated in Figure 1-24 by n_{par}), which occurs before loss of confinement for the 2DEG.

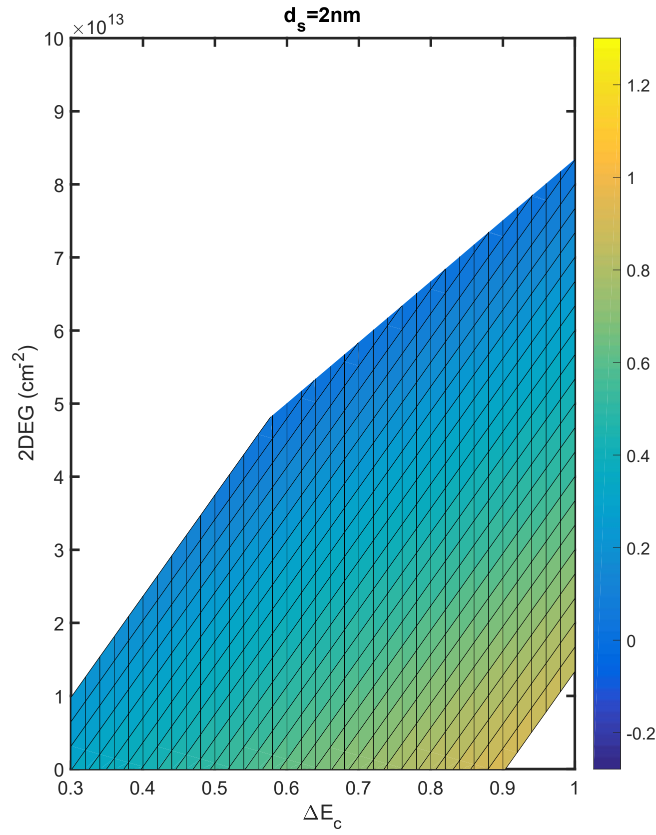

Figure 1-25: Calculated results for the amount of confinement of the 2DEG ($eV_{\bar{di}}$) as a function of the conduction band offset, ΔE_C and the 2DEG sheet charge density. For a well depth of 0 eV or less, there is no carrier confinement within the $BaSnO_3$ layer.

According to theoretical calculations [94], the $SrTiO_3$ conduction band is offset 1.14 eV above that of $BaSnO_3$. This work also used more sophisticated calculations to determine the 2DEG density and confinement using a Poisson solver. For a 2Å doping thickness spaced 2 nm from the $SrTiO_3$/$BaSnO_3$ interface, this permits confinement of 8×10^{13} cm^{-2} without spillover. This calculation, however, suggests a $BaSnO_3$ band gap of only 2.4 eV, compared to the measured value of 3.1 eV. Other work, in comparison, has

experimentally demonstrated band offsets of only 0.4 eV ± 0.2 eV [95]. This would lead to much lower 2DEG densities before spillover of several $\times10^{13}$ cm^{-2}.

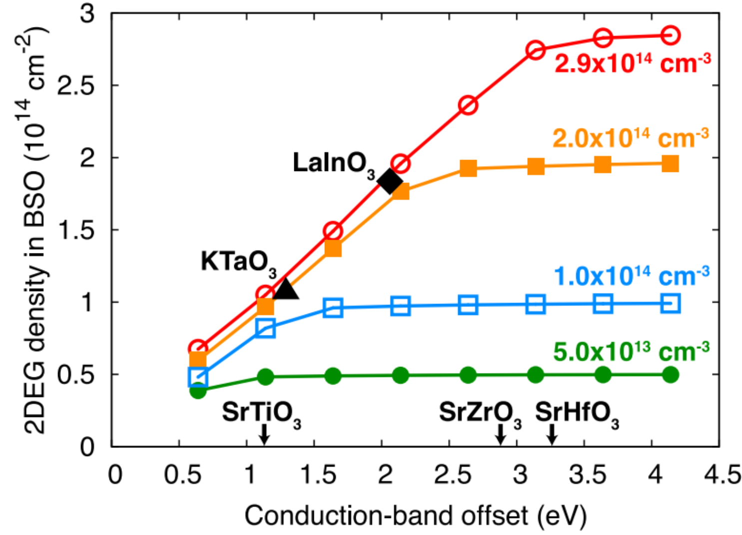

Figure 1-26: Degree of carrier confinement in $BaSnO_3$ as a function of the conduction band offsets for various sheet carrier densities. For the calculations, carriers were placed 2 nm from the $BaSnO_3$ interface. Calculated band offsets are indicated with arrows, and results for selected polar interfaces are also shown. Reprinted from [K. Krishnaswamy, L. Bjaalie, B. Himmetoglu, A. Janotti, L. Gordon, and C. G. Van de Walle, "$BaSnO_3$ as a channel material in perovskite oxide heterostructures," *Appied Physics Letters*, vol. 108, no. 8, p. 083501, 2016.], with the permission of AIP Publishing. (Ref. [94])

Recently, work demonstrating a depletion-mode MOSFET with a $BaSnO_3$ channel was reported with a transconductance of 2 mS/mm at room temperature and field-effect mobilities above 70 $cm^2/V{\cdot}s$ [96]. While an on-off ratio above 10^7 was achieved at low temperatures (77 K), the gating was less effective at room temperature, giving an on-off ratio below 3.

2 GROWTH, CHARACTERIZATION, AND FABRICATION METHODOLOGIES

The thin film perovskites investigated in this work are all grown by molecular beam epitaxy (MBE). This is an ultra-high vacuum technique, with base pressures as low as 10^{-11} Torr. At these pressures, the mean free path is on the order of hundreds kilometers (though atoms will hit the chamber walls long before then). This allows for the deposition of material whose purity (for reasonable growth rates) is limited only by the purity of the original source material. For MBE, this source material is often provided from solid source effusion cells, which face a heated substrate as shown in Figure 2-1. Because source material is supplied to the film using evaporation, MBE is a very low-energy deposition technique, comparable to atomic layer deposition (ALD) or chemical

vapor deposition (CVD). The MBE technique thus allows excellent purity and the capability for low defect concentrations, making it ideal for studying fundamental material properties and fundamental physics. However, the technique is also more expensive, with high maintenance costs, and very complex to operate. Since this work is trying to push the limits of current materials, which have already been explored by other means, MBE is an excellent choice of growth technique.

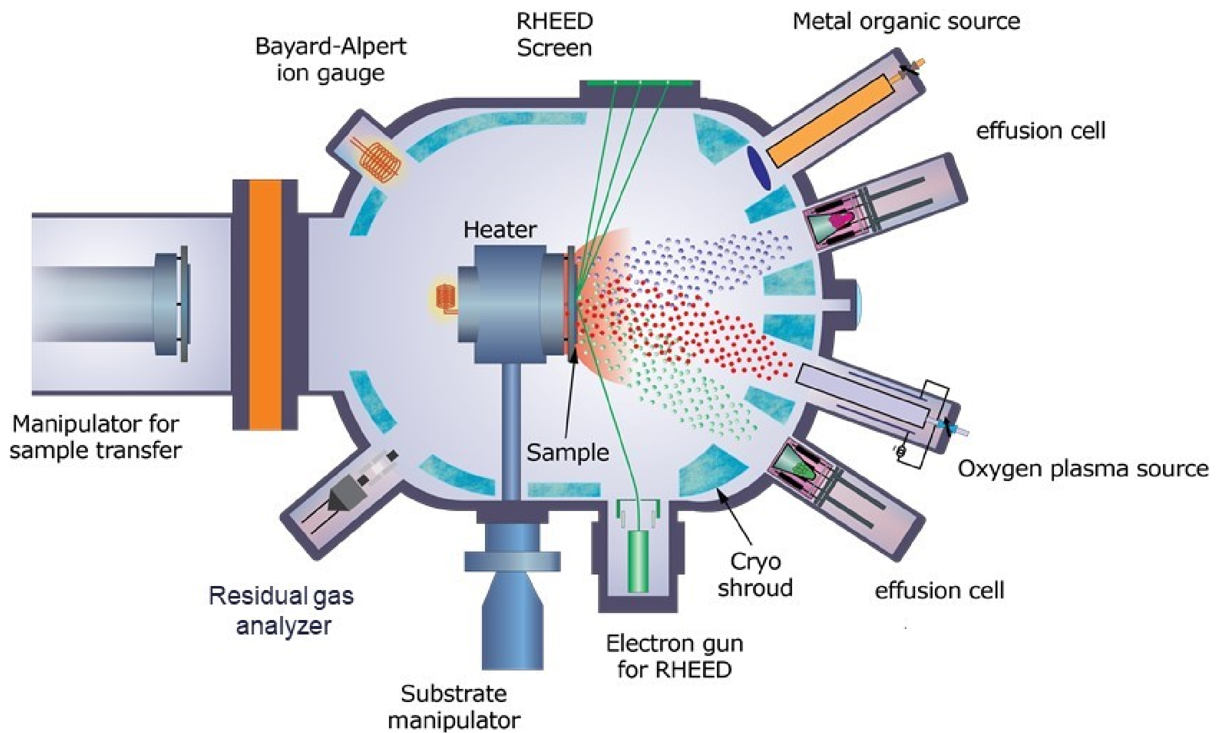

Figure 2-1: Schematic of the MBE chambers used in this work.

2.1 Hybrid MBE for growth of titanates

The success of III-V semiconductor growths by molecular beam epitaxy (MBE) hinges upon the growth of near-perfectly stoichiometric material. This is possible because of the “growth window” allowed by thermodynamics [97]. In GaAs growth, for example, an excess of arsenic is supplied from the cracker. Due to the high vapor

pressure of arsenic at growth temperatures, it can desorb, only bonding to the surface if there is unbonded gallium on the surface to bond to. This growth window is demonstrated below for GaAs in Figure 2-2.

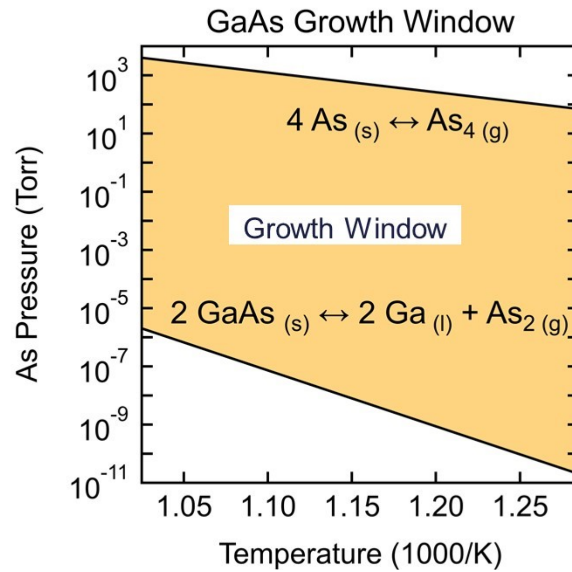

Figure 2-2: Estimated MBE growth window for the growth of GaAs from solid Ga and cracked As. Each line indicates an equilibrium for the reaction shown. Plot recreated from Ref. [98]

In traditional perovskite oxide growth by solid-source MBE ($SrTiO_3$, for example), the metallic species (Sr, Ti) are supplied by evaporation of solid metals in an effusion cell, and then oxidized by oxygen plasma. The low volatility of SrO and Ti create a growth window at impractically high growth temperatures or low growth fluxes. This is demonstrated in Figure 2-3. For reasonable growth rates, Sr fluxes at or above 10^{-8} are needed. For a growth window at these fluxes, growth temperatures of above 1500 K are required. In the absence of the growth window, and considering that solid-source fluxes can only be controlled within ±1% [99], defect concentrations can become excessively high (10^{20} cm^{-3}).

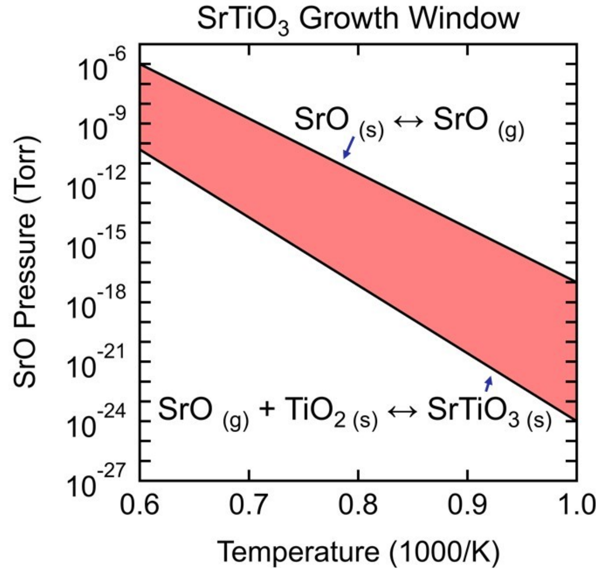

Figure 2-3: Estimated MBE growth window for the growth of $SrTiO_3$ from solid Sr and Ti sources. Each line indicates an equilibrium for the reaction shown. Plot recreated from Ref. [100]

However, by replacing one of the solid sources (in this case, Ti) with a volatile metalorganic precursor, a growth window becomes possible. Supplying Ti with titanium tetraisopropoxide (TTIP) has been demonstrated to enable an adsorption-controlled growth, eliminating the necessity for perfect flux control [100]. The effectiveness of this stoichiometry control was demonstrated for La-doped $SrTiO_3$, a material whose low-temperature mobility is strongly dependent on point-defect densities [81]. With the use of the TTIP precursor, homoepitaxial films with mobilities above 30,000 $cm^2/V{\cdot}s$ (at 2 K) were demonstrated, exceeding bulk measurements. Under strain (bending), these mobilities were pushed above 120,000 $cm^2/V{\cdot}s$ [101]. Using this same TTIP precursor, BST can be grown by supplying Sr and Ba from solid sources, and providing additional oxygen with an oxygen plasma source [57].

2.2 Parallel-plate device fabrication and characterization

To make parallel plate capacitors, 100 nm epitaxial Pt bottom electrodes were grown on (001) $SrTiO_3$ single crystal substrates (MTI, 10 × 10 × 0.5 mm^3) by DC sputtering as described elsewhere [47]. Pt films were post-growth annealed at 1000 °C for 10 min in oxygen. This anneal serves to stabilize the (001) orientation of the Pt film when heated under vacuum (Section 1.2.5). BST films were grown by hybrid molecular beam epitaxy as described in 2.1. Substrate temperature was 775 °C (set by thermocouple), and oxygen plasma was supplied by an RF plasma source operating at 250W with a background pressure of 3×10^{-6} mTorr. Approximate Ti/(Ba + Sr) (B/A ratio) was calibrated with 30 min growths on $SrTiO_3$ substrates by fixing cation beam equivalent pressure (BEP) for both Sr and Ba and varying the BEP of the metalorganic Ti source (TTIP). Like in $SrTiO_3$ [100], strained BST films exhibit a minimum in the out-of-plane lattice constant when films are stoichiometric (demonstrated later in Section 3.1). Lattice constants were determined using high-resolution 2θ-ω scans of the (002) reflection for BST (Philips X'PERT Panalytical MRD Pro Thin Film Diffractometer). 280 - 300 nm BST films were grown on Pt electrodes (thickness determined by x-ray reflectivity) with varying TTIP BEP to yield TTIP/(Sr + Ba) flux ratios of 28, 32, 36, 40, and 44. Post-BST-growth surfaces were investigated with atomic force microscopy [102]. Off-axis scans of the 103 reflection (MRD Pro with Pixcel3D detector) were used to obtain in- and out-of-plane lattice constants, which were used to determine $Ba_xSr_{1-x}TiO_3$ composition [11].

100 nm Pt top electrodes were blanket-deposited via either sputtering at 825 °C in 10 mTorr Ar following a 2 hour anneal in O_2 or by electron-beam (e-beam) evaporation

at room temperature with no *in-situ* clean. Using a two-step mask process, top-contact patterns were etched by Ar ion mill (Oxford), followed by a mesa etch with the Ar ion mill. After over-etching the active mesa in the ion mill, 80 nm Pt was deposited by e-beam evaporation to thicken exposed areas of the back contact through a liftoff process. After fabrication, devices were annealed for 20 minutes at 800 °C in O_2 to minimize oxygen vacancies.

While real-world devices would operate at microwave frequencies, low frequency measurements are often performed for basic materials characterization due to the high complexity involved in both device fabrication and data analysis as measurements enter the GHz range [12]. Impedance measurements (C_p-G) were taken on an Agilent 4294A impedance analyzer on 45 μm x 45 μm capacitors with a 60 μm x 60 μm mesa. Picoprobe GSG probes with 100 μm pitch were used for measurements. An AC probe amplitude of 50 mV was used. For bias sweeps, 50 mV steps and downward sweeps were used.

2.3 Selecting source material for growth of stannates

Significant effort has been put into selecting appropriate source materials for the growth of high-quality stannate perovskites by molecular beam epitaxy [78]. After the success of growing high-quality titanates by hybrid MBE, the obvious transition to growing stannates was finding an analogous Sn-containing metalorganic alkoxide precursor. Ideally this precursor should also contain oxidized Sn to facilitate reduction of Sn to the 4+ oxidation state needed for the stannate perovskite. One such precursor,

tin tert-butoxide, is nearly identical to zirconium tert-butoxide [103], which has been successfully utilized for the growth of zirconate perovskites [103]. Significant effort in growing using tin tert-butoxide eventually led to the conclusion that at temperatures sufficient to achieve reasonable flux, the precursor decomposed in the supply lines before even entering the MBE system. Initial efforts used a metallic Sn source, sacrificing the growth window and relying on an oxygen plasma to oxidize the evaporated Sn. Growth of SnO_2 by this method has been demonstrated previously [104]. This effort ultimately failed, with the plasma source not supplying enough activated oxygen to fully oxidize the Sn, leaving metallic Sn on the surface after attempted growths [78]. Likely the Sn that partially oxidized to SnO simply evaporated due to its high vapor pressure before it could further oxidize to SnO_2 [104].

More recent work [105] has successfully utilized a precursor, hexamethylditin, which contains nominally neutral Sn. While the authors claim a growth window (observed via a plateau in lattice constant from XRD as a function of relative cation fluxes) exists with this precursor, it appears vanishingly narrow from initial reports. This precursor does, however, enable growth of thick $BaSnO_3$ films with respectable mobilities above 100 $cm^2/V{\cdot}s$ [105].

Due to the difficulty in oxidizing the metallic Sn under ultra-high vacuum, SnO_2 powder was also tested to supply a large fraction of Sn already in the 4+ state [78]. While using SnO_2 facilitates the oxidation of Sn to the 4+ state, it introduces additional uncertainty in the form of other compounds that also evaporate from the source material – namely SnO, O^-, O_2, etc. Figure 2-4 shows the theoretical vapor pressures of

compounds that evaporate from SnO_2 powder as a function of temperature under 10^{-7} Torr oxygen (supplied by oxygen plasma source) [76]. As shown in the figure, the vapor pressure is dominated by SnO, requiring further oxidation by the plasma source to form the perovskite structure. The figure also demonstrates a high partial pressure of oxygen radicals. Note that in a typical oxygen plasma, typically only about 1% of the supplied oxygen is activated, while the rest remains diatomic oxygen. This indicates that at high cell temperatures the partial pressure of O^{-2} can be higher from the SnO_2 source than the oxygen source itself, which is beneficial for oxidizing the SnO fully.

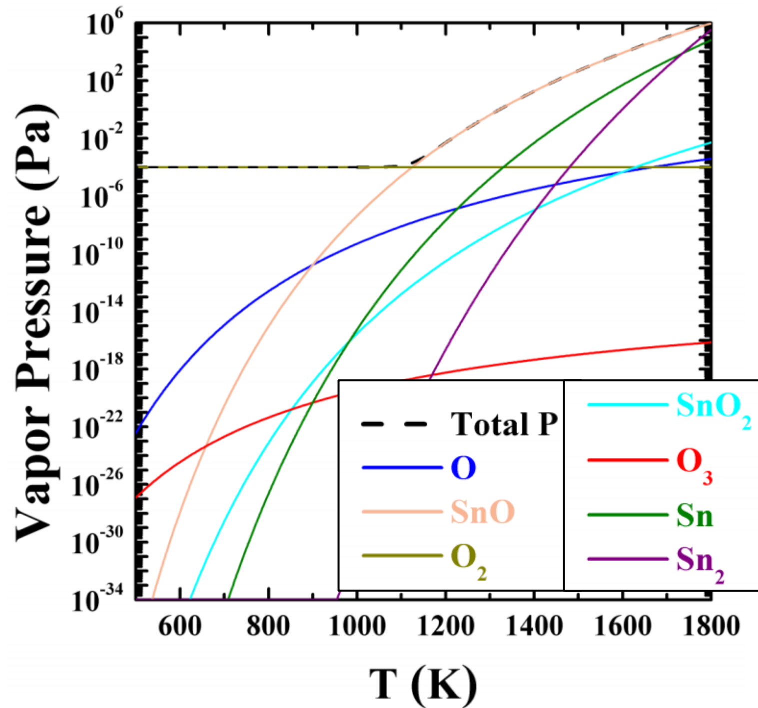

Figure 2-4: Vapor pressures of SnO_2 and its decomposition biproducts. Figure from [H. Paik, Z. Chen, E. Lochocki, A. Seidner H., A. Verma, N. Tanen, J. Park, M. Uchida, S. Shang, B.-C. Zhou, M. Brützam, R. Uecker, Z.-K. Liu, D. Jena, K. M. Shen, D. A. Muller, and D. G. Schlom, "Supplementary material: Adsorption-controlled growth of La-doped $BaSnO_3$ by molecular-beam epitaxy," *APL Materials*, vol. 5, no. 11, p. 116107, 2017.] is licensed under CC BY 4.0. (Ref. [76])

Using a SnO_2 source presents a challenge with consistency due to the changing contents of the crucible over time. While the exact contents of the cell are difficult to determine at a given time, a clear change is observed over time as the powder turns from a white/pale yellow powder to a caked gray powder. Figure 2-4 shows that SnO is the primary species evaporating from the cell. While the cell initially contains only SnO_2, over time oxygen evolves from the powder, leaving SnO and metallic Sn. There are also reports of the formation of Sn_2O_3 or Sn_3O_4 as intermediate suboxides, but only

below 550 °C [106]. Additionally, these Sn suboxides are not very stable. Instead, they will react with oxygen if present. In reducing conditions, they spontaneously disproportionate to other suboxides (including SnO_2) and metallic Sn [107]–[110].

Another challenge in the growth of stannate perovskites with a SnO_2 source is the large fluxes required, due to the volatility of SnO. Some reports suggest that this actually leads to desorption-limited growth, opening a growth window [76]. While the desorption of SnO_x from the surface may enable the opening of a growth window [76], the high fluxes needed mean the source material depletes rapidly compared to other sources. For example, with the original 25 cc high-temperature cell at a temperature between 1150-1250 °C, only 15-25 90-minute growths could be completed before a dramatic drop-off in flux from the SnO_2 cell due to depletion of the source material. To combat this, a 120cc, dual-filament, high-temperature effusion cell was purchased to hold a considerably-larger volume of SnO_2 source material. With this new cell (only filled around half-way for better flux uniformity and to prevent extra heating from the tip filament), 75-100 90 minute growths are achievable before depleting the source material. This reduces both the amount of time spent with opening, baking, and recalibrating the MBE system to refill material and also allows for longer growth series without having to constantly search for good growth conditions.

The use of a dual-filament cell, each with its own thermocouple and PID controller, adds the capability to maintain a different temperature at the base of the cell (i.e. where the source material is) and the lip of the crucible. Even with the 25 cc effusion cell, a shell of material would form near the end of the crucible which would slowly close off

and block flux from the base of the cell. Under the wrong conditions, this process causes a dramatic drop in flux from the cell. Opening to refill what was expected to be an empty cell revealed this shell. The use of a dual-filament cell allows a higher tip temperature to reduce this deposition from the start. While unclear from the manufacturers specifications how large a temperature gradient is possible, a fairly significant 100 °C higher tip temperature has been used without any evident damage to the crucible over years of use. Previously a temperature difference as high as 150 °C was used. This stopped after a crucible cracked and broke, but it should be noted that the ramp rate for the cell when this damage occurred was 10 °C/min, which is much faster than the 2 °C/min that is commonly used for alumina. Since the damage to the crucible occurred near the base, and not in the region where a temperature gradient should be expected, a difference of 150 °C between base and tip zones is likely safe.

The highly reactive nature of the SnO_2 and its biproducts, such as atomic oxygen, requires the use of alumina crucible for evaporating the SnO_2 powder in the MBE chamber. As we discovered after initial tests growing with the powder, the Ta shielding on the effusion cell itself is also susceptible to the reactive powder and its biproducts at cell temperatures upwards of 1250 °C (e.g. crucible lip temperatures above 1350 °C). The damage sustained over the life of one crucible worth of material was sufficient to require a complete rebuild of the cell. To combat this damage, an extra thickness of spiral tubing was added around the crucible body to run cooling water to keep the protective sheathing cool. By reducing the temperature of the external sheathing, the rate of degradation is dramatically reduced.

3 ENHANCING PERFORMANCE OF $Ba_xSr_{1-x}TiO_3$ TUNABLE CAPACITORS

As seen in Section 1.2, the field of BST varactors is quite developed. The technology has been on the market for over a decade in a variety of technologies. Samsung phones have previously used sputtered BST for tunable antennas in cell radios [111]. Panasonic has used BST deposited by sol-gel methods for the extremely high capacitance density. More recently, ON Semiconductor has used BST in hearing aids, and they are now selling BST into handsets at smaller volume for antenna tuning. Last year, ON Semiconductor is reported to have sold over 100 million BST capacitors. Even so, scale has been limited, preventing them from getting into huge markets like the iPhone. This array of market applications is only possible because of its effectiveness in competing

with existing technology. Nevertheless, the use of MBE-grown BST represents a potential for extreme improvements in device performance, as discussed in Section 1.2.4. With this comes an opportunity to investigate intrinsic material limitations as contributions from extrinsic factors are reduced. This work seeks to further understand how to improve device performance through the understanding of these limitations. By understanding these limitations, we seek to determine if it is possible to grow BST by other techniques with the extraordinary performance seen in MBE-grown material. There remain a number of fundamental differences in the properties of material grown by MBE vs. sputtering or PLD. Among these are the energetics of the deposition, the degree of *A*:*B*-site stoichiometry, and the presence of impurities in the film. While some of these parameters are more or less out of an MBE-grower's control, the *A*:*B*-site stoichiometry can be very finely tuned without needing to change source material. As such, the investigation into what gives MBE-grown material its performance begins with a study of stoichiometry.

3.1 Controlling composition of $Ba_xSr_{1-x}TiO_3$ by MBE

There have already been significant studies on the effects of *A*:*B*-site (Ba+Sr : Ti) stoichiometry on device properties, as discussed in 1.2.2. However, many of these studies find improved performance for *A*:*B* stoichiometries far from 1:1. Additionally, they tend to control stoichiometry by tuning a parameter which may also influence other materials properties [50], [51]. In contrast, growing BST via the hybrid MBE technique affords a high degree of control over stoichiometry [100], [112], as well as a

low concentration of point defects [81], [113]. While the study in Ref. [57] made efforts to grow nearly-stoichiometric BST, the fine (and under some conditions self-limiting) control over *A*:*B* site stoichiometry by hybrid MBE allows a more precise study of the effects of non-stoichiometry without requiring fabrication and replacement of BST targets. By the same token, Ba content (x) can also be varied controllably from 0-1 in $Ba_xSr_{1-x}TiO_3$.

Figure 3-1 shows out-of-plane lattice constants of BST grown on $SrTiO_3$ at various Ba contents. Each plot shows the behavior of lattice constant as *B*:*A*-site flux ratio is varied. For $SrTiO_3$, a lattice expansion is observed in both Sr-rich and Ti-rich conditions by XRD [100]. This trend is observed for Ba content up to 46%. At Ba composition around x = 0.6, there appears to be a slight lattice expansion under Ti-rich conditions, but lattice constant drops under *A*-rich conditions. For x ~ 0.65, the lattice constant has considerable scatter, making determination of stoichiometric conditions from XRD challenging.

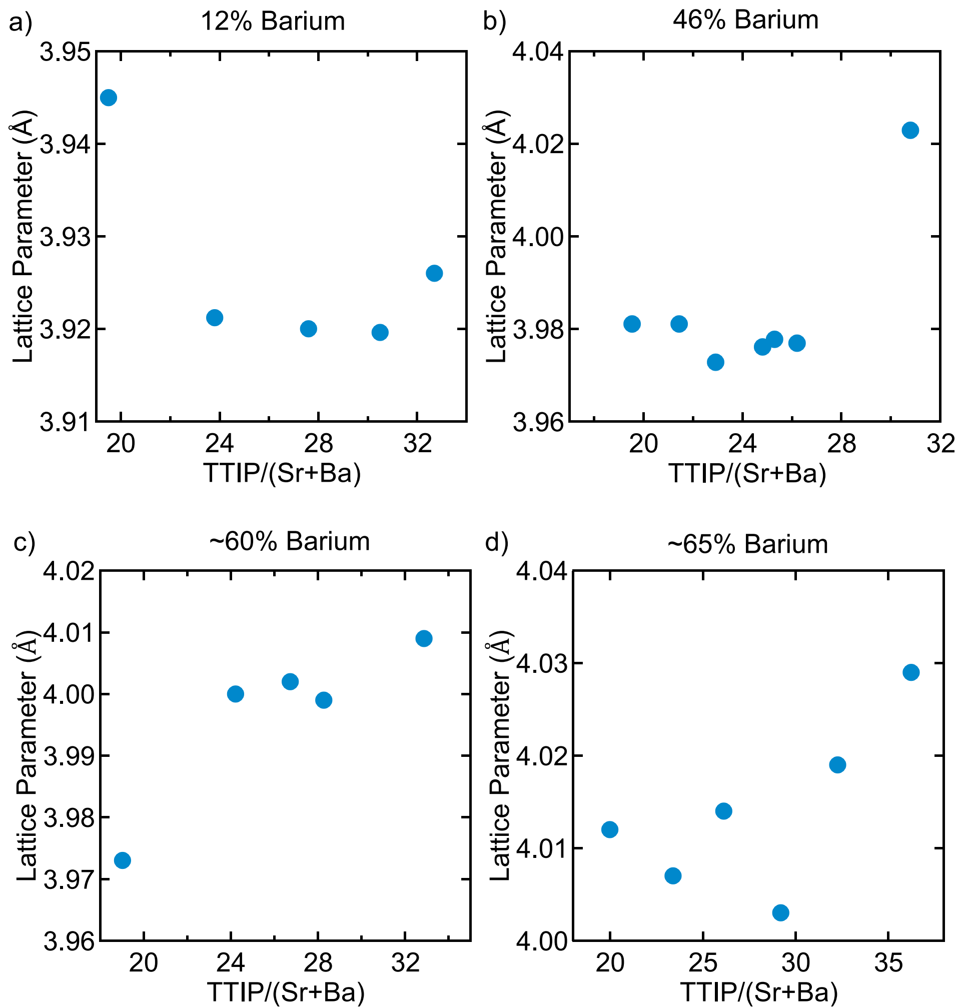

Figure 3-1: Strained out-of-plane lattice constants (determined by XRD) for ~60 nm BST grown on $SrTiO_3$ (001) with Ba content of a) 12%, b) 46%, c) ~60%, and d) ~65%. At each composition, *A*:*B*-site flux ratio is varied.

This scatter in Figure 3-1(d) may be related to the ferroelectric phase transition, which is known to happen at room temperature for x ~ 0.7, but which can be induced even in pure $SrTiO_3$ under the application of large strain. It is possible that at this composition (which is estimated from the lattice constant, assuming a cubic lattice), small shifts in Ba content and/or stoichiometry could be shifting the Curie temperature

around room temperature, thereby inducing a phase transition which changes the out-of-plane lattice constant so significantly. Another potential explanation is a diminishing growth window for these compositions, as the scatter in lattice constant resembles that of $SrTiO_3$ grown at low substrate temperature. While growth windows exist for $BaTiO_3$ [114] and $SrTiO_3$ [100], it has been suggested that for intermediate *A*-site compositions, the window may narrow [115]. Regardless, films with Ba content this high were not used to fabricate devices, since the tunability was high enough at low Ba composition and loss generally increases as Ba composition increases. While composition determination from XRD is challenging for x ~ 65%, it has previously been demonstrated that A-site composition (x) calculated from lattice constant matches closely with measurements by Rutherford Backscattering Spectrometry, which was done for *x* up to around 0.5 [57]. Figure 3-2 demonstrates that even up to x = 0.6, the 60 nm BST films in Figure 3-1 remain fully strained to the $SrTiO_3$ substrate. To calculate unstrained lattice constant, misfit strain is calculated, and out-of-plane strain is calculated using elastic constants for $SrTiO_3$ and $BaTiO_3$.

In-plane misfit strain is calculated by

$$\varepsilon_{xx} = \varepsilon_{yy} = \frac{a_s - a_f}{a_f}, \tag{3-1}$$

where ε is strain and a_s and a_f are the lattice constants of the substrate and film, respectively. For a cubic material with no shear strain, Hooke's Law (using Einstein notation) says

$$\begin{bmatrix} \sigma_{xx} \\ \sigma_{yy} \\ \sigma_{zz} \end{bmatrix} = \begin{bmatrix} C_{11} & C_{12} & C_{12} \\ C_{12} & C_{11} & C_{12} \\ C_{12} & C_{12} & C_{11} \end{bmatrix} \begin{bmatrix} \varepsilon_{xx} \\ \varepsilon_{yy} \\ \varepsilon_{zz} \end{bmatrix} \tag{3-2}$$

where C_{ij} indicate components of the material's elastic constant tensor. Rearranging this equation with $\varepsilon_{xx} = \varepsilon_{yy}$ gives simply

$$\varepsilon_{zz} = \frac{2 \cdot C_{12}}{C_{11}} \varepsilon_{xx} \quad (3\text{-}3)$$

Knowing that in-plane and out-of-plane lattice constant must be the same for the cubic material, the unstrained lattice constant can be calculated and used to estimate composition from Figure 1-5.

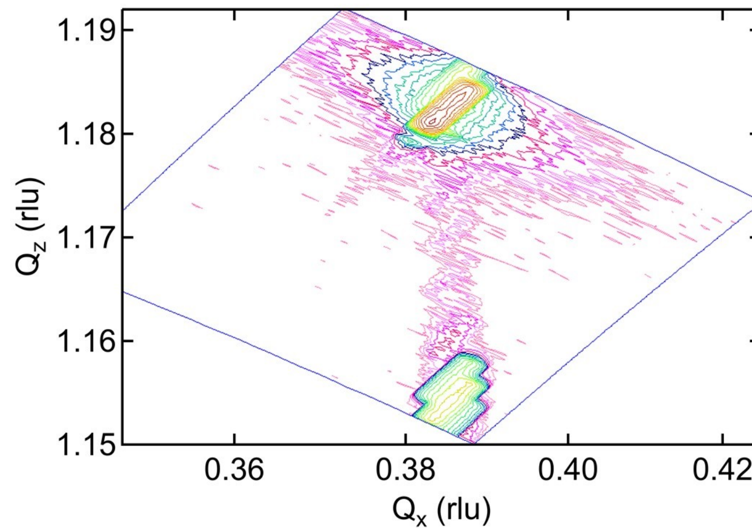

Figure 3-2: Reciprocal space map of the (103) reflection of a 60 nm $Ba_{0.6}Sr_{0.4}TiO_3$ film on $SrTiO_3$ demonstrating the film is fully strained to the substrate in-plane lattice constant.

3.2 *A*:*B* site stoichiometry and device performance

While the previous study of MBE-grown BST [57] was aiming only for stoichiometric growth conditions, it is important to understand how non-stoichiometry influences device properties. For the sputtered films, non-stoichiometry was found favorable for improving the reliability of BST devices [50]. To investigate the effects of *A*:*B* site stoichiometry, first a calibration series was grown of 60 nm BST on $SrTiO_3$. The typical

procedure was to then use the same growth conditions for stoichiometric BST on $SrTiO_3$ to then grow 280 nm BST on 100 nm Pt (001)/$SrTiO_3$ (001) substrates to fabricate parallel plate capacitors (thickness confirmed by x-ray reflectivity, XRR). Rather than grow a single 'stoichiometric' sample on platinized $SrTiO_3$, a full series of 280 nm thick BST was grown under the same conditions as the calibration series. A Ba composition of 0.3 was chosen for this series, since this previously provided a good balance in the trade-off between high *Q* and high tunability [116]. As seen in Figure 3-3a, the BST demonstrated a growth window at this composition, marked by an increase in out-of-plane lattice constant on either side of a plateau in lattice constant. In contrast, no such increase in lattice constant was seen for the BST grown on Pt (Figure 3-3b). An unstrained lattice constant of 3.928 Å was calculated for this calibration series on $SrTiO_3$, which is comparable to the lattice constant measured for the BST grown on Pt. It was confirmed via reciprocal space maps of the (103) that the ~280 nm thick BST films on Pt are fully relaxed.

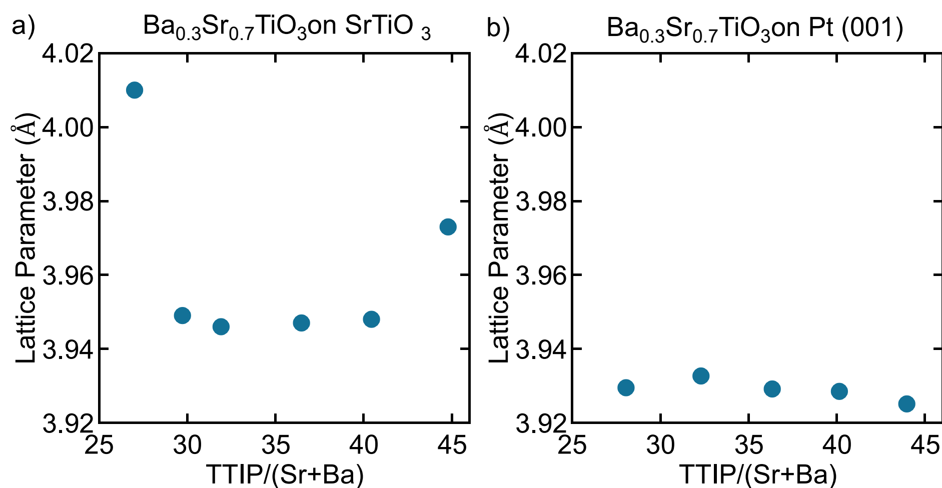

Figure 3-3: Measured lattice constant from XRD as a function of flux ratio for BST with x = 0.3 on a) $SrTiO_3$ (001) (~60 nm thick) and on b) 100 nm Pt (001)/$SrTiO_3$ (001) (~280 nm thick).

While XRD does not allow for distinguishing differences between the samples grown on Pt, in-situ RHEED and post-growth atomic force microscopy (AFM) show a great deal of difference. The results are summarized in Figure 3-4 for all five samples. From AFM, significant roughness is noted for all samples. It is for this reason that no thickness fringes are apparent in XRD, requiring thickness measurements by x-ray reflectometry. Nevertheless, samples which are more *A*-rich tend to have more features with higher roughness (see vertical scale size decreasing from left to right). For the most *A*-rich sample, with a ratio of 28, the surface is entirely covered by rough features, whereas the other samples have more prominent smooth areas with rough features scattered on top.

From surface reconstructions in RHEED, the samples with flux ratios of 36 and 40 look comparable to highly stoichiometric $SrTiO_3$ grown by hybrid MBE [112]. The areas of the sample surface in between raised features, which may be primarily due to other crystalline orientations besides BST (001), are also relatively smooth for these two ratios, with atomic steps visible in finer AFM scans. The prevalence of additional spots in RHEED also indicates fewer alternative orientations for these two samples, though there are brighter spots in the sample with a ratio of 40. For the other ratios, there is a diminished distinction between the diffraction patterns along the [100] and [110] directions, which is suggestive of the growth of alternate grain orientations. Note that there is no indication of rings in RHEED, which would be indicative of polycrystalline growth. The alternative directions that are seen here (and in XRD) remain discretized in their orientations to underlying Pt metal. To look at the effects of stoichiometry on device properties, Pt plate capacitors were fabricated from these samples by depositing

Pt top contacts and performing a mesa etch. Unless indicated otherwise, the samples discussed in this section were fabricated using Pt top contacts sputtered at high temperature after an oxygen anneal at 825 °C, as discussed in Section 2.2.

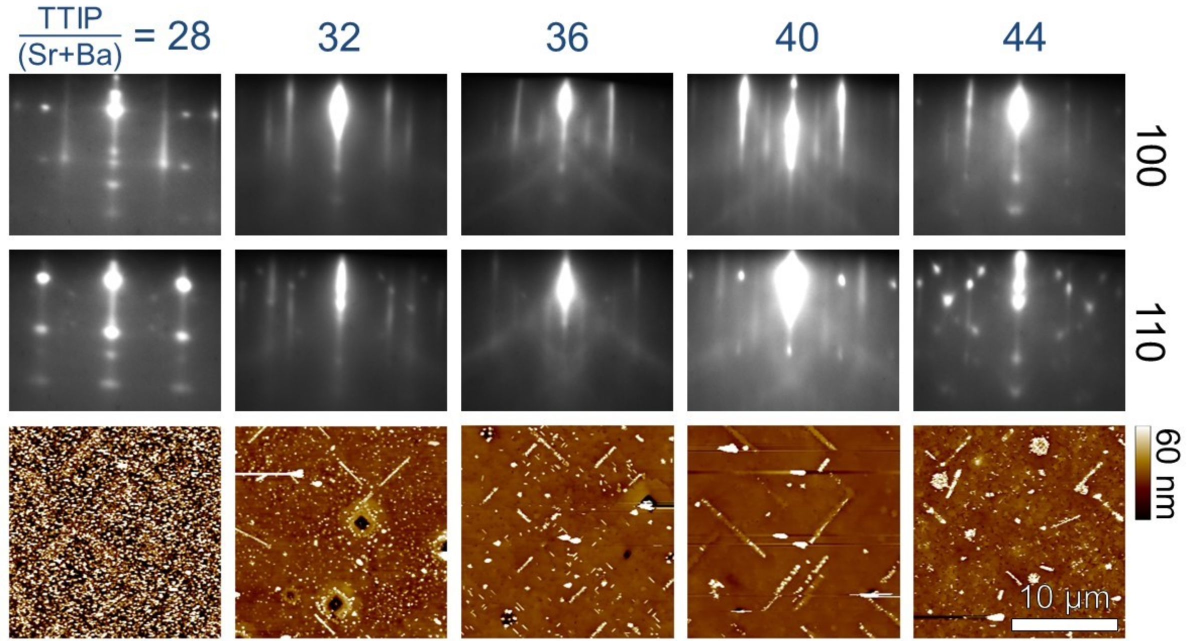

Figure 3-4: RHEED and atomic force micrographs of the BST series (x ~ 0.3) grown on 100 nm Pt (001)/$SrTiO_3$. AFM was taken after the post-growth oxygen anneal.

Figure 3-5 shows the measured zero-field Q as a function of frequency. The zero-field Q is highest for stoichiometry ratios of 36 and 40, which correspond to proper A:B-site stoichiometry. When shifting towards A-rich conditions, zero-field Q drops significantly. This is in contrast with previous results, which found that A-rich BST (grown by PLD) had lower dielectric loss than nominally stoichiometric BST [50]. However, the degree of control over stoichiometry by PLD (or sputtering) is not as fine as by hybrid MBE, which has a demonstrated growth window. In addition to the coarse stoichiometry control afforded by these techniques, the high-energy deposition

introduces a degree of damage [49] which may interact with point defects from non-stoichiometry in a manner which improves device performance for slightly non-stoichiometric films.

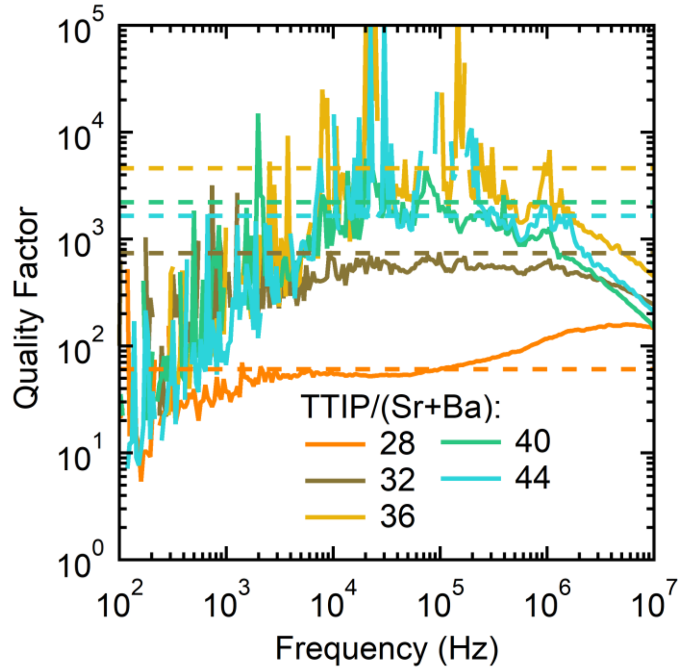

Figure 3-5: Q as a function of frequency for 45 × 45 μm^2 devices with sputtered top contacts under no DC bias. Measured data is shown with a solid line, while the dotted line shows calculated Q from eq. (3-5).

Figure 3-6 demonstrates that stoichiometry also affects the bias at which Q begins to drop off due to leakage. For the e-beam-deposited contacts, this occurs at roughly the same field (-0.15 MV/cm) for all stoichiometry ratios besides 28, which can be biased to much higher voltages. However, for sputtered contacts, higher flux ratio (trending towards B-site excess) correlates with lower achievable fields. While this trend appears very clear in Figure 3-6(b), the large variation between individual devices makes it difficult to confirm that the trend is monotonic with flux ratio.

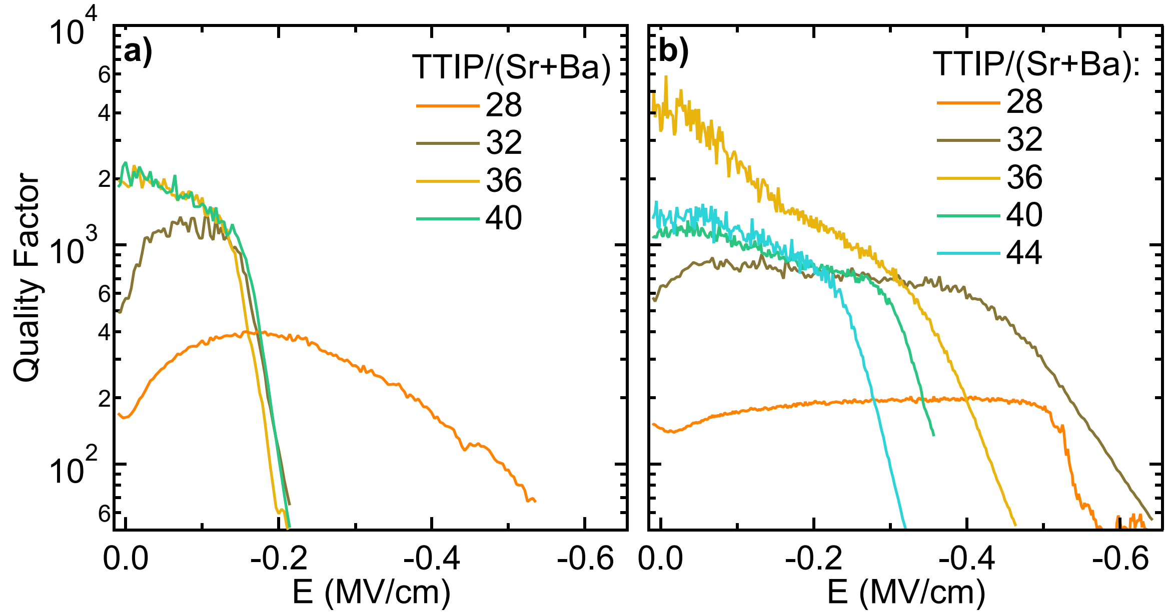

Figure 3-6: Measured Q as a function of applied field for (a) e-beam-deposited Pt top contacts and (b) sputtered top contacts at 1 MHz. Negative field is plotted since application of bias in this direction probes the breakdown from injection by the top interface. While zero-field Q is highest for stoichiometric samples (36, 40), A-rich stoichiometries can be biased further.

3.2.1 Verification of extraordinary quality factors

The large Qs observed in Figure 3-5 approach the measurement limits of the impedance analyzer, which is indicated in the high noise level for the samples with highest Q. For verification of the high Q values measured, a power-law fit to the frequency dependence of capacitance density was conducted according to Ref [23]:

$$C(f) = C_{HF} + C_0 \left(\frac{f}{f_0}\right)^{n-1} \tag{3-4}$$

Where C_{HF} is the high-frequency capacitance, and n has a value between zero and one. From this fit, Q can be calculated with eq. (3-5):

$$Q(f) = \left(\frac{C(f)}{C(f)-C_{HF}}\right) * \tan\left[\frac{(n*\pi)}{2}\right] \tag{3-5}$$

Figure 3-7 shows the measured capacitance as a function of frequency for each of these devices. Using eq. (3-4) and (3-5), Q was calculated from the trends in capacitance for each sample. The calculated Q for each sample is depicted in Figure 3-5 by a dotted line. As seen from this figure, the calculated Q is slightly higher than the measured value, demonstrated that the extremely high Q values measured are likely real. The exponents for the fits to capacitance are shown in Table 3-1. The exponent n relates to the maximum quality factor in Region II of Figure 1-11, where a higher exponent indicates a higher maximum quality factor. These exponents are extremely close to 1, the maximum theoretical value they could reach.

Table 3-1: Extracted exponent from fits to capacitance as a function of frequency for the stoichiometry series grown on Pt.

TTIP/(Sr+Ba)	28	32	36	40	44
n	0.99276	0.99838	0.99975	0.99965	0.99841

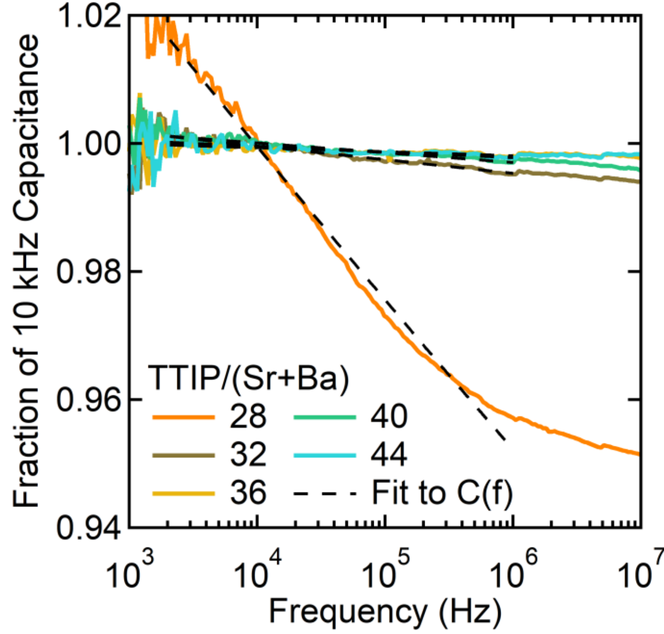

Figure 3-7: Measured capacitance as a function of frequency for films with different stoichiometry. Fitting to eq. (3-4), we can calculate expected *Q*.

3.3 Improving the interface between BST and top contacts

For extremely-large dielectric constant materials, such as BST, the presence of an additional series capacitance is extremely detrimental to device performance [13]. For series-connected capacitors,

$$\frac{1}{C_{tot}} = \frac{1}{C_{BST}} + \frac{1}{C_{int}}, \tag{3-6}$$

such that the tuning voltage $$V_{BST} = V_{tot} \cdot \frac{C_{tot}}{C_{BST}}. \tag{3-7}$$

Previously there was some speculation as to the cause of this series capacitance [117]. It is now understood to come from the adsorption of contaminant hydrocarbons onto the surface. These hydrocarbons are known to begin adsorbing on $SrTiO_3$ (and likely BST by extension) almost immediately upon exposure to air [118], [119]. This contaminant

layer is extremely persistent, and can be removed in UHV under oxygen plasma at 870 °C (but not at 800 °C) [118], [120]. This layer has a very low dielectric constant relative to BST, which itself can be much greater than 1000. As such, it typically dominates C_{tot}, despite its relatively low thickness. The smaller this capacitance (i.e. thicker this interlayer), the more of the applied voltage is shared to the interfacial layer. This is detrimental because it is the voltage applied across the BST that is required for good tunability.

Work has already been done to look at the role of surface cleanliness on interfacial capacitance for devices made with $SrTiO_3$ [56]. This study demonstrated a significant change in trapped charges at the interface based on the cleanliness of the Pt/Nb:$SrTiO_3$ interface. For lower-quality interfaces, this trapped charge could be modulated more significantly (either in charge density or in spatial location with respect to the interface). This modulation tunes the effective barrier height of the Pt/Nb:$SrTiO_3$ contact and leads to a significant hysteresis in the I-V, giving the low- and high-resistance states characteristic of resistive switching. Furthermore, the ideality factor is improved from 1.80 and 2.74 (in the high- and low-resistance states, respectively) to 1.19 and 1.39 with improved interface cleanliness. The ideality factor, n, describes the deviation of the I-V relationship from ideal thermionic emission, with the ideal thermionic emitter having $n = 1$. In this case, the deviation from ideal behavior stems from a voltage-dependent barrier height, which is typically linked to the presence of an insulating interface layer or surface states [56]. While the interfacial layer's impact on the device properties could not be eliminated entirely, the effects were greatly

diminished, as seen by the ideality factors very close to 1. The present work leverages similar processing to vary interface cleanliness from most clean (high-temperature anneal under oxygen flow, followed by high-temperature sputtering of the Pt top contact) to less clean (low-temperature electron-beam evaporation of the Pt top contact with no *in-situ* clean/anneal) to study the specific effects of interfacial capacitance on device performance.

3.3.1 Effects of interface cleanliness on quality factor

As seen in Figure 3-6, tuning voltage where leakage causes Q to drop is highly dependent on top interface cleanliness. Note that the sweeps shown are under negative bias, such that breakdown should occur because of charge injection at the top interface, rather than the bottom interface (which should be the same for both sets of devices). For the devices with e-beam-deposited contacts, Q begins dropping due to leakage at only -0.15 MV/cm for all but the most A-rich sample. This is attributed the lower interface capacitance stemming from the less-clean interface between the BST and the top contact. In contrast, the devices with sputtered top contacts (having higher interfacial capacitance) seem to have usable bias ranges which are dependent on sample stoichiometry instead of contact quality. There is no clear trend between interfacial capacitance and peak device Q apparent in Figure 3-6.

3.3.2 The role of interfacial capacitance on tunability

The interfacial capacitance has previously been extracted by measuring the variation of capacitance with film thickness for Pt-BST-Pt parallel plate capacitors [119]. Instead

of growing a thickness series, here we attempt to fit to the empirical approximation for tunability eq. (1-4). The relative simplicity of the empirical calculation is why the empirical relation is used in the fits below. We note that this equation only considers the dielectric constant associated with the tunable material. As mentioned previously, this interfacial capacitance not only reduces the overall capacitance of the parallel plate structure, but also parasitically reduces the voltage dropped over the tunable layer (i.e. tuning voltage, V_B). This voltage relationship can be described as follows:

$$V_B = E_B * (t - t_i) = V_{App} * \frac{\epsilon_i / t_i}{\epsilon_i / t_i + \frac{\epsilon_B(E_B)}{t - t_i}} \tag{3-8}$$

where E_B and ϵ_B are the electric field within and dielectric constant of the tunable material, respectively, and ϵ_i/t_i is the interfacial capacitance. Note that separating ϵ_i and t_i is unnecessary, and the two terms can be left lumped. From eq. (3-8), we see that when the interfacial capacitance term is very large, the device will then behave like the model in eq. (1-4). The fits to eq. (3-8) are shown in Figure 3-8.

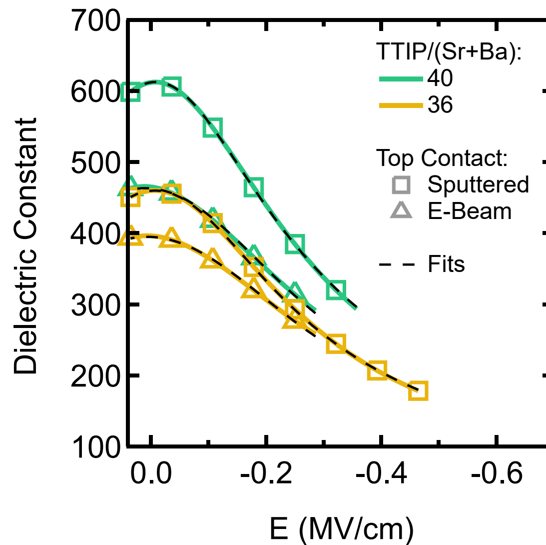

Figure 3-8: Tunability measured in the dielectric constant for devices with stoichiometric BST at 1 MHz. Solid lines indicate measured data, while dotted lines show fits to tunable capacitance as described by the empirical relation given in eq. (1-4) and (3-8). Reprinted from [C. R. Freeze and S. Stemmer, "Role of film stoichiometry and interface quality in the performance of $(Ba,Sr)TiO_3$ tunable capacitors with high figures of merit," *Applied Physics Letters*, vol. 109, no. 19, p. 192904, 2016.], with the permission of AIP Publishing.

Each BST sample investigated here has a pair of parallel plate capacitors which differ only by the method with which the top contact is deposited. As such, the material properties, ϵ_B and *b,* should be identical for each pair once extrinsic contributions (such as the interfacial capacitance) are accounted for. Using these constraints to inform the fits from eq. (3-8), we attempt to separate interfacial capacitance from the tunable dielectric properties. After performing initial fits, however, the shapes of the curves were very poorly described for the flux ratio of 40, resulting in impractically large numbers for the interfacial capacitance for a flux ratio of 40 with sputtered top contacts. To remedy this, *b* was freely refined in the fits shown (Figure 3-8). The results of the fits

are summarized in Table 3-2. We note that even though *b* was not constrained within each sample set, the variation seen from the fits is small (especially for the flux ratio of 36). In addition, the measured tunability for both flux ratios is very close together, and sputtered contacts yield higher measured tunability than e-beam contacts. For comparison, the tunability of each device is shown at -0.25 MV/cm in Table 3-2. The difference in tunability can be explained by the enhancement of the interfacial capacitance for the sputtered top contact through a reduction or elimination of the interfacial layer. For these samples, the interfacial capacitance is enhanced by a factor of two to four for the different stoichiometries investigated here.

To confirm that the extracted numbers are reasonable, we compare to Schottky Pt contacts on stepped $SrTiO_3$ substrates [56]. For contacts deposited under conditions identical to that for e-beam contacts in this study, an interfacial capacitance of approximately 8 nm^{-1} was reported, while the fits here give a value of approximately 5 nm^{-1}. For the same conditions as sputtered contacts in this study, 64 nm^{-1} was reported compared to 8 nm^{-1} to 19 nm^{-1}. While the values extracted from the fits in this study are lower, there are also two interfaces for the parallel plate capacitors (which each contribute their own series capacitance) instead of one. Additionally, the top interface in the present study, while containing atomically-stepped regions, also has features that increase the roughness, and these may contribute to reduced interfacial capacitance.

While most of the extracted parameters are unsurprising, the zero-bias BST dielectric constant varies significantly between the two flux ratios shown. This is surprising since both have the same Ba:Sr ratio and may only vary in *A*:*B* stoichiometry

to a small degree (especially if both are truly within a stoichiometric growth window). We expect this may be explained partially by the lower roughness at the interface between the BST and the top contact for the flux ratio of 40 [102]. While this difference may be large, care should be taken in assuming these are the correct values for BST dielectric constant. From the tunability relationship derived from Landau-Ginzberg-Devonshire theory in eq. (1-5), a calculation was completed for the same film with a non-tunable series capacitance (such as an interfacial capacitance) [18]. From this derivation, it was found that the impacts of this non-tunable series capacitance could be lumped into the peak dielectric constant (ϵ_{max}) and the tuning voltage (V_2) without changing the form of the equation at all. The same fits for eq. (1-5) are shown for the same data in Figure 3-9. While these fits do not represent the data as well as the fits to the empirical relation in Figure 3-8, the extracted parameters are included in Table 3-2. The higher value of each pair of measured dielectric constants here should be seen as a lower bound for the dielectric constant of the BST layer.

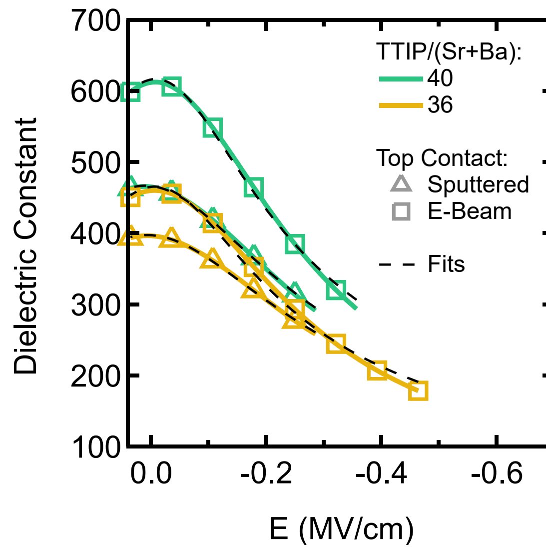

Figure 3-9: Tunability measured in the dielectric constant for devices with stoichiometric BST at 1 MHz. Solid lines indicate measured data, while dotted lines show fits to tunable capacitance as described by Landau-Devonshire-Ginzburg theory in eq. (1-5). Reprinted from [C. R. Freeze and S. Stemmer, "Role of film stoichiometry and interface quality in the performance of (Ba,Sr)TiO_3 tunable capacitors with high figures of merit," *Applied Physics Letters*, vol. 109, no. 19, p. 192904, 2016.], with the permission of AIP Publishing.

Though literature has previously mentioned the presence of an offset to the C-V peak as indication of non-stoichiometry [13], small offsets remain for both sets of samples. Though relatively small offsets occur, the sign of the offset appears related to the top contact deposition method – with a small positive offset for e-beam contacts and a small negative offset for sputtered contacts. This trend follows for the other flux ratios not shown in Figure 3-8 as well, with the notable exception of 28 (for which the signs of the offsets are reversed). However, the data presented here is a small sample set, and requires more study to verify this trend.

Table 3-2: Extracted material parameters and interfacial capacitances for the curves shown in Figure 3-8 and Figure 3-9. Also shown is the measured tunability of each device $\left(n = \frac{C(E=0)}{C(E)}\right)$ at a field of 0.25 MV/cm to demonstrate the impact of the interfacial capacitance. Reprinted from [C. R. Freeze and S. Stemmer, "Role of film stoichiometry and interface quality in the performance of $(Ba,Sr)TiO_3$ tunable capacitors with high figures of merit," *Applied Physics Letters*, vol. 109, no. 19, p. 192904, 2016.], with the permission of AIP Publishing.

	TTIP/(Sr+Ba) = 36		**TTIP/(Sr+Ba) = 40**	
Fit Parameter	Sputtered	E-Beam	Sputtered	E-Beam
n (E = 0.25 MV/cm)	1.57	1.43	1.59	1.48
To eq. (1-4)				
$\epsilon_B(0)$	575		692	
b (MV/cm)	87.3	89.7	116.0	99.7
$\frac{\epsilon_i}{t_i}$ (nm^{-1})	8.2	4.5	19.2	5.0
E_0 (MV/cm)	-0.007	0.007	-0.008	.010
To eq. (1-5)				
$\epsilon_{B,\ app}(0)$	466	397	617	467
E_2 (MV/cm)	0.343	0.458	0.345	0.433

3.3.3 Field dependence of Q, and the dip at low bias

In much of the literature regarding BST, a notable feature is the sharp rise in Q upon the application of a small bias, and a continued gradual rise as more bias is applied [51],

[121]–[125]. The present study only observes this feature in capacitors with stoichiometry ratios of 28 and (for low voltages) 32, but not for stoichiometric samples or Ti-rich samples in this study, as demonstrated in Figure 3-6. We also note that due to inconsistency between devices on each sample, the bias range over which the Q rises varies significantly. For instance, some of the devices with a flux ratio of 32 showed the sharp rise in Q below 0.1 MV/cm, with a continued gradual rise until 0.4 to 0.5 MV/cm. In contrast, almost none of the devices with a flux ratio above 32 demonstrated any rise in Q with bias. Nevertheless, it is the sharp rise at low bias that is the subject of discussion here.

Among the BST literature, there tends to be wide agreement that Q is typically highest under bias, and lower near zero field [13], [125]. This trend is often referred to as an increase in Q under the application bias. Though the rise in Q with bias is ubiquitous in the literature, it is not adequately addressed. Except for quasi-Debye loss and DC leakage, nearly all other loss mechanisms are suppressed by lowering the dielectric constant, as discussed in Section 1.1.1.2. As such, the suppression of the dielectric constant (by applying voltage) should cause Q to rise if it is not limited by one of these two contributions. Based on the high Q observed with MBE-grown material, we suspect that the rise in Q upon the application of bias in previous studies was due to the suppression of extrinsic loss mechanisms not seen for most of the samples here. Instead of a rise in Q under the application of bias, we suggest that it should be viewed a drop in Q near zero bias instead.

In fact, for the stoichiometric samples in this study (with flux ratios of 36 and 40), a gradual drop in *Q* is observed as bias is applied instead of a rise. A closer look at quasi-Debye loss offers a possible explanation. By definition, quasi-Debye loss is not possible in centrosymmetric crystals [20] such as bulk BST with $x < 0.7$, which has a cubic crystal structure at room temperature. Because of the motion of the Ti^{4+} atom, DC bias breaks this centrosymmetry, thereby reducing *Q* as this loss mode is activated.

Upon further investigation, the dip in zero-bias *Q* could be induced (at least slightly) for even the stoichiometric samples. By increasing the AC probe amplitude to 500 mV (~0.018 MV/cm), the depth and width of the dip in *Q* is increased for all samples, as seen in Figure 3-10. While the dip stops being apparent below 50-100 mV for the stoichiometric samples, it remains clearly apparent in the *A*-rich sample even down to 25 mV.

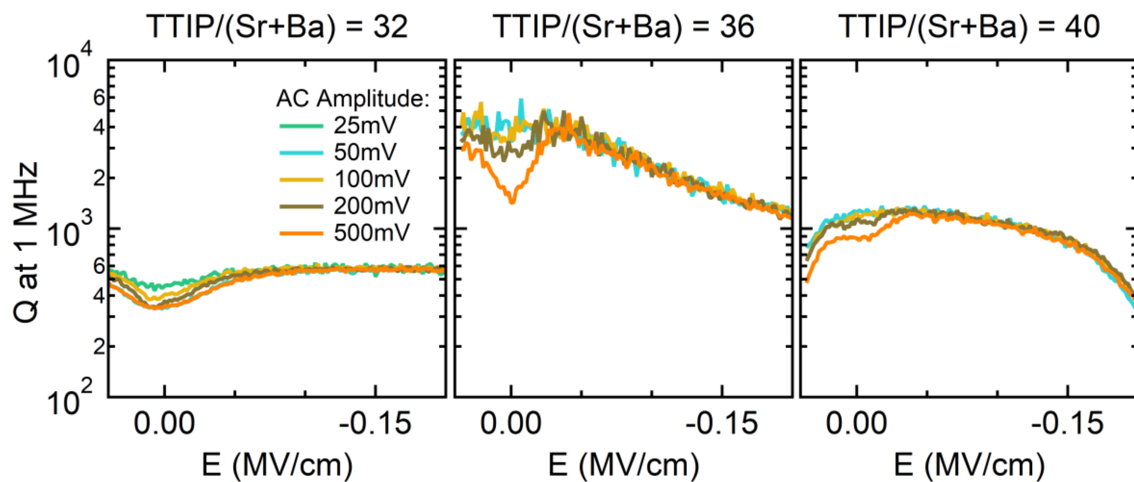

Figure 3-10: *Q* as a function of bias for samples with flux ratios of 32, 36, and 40 at $f = 1$ MHz. In these sweeps, AC probe amplitude is varied from as low as 25 mV to 500 mV. Scans are typically done with $V_{AC} = 50$ mV.

This dip near zero bias may be a result of secondary harmonic generation in the tunable capacitor [126]. This effect is more pronounced for tunable capacitors where the curvature of the capacitance with respect to applied DC bias is highest. This is most pronounced for tunable BST capacitors near zero bias. Additionally, a more sharply-peaked *C* as a function of bias exaggerates this effect. Figure 3-11 shows the dielectric constant (proportional to C) as a function of applied DC field for the range of cation stoichiometries discussed previously. As seen from the figure, the curve is much sharper at zero bias for the flux ratio of 32 than for 36 or 40. This is in agreement with the dip at zero bias that does not disappear for smaller AC amplitudes for the devices with a flux ratio of 32.

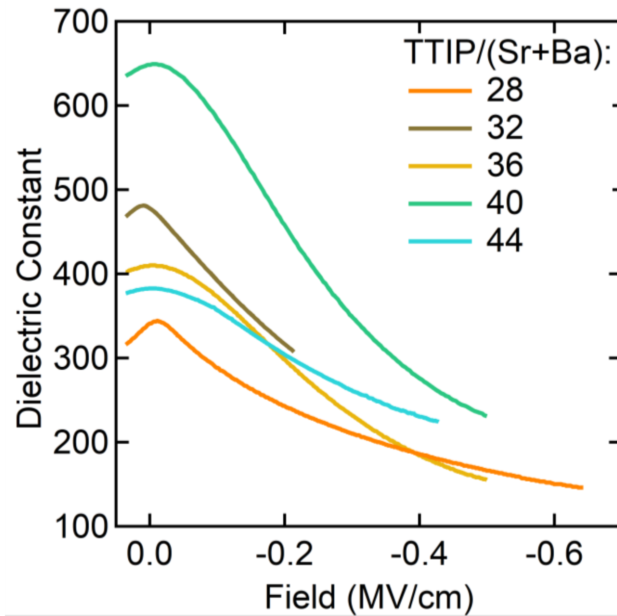

Figure 3-11: Dielectric constant as a function of applied DC field measured at 1 MHz for samples with varying cation stoichiometry.

3.4 Device Leakage

In the low-frequency region I of Figure 1-11a, Q is limited by parallel conduction, or leakage. In this regime, we can describe the device properties by the equivalent circuit shown in Figure 1-11b. Because the impedance analyzer takes measurement data as paired capacitance and parallel conductance at each frequency point, the leakage can be measured simply by looking to the conductance data, for which there should be a plateau at low frequencies. This data is shown at bias ranging from 0 V to 13 V for devices with cleaned/sputtered top contacts and for the flux ratio of 36 in Figure 3-12. There is a significant amount of noise, on the order of several nS. However, at low bias, the parallel conductance due to leakage is lower than the instrument's noise floor. This is why there are gaps in the data, where the 'measured' conductance drops below zero (and does not show up on a log scale). Typically, parallel conductance gradually increases, starting as soon as bias is applied [13]. For this device, however, there is a negligible increase in leakage until almost 9 V of bias.

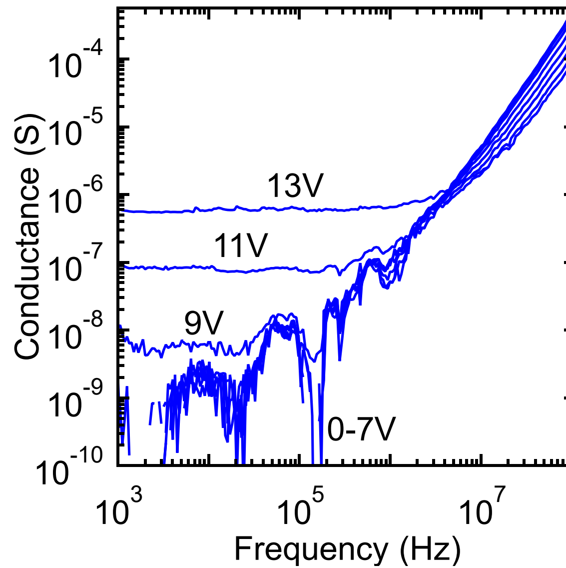

Figure 3-12: Parallel conductance for measured from 0 V to 13 V (only odd integers and zero shown). The device measured is the sample with flux ratio of 36 with sputtered top contacts.

3.5 Extrinsic factors from device design

As described in Section 1.2.3.2, extrinsic device factors play a strong role in the frequency dependence of the Q. These factors effectively determine the frequency range in which the device has the highest performance (region II in Figure 1-11a). The two main factors for extrinsic device losses stem from series resistance and parallel conduction through the device periphery, which is varied by changing device size. Series resistance leads to a drop in Q at the high end (region III). There are also several other device design considerations that can limit performance which will be discussed in this section.

3.5.1 Calculating series resistance

For devices with Qs strongly limited by series resistance (region III in Figure 1-11a), we can describe the properties with the equivalent circuit shown in Figure 1-11c. To extract series resistance, we fit to

$$Q = \frac{1}{\omega \cdot C \cdot R_s} \tag{3-9}$$

using Q and C from the impedance analyzer measurements. These fits to the data are shown for most sample stoichiometries and devices with both methods of top-contact deposition in Figure 3-13. The series resistances calculated from these fits are summarized in Table 3-3. While most of the devices demonstrate the characteristic $1/\omega$ slope at these frequencies, the most Ba-rich sample does not. This is related to the lower device capacitance, since the extracted series resistance values are higher than most of the other devices.

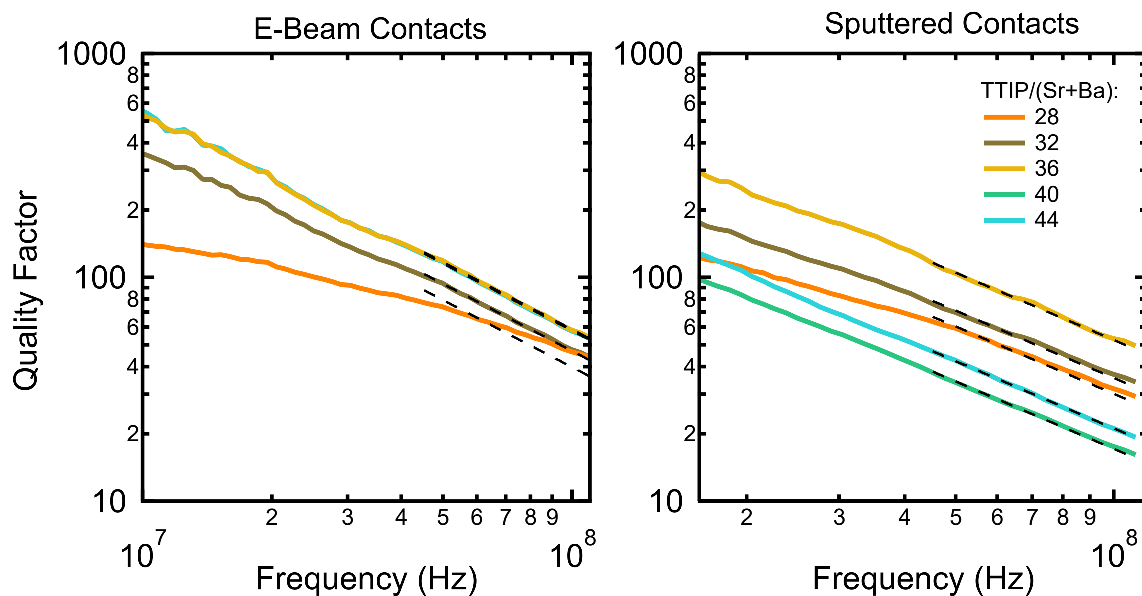

Figure 3-13: Qs as a function of frequency shown in the high-frequency range, where series resistance dominates the device properties.

As seen from the table, all samples have a series resistance on the order of 1 Ω. Surprisingly, the series resistances are almost all higher for the samples with sputtered top contacts, despite the higher quality interface associated with this deposition method. For the sputtered top contact, the series resistance is lowest for the sample with a flux ratio of 36, while for the e-beam deposited top contacts a minimum is seen at a ratio of 40. In literature, this series resistance is found to vary with device area, such that $R_s = r_c/A$ [13]. Other work has shown a series resistance near 1 Ω for devices regardless of size (12 ×12 μm^2 to 45×45 μm^2) at 1 MHz [52]. However, it is also shown that the measured series resistance is related to the contact area of the probes used. Like with this work, 100 nm Pt top contacts were used, and probed with sharpened GGB-brand GSG probes with 100 μm pitch and tips sharpened for 12×12 μm^2 devices. However, they found that contact resistance was directly proportional to the contact area of the probes used – when switching to probes with a footprint of 30×30 μm^2, the series resistance dropped to 0.15 Ω. The author notes that this resistance ratio of 6.7 is comparable to the area ratio of 6.25. The GSG probes used in the present study are sharpened for use on 12×12 μm^2 devices, and the previous study with similar probe size measured a minimum series resistance of 1 Ω. This series resistance minimum in this study is measured to be around 1 Ω as well.

Table 3-3: Extracted series resistance (R_s) for devices extracted from impedance analyzer measurements at high frequencies according to eq. (3-9) (measured in Ω).

Device R_s (Ω)	**Sample's Flux Ratio**				
Top contact	**28**	**32**	**36**	**40**	**44**

Sputtered	2.38	1.42	1.03	2.37	3.03
E-Beam	2.02	1.15	1.07	1.00	-

3.5.2 Device size effects (P/A)

It is shown that, in the absence of extrinsic device effects like resonance or roll-off from series resistance, Q at 1 MHz translates well to high frequency properties [23]. Extrinsic device properties must be more-carefully considered when fabricating devices for these high frequencies, since the high dielectric constant requires small devices to push the $1/\omega R_s C$ roll-off to higher frequencies (it can require on the order of $1 \times 1\ \mu m^2$ for BST parallel plate capacitors at low GHz). However, there is a trade-off in other properties when moving to smaller device sizes. One of the most important observations is the reduction in Q as the ratio of the perimeter length (P) to the area (A) of parallel plate capacitors increases – i.e. moving to smaller device sizes.

3.5.2.1 Effects of device size on Q

The size dependence can be explained by looking at the ratio of device periphery to area (P/A), as depicted in Figure 1-8b. Eq. (3-10) shows the dependence of Q on P/A by considering a linear conductance density around the periphery:

$$Q = \frac{\omega c}{g_\mathrm{d}}\left(1 + \frac{G}{g_\mathrm{d}}\left(\frac{P}{A}\right)\right)^{-1} \tag{3-10}$$

Here c is the capacitance density, g_d is the material's conductance density and G is a linear conductance density. This model considers a capacitor and two parallel resistances, as shown in Figure 3-14. Here, C and R_Bulk (related to c and g_d, respectively)

scale with device area. In contrast, R_P (related to G) is a periphery-dependent leakage, which scales differently than the other two elements. Note that for a capacitor with no conductance along the periphery (i.e. $R_P \rightarrow \infty$), this simplifies to the standard equation for Q (and the standard circuit model of a capacitor with parallel resistance for leakage). This size effect is summarized in Figure 3-15 for capacitors ranging from 12×12 μm^2 to 45×45 μm^2 [127].

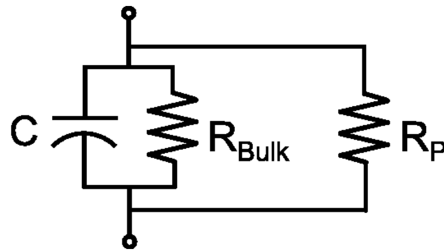

Figure 3-14: Equivalent circuit model for the periphery-dependent leakage described by

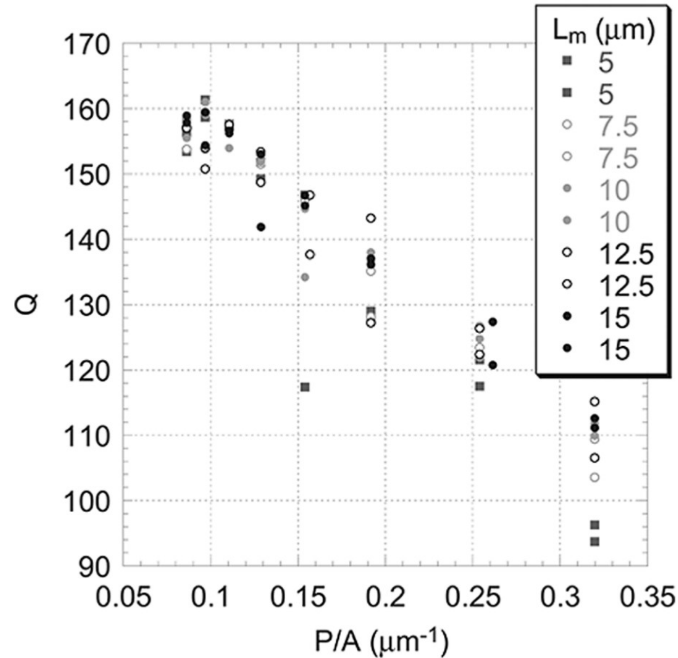

Figure 3-15: Effects of device periphery on Q (at 1 MHz) for $Ba_{0.5}Sr_{0.5}TiO_3$ parallel plate capacitor devices grown by Nadia Pervez ranging in size from 12×12 μm² to 45×45 μm². L_m indicates the spacing between the edge of the top contact and the etched mesa edge, or "mesa ledge width" (as depicted in Figure 1-8b). Reprinted with permission from [N. K. Pervez and R. A. York, "Geometry-Dependent Quality Factors in $Ba_{0.5}Sr_{0.5}TiO_3$ Parallel-Plate Capacitors," *IEEE Transactions on Microwave Theory and Techniques*, vol. 55, no. 2, pp. 410–417, 2007.] © 2007 IEEE. (Ref. [127])

As seen from eq. (3-10), this additional source of loss is a direct result of parallel conduction through the device periphery, presumably related to conductive surface states. When looking at the contributions of the mesa ledge width (L_m), which is the spacing between the edge of the top contact and the edge of the etched mesa, there doesn't appear to be a strong contribution. This periphery conduction highly dependent on the P/A ratio, but it shows very little change for dramatically different mesa ledge widths. This occurs despite the (nearly) two orders of magnitude difference in length

between the mesa ledge width and BST film thickness (approximately 135 nm for the devices in Figure 3-15 [127]). This suggests that the periphery conduction is more related to populating and depopulating surface states near the contacts.[13] If this is the explanation, it would yield a frequency-dependent parallel conduction term that is not necessarily present at low frequency (i.e. DC leakage), and that becomes more dominant as the frequency increases. It is unclear if these states are caused by etch damage or inherent to the BST-air interface.

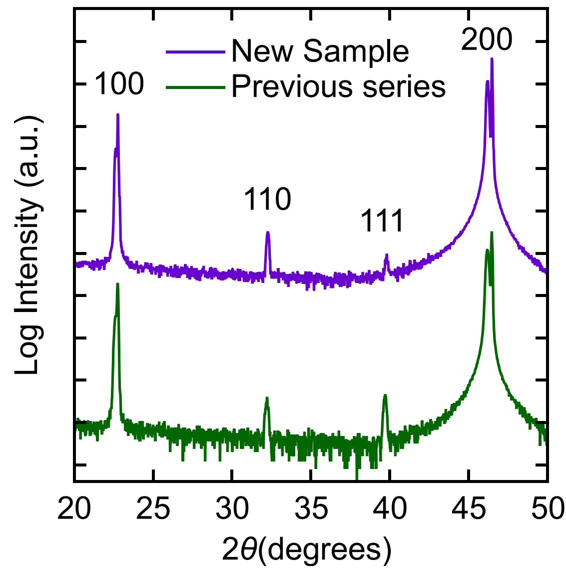

Figure 3-16: Wide-angle XRD demonstrating the presence of additional orientations in the BST/Pt films after BST growth. The new sample has a re-optimized Pt (001) back contact (on an $SrTiO_3$ substrate) to reduce the off-orientation BST grown on it. The previous sample is from the series discussed earlier with a TTIP/(Sr+Ba) flux ratio of 36.

To investigate the strength of this effect for MBE-grown material, which are of higher quality, another sample was grown. Before the growth of BST by MBE, the Pt (001) growth conditions were optimized for higher-quality Pt with fewer rough defects on the surface. This was done primarily by adjusting the sputtering power, but also

moderately increasing substrate heater temperature from 825 °C to 835°C. Once again, BST with x ~ 0.3 was chosen for its combined high tuning and low loss. Figure 3-16 compares wide angle XRD of the new sample for etching studies with the XRD from a stoichiometric sample from the previous series (the sample with TTIP/(Sr+Ba) = 36). As seen from the figure, the BST (111) peak is much less prevalent, though the (110) peak has similar intensity. The differences in sample quality can be seen much more clearly in AFM, which is shown for the new sample in Figure 3-17. In comparison to the AFM in Figure 3-4, the surface is clearly much smoother, with fewer large features.

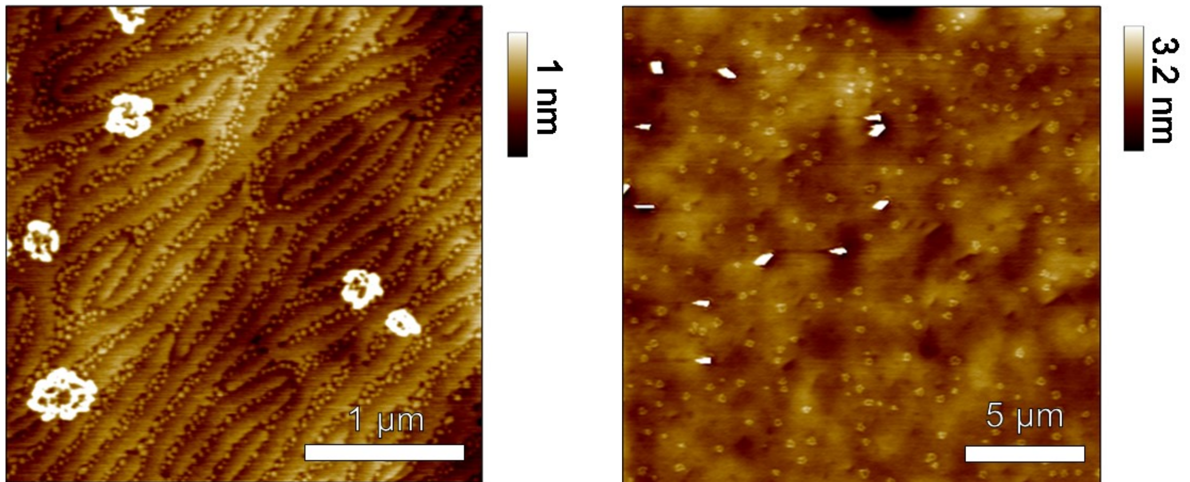

Figure 3-17: Atomic force micrographs of the BST sample surface used to investigate how the degree of etch damage effects the device-size effects described in eq. (3-10).

Using this newly optimized BST-on-Pt sample, parallel plate capacitors were fabricated by blanket sputtering Pt (001) at 835 °C following a 2 hour *in-situ* anneal under 10 mTorr O_2 flow (the same conditions as the 'sputtered' top contacts discussed previously). Once again, contacts were patterned by Ar ion milling the Pt contact using a photoresist mask. Two different etches were compared for the mesa etch – ion milling the BST film and wet etching with 1:20 H_2O:HF. To account for the over-etch of BST,

Pt back contacts were thickened by e-beam evaporating more Pt, which was lifted off from the mesa. Figure 3-18 shows the *Q* as a function of frequency for both sets of devices.

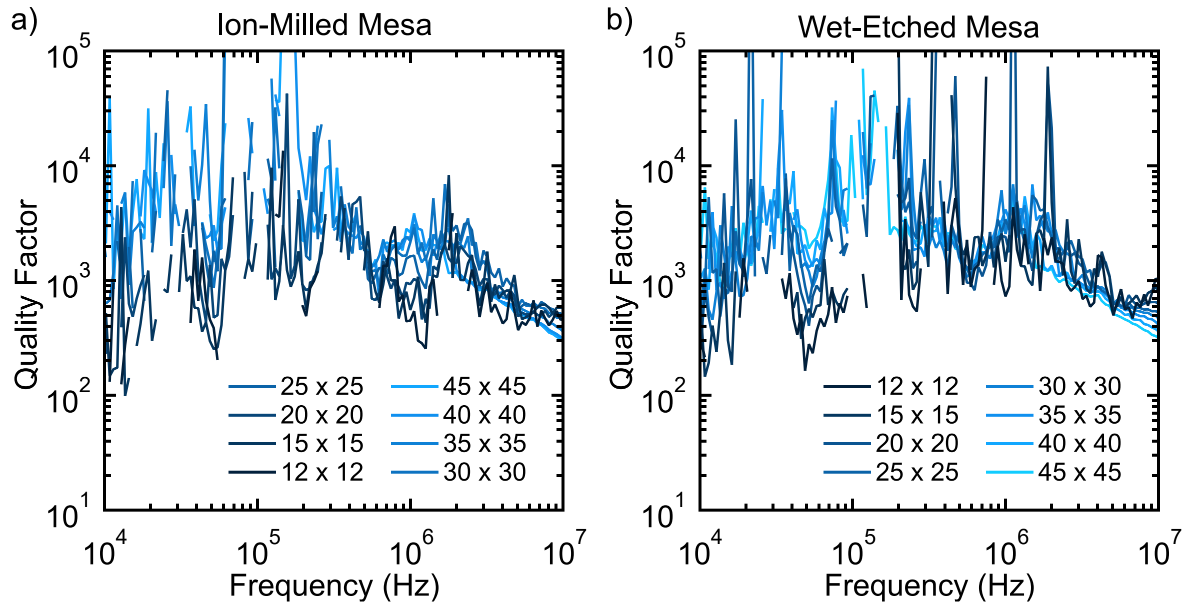

Figure 3-18: Plots of *Q* as a function of frequency for parallel-plate devices of varying size (in μm) with mesas etched by a) Ar ion mill and b) 1:20 HF:H_2O.

As discussed, there appears to be a drop in maximum *Q* as the device size is decreased. However, as a result of the significant noise in these measurements, exact conclusions on the trends in *Q* are difficult. Nevertheless, Q at 1 MHz is plotted as a function of P/A for both sets of devices in Figure 3-19 along with fits to eq. (3-10). As seen from the figure, the trend in *Q* is not accurately explained by eq. (3-10). More precisely, there appears to be disagreement between the low and high *P*/*A* for the set with the wet-etched mesa. This drop at higher *P*/*A* may be partially due to the resolution limits to the impedance analyzer setup. Figure 3-20 depicts the error in the impedance measurement as it relates to the device impedance and measurement

frequency. For a capacitor with $Z = -j/\omega C$, this gives a diagonal line shown in the figure. For our capacitors, the highest-accuracy region is barely achieved for the 45×45 μm^2 capacitors at 1 MHz. As capacitance is reduced, the error increases more than three-fold. Thus, the lower Qs measured at the smallest device sizes in may be a result of measurement inaccuracy, rather than performance that is much lower than the trend seen in the rest of the set.

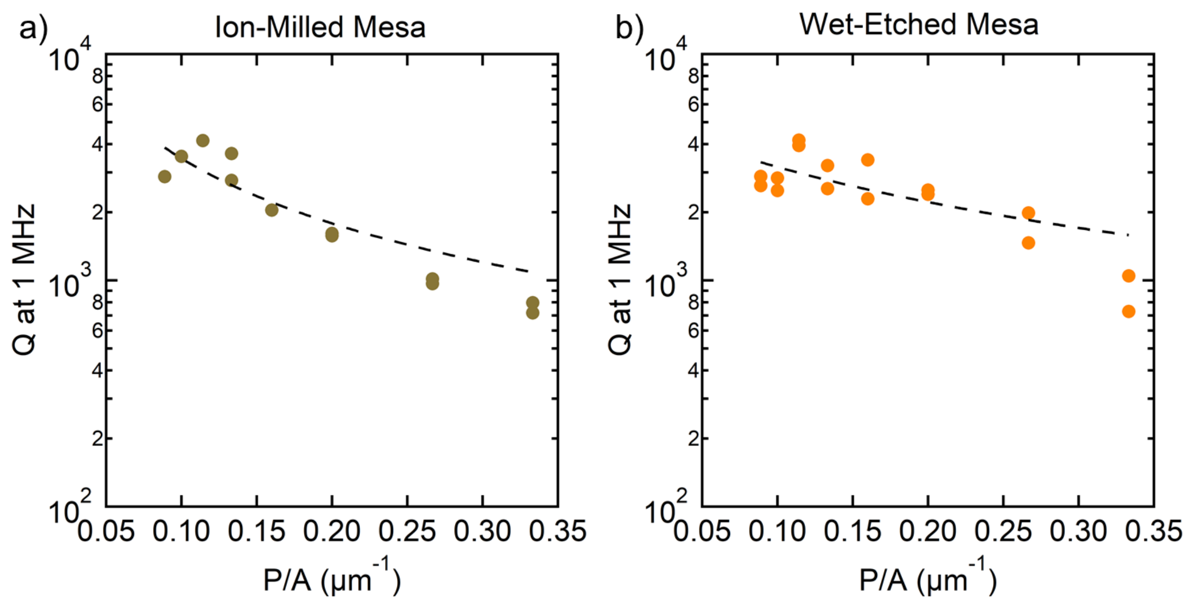

Figure 3-19: Measured Q (at 1 MHz) as a function of the ratio of perimeter length to contact area for devices fab ricated with the BST mesa etched by either a) ion milling or b) wet etch with 1:20 HF:H_2O. Fits to eq. (3-10) are also plotted for both sets.

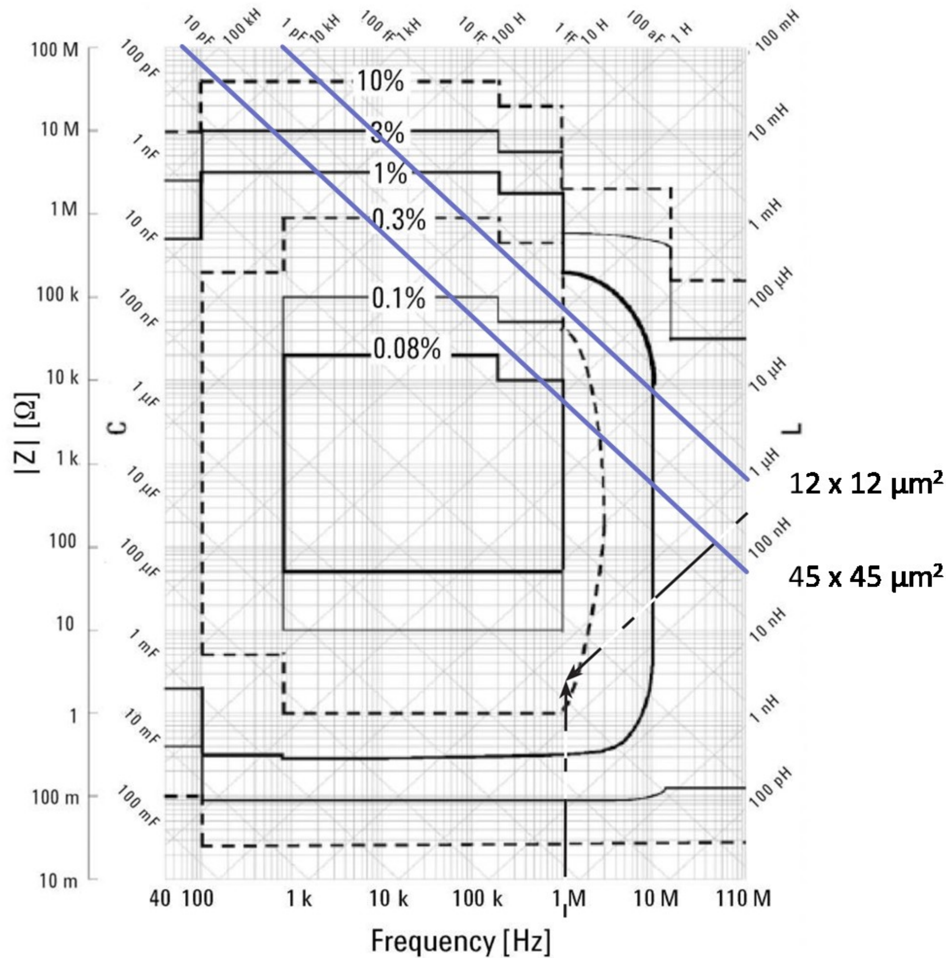

Figure 3-20: Impedance resolution limits to Keysight 4294A Impedance analyzer, as given in the user manual. Lines are drawn which show the approximate impedances for 12×12 μm^2 and 45×45 μm^2 BST parallel plate capacitors [128].

In order to get a more consistent value of Q as device size changes, fits to capacitance were done according to eq. (3-5). The results are plotted in Figure 3-21. From this figure, there is a smaller device-size dependence for both sets of devices. Still, the Qs of devices with an ion-milled mesa appear to have a more pronounced dependence on device size than those with a wet-etched mesa. In this case, it appears that Q for devices with a

wet-etched mesa may stay the same or even increase as device size is reduced, though there are extremely large error bars.

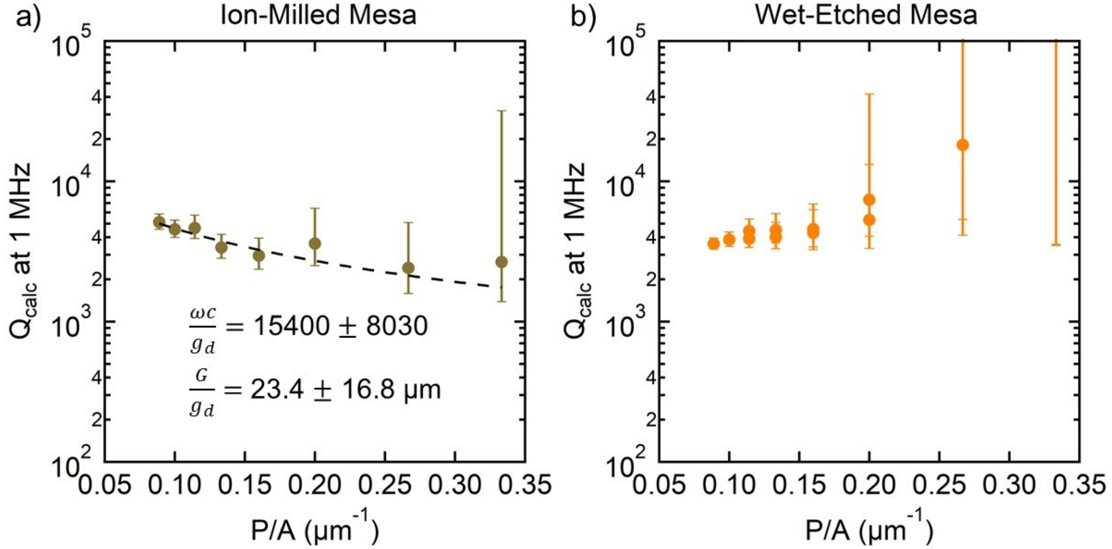

Figure 3-21: Q calculated at 1 MHz using fits to capacitance as a function of frequency as described by eq. (3-4) and (3-5). A fit to eq. (3-10) is plotted for the set with the ion-milled mesa, along with fitted parameters. Error bars are shown according to a 95% confidence interval for the fitted value of n for eq. (3-4).

The difference in capacitance density, c, is shown in Figure 3-22 as a function of P/A. For the sputtered devices discussed in Ref. [127], capacitance density is on the order of 20-24 pF/μm^2, or roughly 1/2 to 2/3 of the value seen here. The increase in capacitance density further emphasizes the improved quality of MBE-grown BST films (and the BST-Pt interfaces), which have higher capacitance density despite more than double the thickness (135 nm vs. 300 nm) and a lower Ba composition (x = 0.5 vs 0.3). The capacitance density is expected to rise slightly for smaller devices, since fringing capacitance from the edges becomes a larger contribution [52]. Fringing capacitance is discussed further in Section 3.5.2.2. In comparison to the previous study of geometry-

dependent effects [127], $\frac{\omega c}{g_{\mathrm{d}}}$ is larger for the devices measured here by almost two orders of magnitude. Since c is only moderately higher, and ω is the same, g_{d} must be much smaller in the devices measured here.

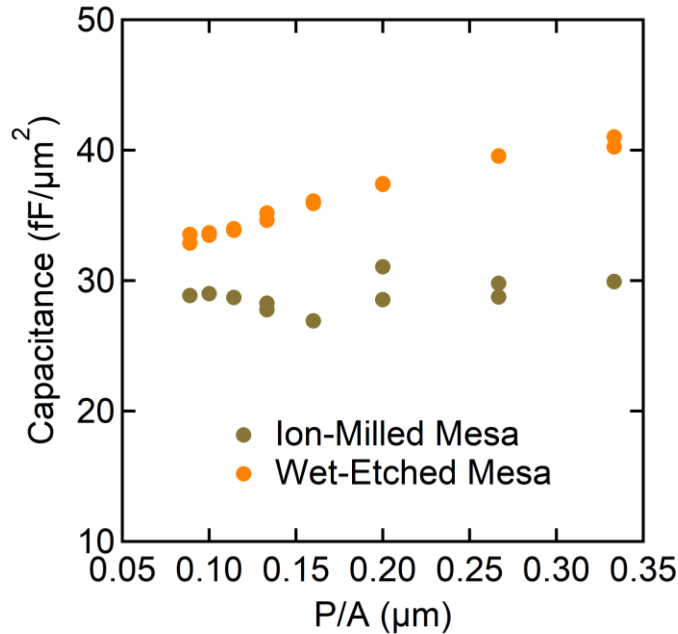

Figure 3-22: Capacitance density (at 1 MHz) as a function of perimeter length to device area for devices with mesas etched by ion mill and wet etch processes.

In Ref. [127], $\frac{G}{g_{\mathrm{d}}}$ ranges from 2-3 μm, which is moderately lower than the ion-milled devices measured here (23 μm, as seen in Figure 3-21). Since g_{d} is much smaller for our devices, the difference in $\frac{G}{g_{\mathrm{d}}}$ of only an order of magnitude suggests that G is lower even for the devices with an ion-milled mesa. The improvement is even more dramatic for the devices with a wet-etched mesa. To summarize, it appears that the device size effects may be less detrimental to device performance for the MBE-grown BST than for sputtered material. For the sputtered material, a 2×2 μm^2 device should have an expected Q peak of less than 38. Using the fits to device size in Figure 3-19a, the dry

etched sample has a predicted Q of 322, while the wet-etched sample could be much higher. This result suggests it is the combination of a less-damaging etch process (wet etch with 1:20 HF:H_2O) along with the high quality of the MBE-grown material that contribute to the higher performance upon miniaturization measured here.

3.5.2.2 Effects of device size on *C*

As device size is reduced, a larger fraction of the total device size is made up of material that is not directly between the top and bottom contacts [13]. Our model for a parallel plate capacitor ignores these edge regions, instead assuming that we have effectively infinite plates as our contacts. If this is the case, all electric field lines should be straight between contacts with no variation. The edges of the device are thus not considered in this model. In fact, there is a buildup of charge at the edges of a parallel plate device, which can lead to higher fields in addition to their non-uniformity [13].

This variation from the ideal parallel plate capacitor can lead to changes from the expected behavior, especially in a high-dielectric-constant material like BST. In the past this was well-modeled by the presence of a non-tunable fringing capacitance, C_f, which is in parallel with the tunable capacitance and is dependent on the device perimeter. This can be thought of as a slight extension of the top and bottom contact areas (plates) of the device to account for the increased charge density at the edges, in which the BST is non-tunable. This has been successfully accounted for by modifying the tunability relation in eq. (1-5):

$$C(V) = \frac{C_{max} - C_f}{2 * \cosh\left(\frac{2}{3} * \sinh^{-1}\left(\frac{2V}{V_2}\right)\right) - 1} + C_f \tag{3-11}$$

After this modification, two variables depend on device size - this fringing capacitance contribution and C_{max}. V_2 should remain the same for all devices made in the same process, since it is related primarily to material and interface quality. Note that changing C_f does not affect the peak capacitance predicted by the model, since at zero field the model collapses to C_{max}. The plots here use a BST film thickness of 300 nm to calculate electric field E from applied bias V. As such, we consider $E_2 = V_2/d$ (where d is the film thickness) instead of V_2, but for the purposes of the fit there is no difference besides units.

Excluding this fringing capacitance term, fits to multiple device sizes are shown in Figure 3-23. These are the same devices described in 3.5.2.1 with the wet-etched mesa. In this fit, C_{max} is set the the peak capacitance measured at each device size. E_2 is fitted to the largest 45 × 45 μm^2 capacitors, where the fringing capacitance term C_f should be negligible, and then this number is used for all devices in the series.

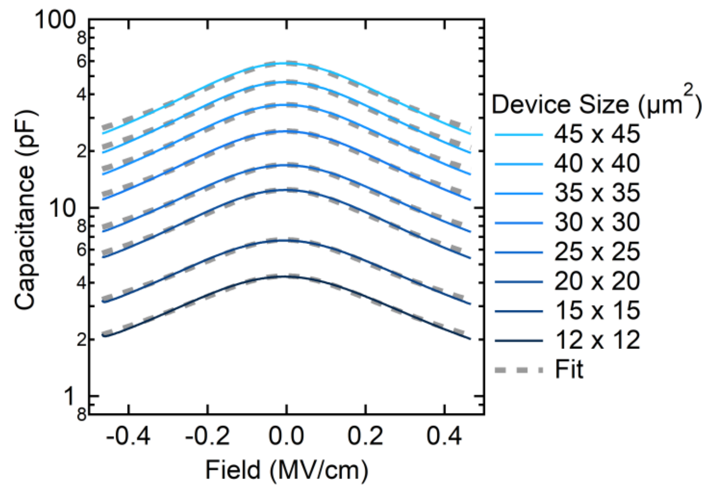

Figure 3-23: Fits (gray dashed lines) to the measured (solid lines) capacitance as a function of applied DC field for different device sizes without including a fringing capacitance. First V_2 (here, 0.400 MV/cm) is fitted to the 45 × 45 μm^2 device, and this value is used for all sizes.

As seen from the fits, the changes in tunability are not accurately captured before the inclusion of C_f. In previous studies, the effects were only significant for device sizes below 12×12 μm² [13]. Including the fringing capacitance term still does not completely describe the behavior seen in the field-tuned capacitance, as shown in Figure 3-24. Fitted values of the fringing capacitance are also shown. As such, the tuning model in (3-11) does not adequately describe this dataset under the given conditions.

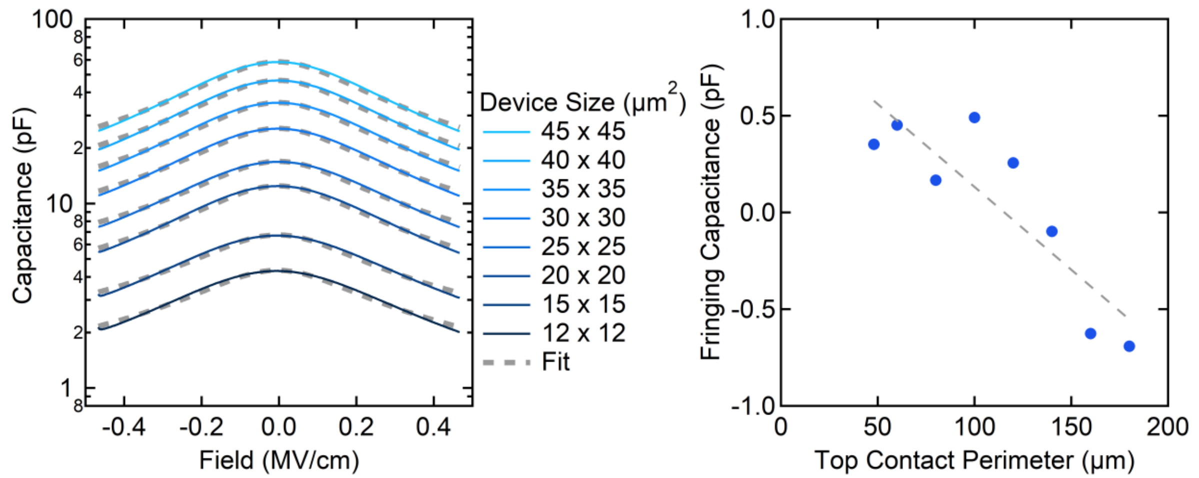

Figure 3-24: Fits to tunable capacitance including a fringing capacitance term according to eq. (3-11) (left). This fit uses the same V_2 (0.400 MV/cm, fitted to the 45 × 45 μm² device) as in Figure 3-23). Fitted fringing capacitance is shown on the right for each device.

Because of the irregularities even with the largest devices, the same fit was performed with V_2 unconstrained (except that it must be the same for all devices regardless of size). This fit is shown in Figure 3-25, along with the extracted fringing capacitance as a function of device area. As seen from the fit, this fit describes the data far better than before. Nevertheless, there are two unusual aspects to the values found for the fringing capacitance. First, all fitted values are negative, and the value increases

in magnitude for larger devices. Second, the negative fringing capacitance also scales linearly with device area, and not with device periphery as observed previously.

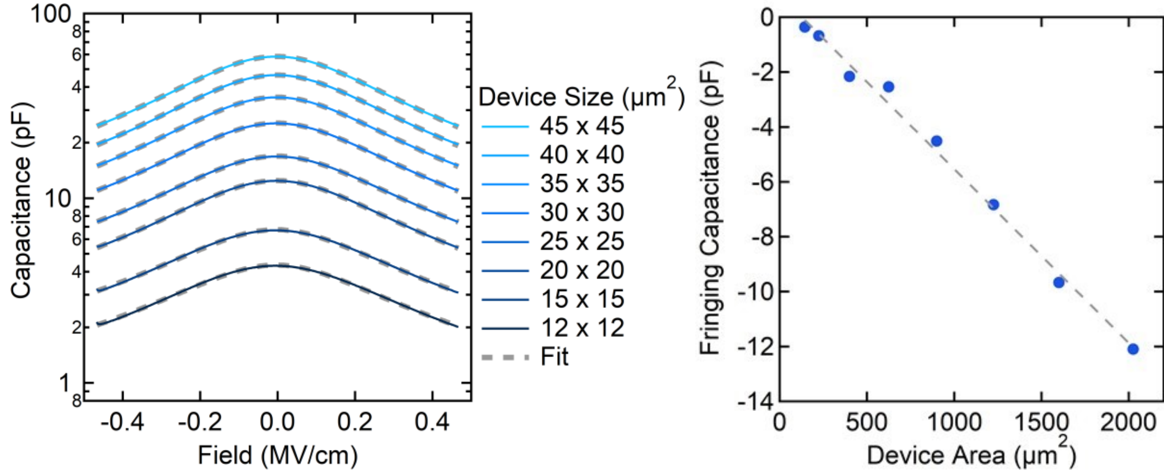

Figure 3-25: Fits to tunable capacitance including a fringing capacitance term according to eq. (3-11) (left). This fit set C_{max} to the peak value for each device but allowed C_f and V_2 to vary (V_2 still remains the same for all devices). Fringing capacitance is shown on the right.

A negative fringing capacitance, while generally non-physical, can be explained by a slight adjustment to the simple model discussed previously. Before, the charge buildup at the device edges was simulated by artificially extending the edges of the top and bottom contacts (e.g. adding a parallel 'fringing' capacitance). The negative values here suggest an artificial shrinking of the effective contact area instead. If fields are higher at the edges of the device than in the center, this could be explained by larger-than-normal tuning at the device edges, leading to a lower effective device area. However, one would expect this effect to scale with device perimeter, not with the area as shown here. This remains an open question that requires further investigation.

3.6 BST on oxide substrates for interdigitated devices

As discussed in Sections 1.2.3.2 and 3.5.2, miniaturization of parallel plate devices leads to an increased influence of the device periphery on ultimate performance. In order to reduce the device capacitance of 300 nm thick BST capacitors to prevent roll-off before the low GHz regime (C ~ 1 pF), device area needs to be shrunk to less than 2x2 μm^2 for a 300 nm film. Because interdigitated device structures (see Section 1.2.1.1) do not require a BST etch near the active region, it provides a good starting point for the high-frequency characterization of the improved material properties afforded by MBE-grown BST.

Another benefit of the interdigitated device structure is the ability to grow BST on a wide variety of substrates, since no back contact is required. As demonstrated in Section 3.1, we have demonstrated a good degree of control over BST film stoichiometry with Ba composition varying from 0% up to 60%. By using oxide substrates with similar crystal structure and lattice constants, BST can even be grown lattice-matched and fully strained. Figure 3-26 shows lattice constants for commercially available substrates, with a comparison to the achievable lattice constants for BST. Based on measures of BST lattice constant as a function of composition [11], [33] $DyScO_3$ is lattice matched to $Ba_{0.46}Sr_{0.64}TiO_3$. Several other substrates are available with lattice matches to higher Ba-composition BST, but due to the trends described in 1.1.1, higher Ba composition is likely to have lower *Q* factors than desired. As shown previously, even $Ba_{0.46}Sr_{0.64}TiO_3$ may have significantly more tunability than needed, so a first test involved the growth of 300 nm $Ba_{0.12}Sr_{0.88}TiO_3$ on $DyScO_3$ (110), which has a moderate tensile strain (0.5%).

Another sample of the same composition was grown on the compressively-mismatched (2.8%) $LaAlO_3$ for comparison.

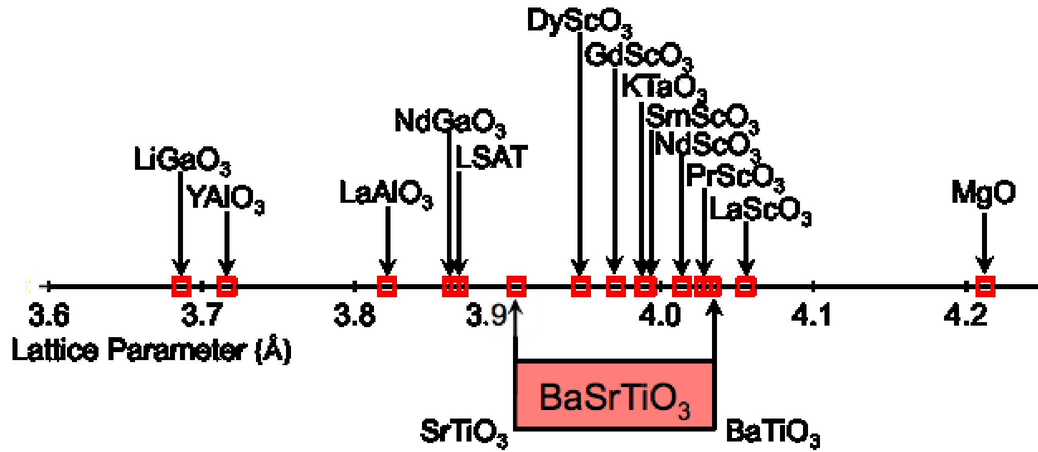

Figure 3-26: Lattice parameters of commercially-available substrates, compared with the range of possible $Ba_xSr_{1-x}TiO_3$ lattice constant. Pseudocubic lattice constants are shown for non-cubic crystal structures (averaging d_{110} and $d_{1\bar{1}0}$).

While post-growth RHEED showed high-quality growth on both substrates, AFM of the surfaces showed problems with the film grown on $DyScO_3$, as shown in Figure 3-27. While the film grown on $LaAlO_3$ is smooth, with visible atomic steps, the film on $DyScO_3$ shows extremely large raised features. These raised features result from the film cracking under the tensile strain, and the areas near the crack itself delaminating from the substrate, as shown in Figure 3-27c. These cracks are also visible in an optical microscope, though they are faint. Low ultimate tensile stress is a known weakness with ceramics, and in this case it appears to be the favorable mechanism to relieve the large mismatch. The AFM of the BST surface grown on $LaAlO_3$ (Figure 3-27) demonstrates the presence of a high density of twin boundaries within the substrate. The atomic steps vary in both orientation and density between the left and the right sides, with a twin

boundary in the middle. These twins are known to occur at relatively high densities in $LaAlO_3$ substrates, and cannot generally be avoided. Nevertheless, film quality is good, and atomically-stepped surfaces can be achieved under the right growth conditions.

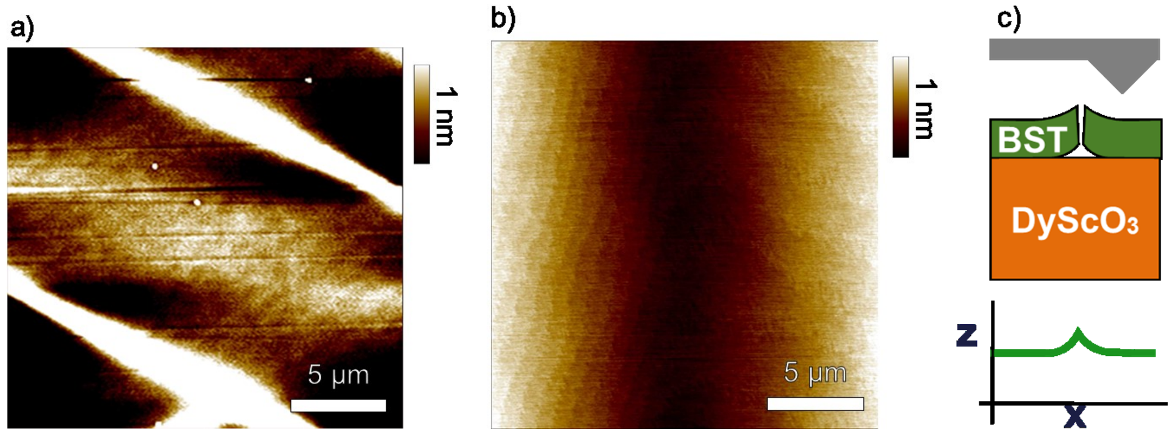

Figure 3-27: Atomic force microscopy images of 300 nm $Ba_{0.12}Sr_{0.88}TiO_3$ grown on oxide substrates a) $DyScO_3$ (110) and b) $LaAlO_3$ (001). (c) demonstrates how film cracking and delamination causes the raised features seen in (a).

While interdigitated devices were fabricated from the BST on $LaAlO_3$ at these low Ba compositions, the tunability was too low to make good devices. Next, BST with x = 0.29 was grown on $LaAlO_3$, and BST with x = 0.46 was grown on $DyScO_3$. Atomic force micrographs of some of these samples are shown in Figure 3-28. As seen in the figure, the surfaces are extremely smooth, and no cracks were observed in the BST film on $DyScO_3$ due to the closer lattice match. While the step sizes are one unit-cell height in both micrographs, there is a contrast change on the steps for the sample grown on $DyScO_3$. This may be related to differences in surface termination, since the height of these features is smaller than the lattice constant of the material.

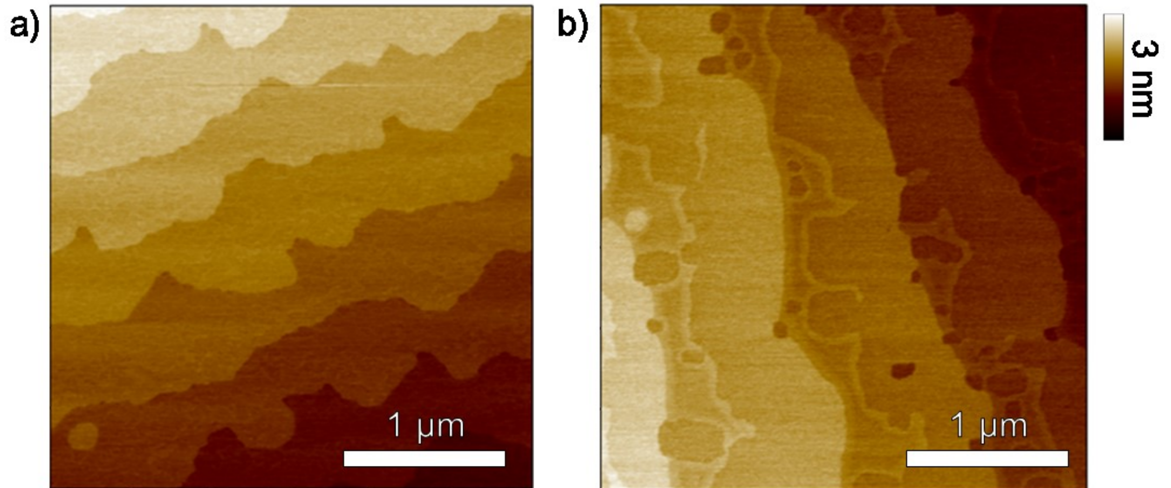

Figure 3-28: Atomic force micrographs of (300 nm thick) BST surfaces grown on a) $LaAlO_3$ (x = 0.29) and b) $DyScO_3$ (110) (x = 0.46).

Off-axis reciprocal space maps for these samples are also shown in Figure 3-29. The sample grown on $LaAlO_3$ is fully relaxed, as seen by the peak positions which lie on the diagonal line which indicates in-plane and out-of-plane spacing are the same. Because $LaAlO_3$ also has a cubic crystal structure, it lies on the diagonal line as well. This contrasts with $DyScO_3$, which is orthorhombic with slightly different pseudocubic lattice spacings in- and out-of-plane. (To get the pseudocubic lattice spacings, ½·d_{110} and ½·d_{001} are used) However, because the in-plane and out-of-plane lattice spacings should be the same for this reflection (½·$d_{1\bar{1}0}$ and 1½·d_{110}, respectively), the $DyScO_3$ 2 4 0 reflection should still appear cubic. The similar lattice constants between BST film and $DyScO_3$ substrate also lead to a fully-strained film, despite being 300 nm thick. This can be seen by the in-plane spacing which is the same for both, but which results in an extension of the BST lattice constant out-of-plane due to the slight tensile mismatch. This leads to a dramatic compression in the BST out-of-plane spacing.

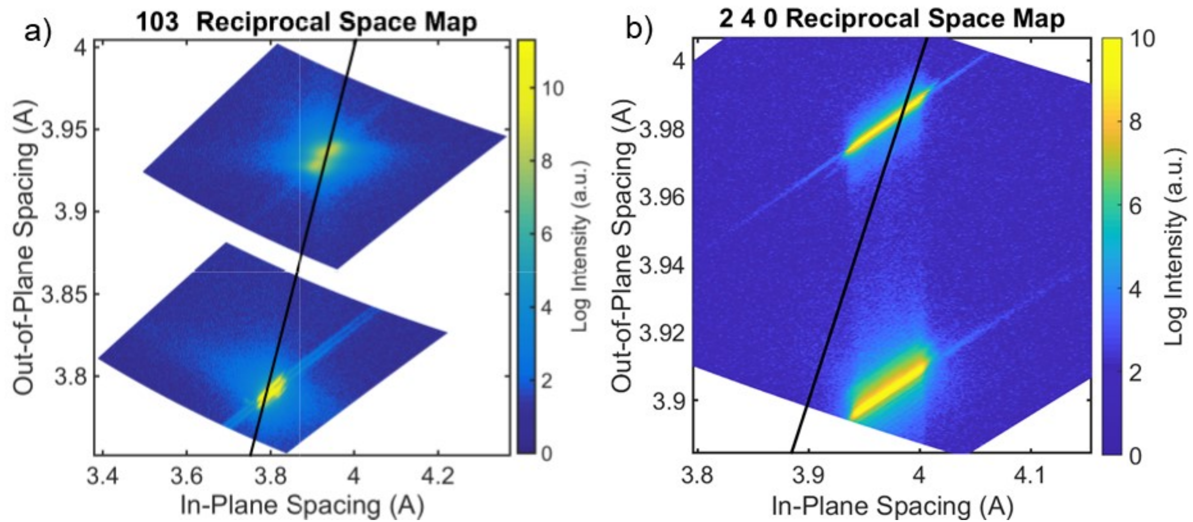

Figure 3-29: Reciprocal space map of a) 300 nm BST (x = 0.29) grown on $LaAlO_3$, demonstrating a fully-relaxed film lattice constant and b) 300 nm BST (x = 0.46) grown on $DyScO_3$ (110). The cubic condition (in-plane spacing = out-of-plane spacing) is indicated with a black line.

While the BST on $LaAlO_3$ showed impressive performance (as will be discussed), large DC leakage was found for the samples on $DyScO_3$, such that high-performance devices could not be fabricated. While Q at zero bias is expected to be lower for these devices, due to higher Ba content, it was simultaneously lower than expected and degraded rapidly under bias. This may have been related to slight titanium excess in the film growth, since this condition has been shown to demonstrate more leakage for our films [22]. It has been shown that slight titanium richness can be achieved even for samples showing the c(4×4) reconstruction in *in-situ* RHEED [112]. While the films grown on $LaAlO_3$ showed better performance under bias, another unexpected problem became apparent. XRD patterns of films on $LaAlO_3$ frequently demonstrated asymmetric peaks for the substrate as well as the film, as demonstrated for a 150 nm

BST film in Figure 3-30a. The surface of the sample is also shown by AFM in Figure 3-30b.

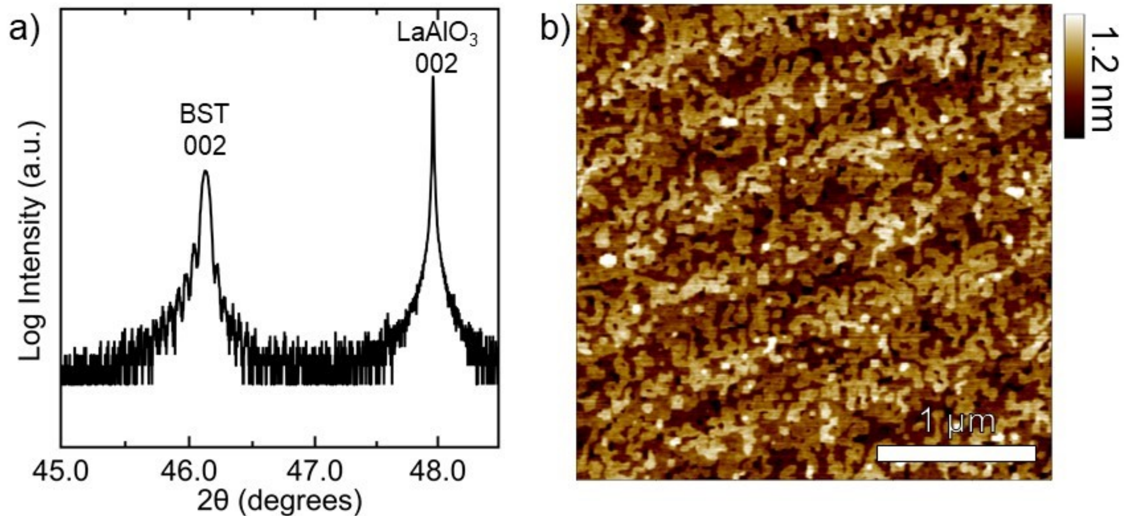

Figure 3-30: X-ray diffraction pattern (a) and atomic force micrograph (b) of 150 nm of BST (x = 0.29) on $LaAlO_3$ (001).

An explanation for this asymmetry calls back to the previous mention that $LaAlO_3$ substrates are highly twinned (Figure 3-27). This gives a number of regions in the substrate where the diffraction planes are slightly misoriented from one another. As such, when there is axial divergence in the x-ray source (Figure 3-31a), there is additional low-angle (or higher spacing) intensity (Figure 3-31b). This is typically only a concern in powder diffraction, which relies upon having crystallites of all orientations. To summarize, the use of a Soller slit should improve the diffraction patterns measured for these films on $LaAlO_3$, and the slight asymmetry should not necessarily be a cause for concern about sample crystal quality.

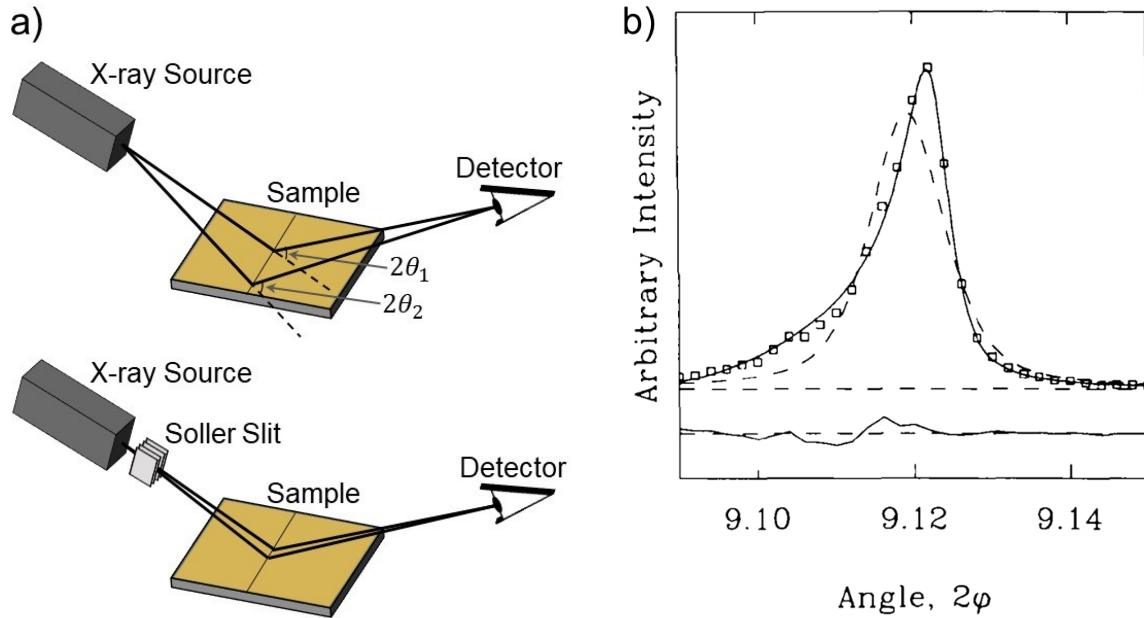

Figure 3-31: A demonstration a) of how a Soller slit used in powder x-ray diffraction reduces axial divergence, and b) how the Soller slit improves the diffraction pattern when multiple crystal orientations are present. In b), data are represented by squares, a symmetric pseudo-Voigt profile by a dashed line, and an asymmetric profile by a solid line. (b) reproduced under open access from [L. W. Finger, D. E. Cox, and A. P. Jephcoat, "A correction for powder diffraction peak asymmetry due to axial divergence," *Journal of Applied Crystallography*, vol. 27, no. 6, pp. 892–900, 1994.]. (Ref. [129])

Using BST samples on $LaAlO_3$ with x = 0.29, (as determined by lattice constants of strained BST calibrations on STO, as well as measured lattice constants on $LaAlO_3$ after sample growth), a number of devices have been fabricated by our collaborator in Electrical Engineering, Cedric Meyers, under the direction of Professor York. Because of the additional complexity in fabricating devices to operate at GHz frequencies, this expertise was needed. Their primarily focused on the fabrication of interdigitated devices with the material described here. Significant effort went into how to fabricate

devices without degrading the material, including etching, patterning top contacts which were spaced significantly from the active area, and passivation. While it was expected that growth of thicker BST films would improve performance of these devices as a result of the fringing fields, these effects were also studied more extensively [36]. This work resulted in the demonstration of devices with record commutation Qs across the L band [35], [37]. Additionally, parallel plate devices fabricated for low-frequency measurements were measured at high frequencies, demonstrating the expectation that the extraordinary Qs measured at low frequency may indeed translate to such high Qs at GHz frequencies [130].

3.7 Conclusions

Previously, it was demonstrated that the performance of $Ba_xSr_{1-x}TiO_3$ tunable capacitors could be dramatically improved by leveraging a hybrid MBE growth process. This work has demonstrated some of the causes of this performance increase by investigating two main factors: film stoichiometry and film-contact interfacial quality. As should be expected, BST film stoichiometry plays a large role in device performance. For devices with proper stoichiometry, device Q at zero bias was maximized. Under bias, however, Q degraded moderately for the stoichiometric and titanium-rich samples. In contrast, samples which had slight A-site excess demonstrated a negligible reduction in Q under bias, which is the opposite of what is observed in literature for sputtered films [125]. We find that the slight rise in Q upon the application of bias, which is ubiquitous in literature, is not intrinsic to BST material, but instead is only

seen in samples with *A*-rich stoichiometries. In fact, for the stoichiometric samples, a slight drop in *Q* is observed upon the initial application of bias. We suspect this may be a result of intrinsic loss via the onset of the quasi-Debye mechanism upon the breaking of centrosymmetry by applying external DC bias.

In addition to stoichiometry, the effects of improving the interface quality between the BST film and top contact was also studied. While improving this interface did not dramatically influence device *Q*s, it had significant effects on total device capacitance through the enhancement of a non-tunable series capacitance at the interface. By reducing the contribution (increasing the capacitance) of this non-tunable interfacial layer, device tunability was also improved. Furthermore, devices could then be biased to higher voltages, since the non-tunable layer appears to have lower breakdown field than the BST film (and by increasing the interfacial capacitance, more of the voltage is shared with the BST film).

In addition to record performance at MHz frequencies, collaborators in Electrical Engineering at UCSB have fabricated interdigitated device structures with our films which have, among other exciting demonstrations, achieved record performance across the L band. Work is currently ongoing to fabricate high-frequency parallel plate capacitor devices with this material as well.

4 Progress in thin-film growth of degenerately-doped $BaSnO_3$

While I have been present at UCSB since MBE growth of $BaSnO_3$ was first attempted here, a great deal of work went into the successful growth of single-phase thin film $BaSnO_3$ prior to my work on the project, as outlined in Section 1.3.1. The continuation of this work achieved room temperature electron mobilities around 170 $cm^2/V{\cdot}s$ at doping densities around 10^{20} cm^{-3}. However, many questions about the growth and opportunities to improve film performance (and consistency) remained. This original work primarily focused on understanding film stoichiometry and its relationship to film morphology and electrical properties. However, due to changing growth rates, both total thickness and carrier density were not consistent for this series, making

conclusions difficult. The first step moving forward was getting consistent thickness and carrier density while varying film 'stoichiometry' through the proxy of flux ratios. In particular, an older series of samples provided a broad survey of $BaSnO_3$ growth which served as the foundation for my work. These samples were grown and measured by Santosh Raghavan and Omor Shoron, and they examine a wide range of parameters including Ba and SnO_x flux, oxygen plasma flow and RF power, substrate temperature, substrate material and surface preparation, doping densities, and total film thickness. While I did not collect that data personally, the analysis of these samples included in this chapter is new. Special care is taken to specify which figures and data come from this older dataset.

4.1 Controlling growth rate

In an effort to reduce the number of variables, the growth time for the majority of samples in the original studies (samples grown by Santosh Raghavan and Omor Shoron) was held constant at 90 minutes. For consistency's sake, the SnO_x flux was held constant, and the Ba flux was changed to alter stoichiometry. This resulted in large variations in growth rate, as seen in Figure 4-1. Here, we see that growth rate varies almost linearly with Ba flux, and there is effectively no trend with SnO_x flux. Growth rate in this case is calculated by dividing the total thickness of the sample (as measured by thickness fringes in XRD) by the total growth time. While this ignores potentially important changes in growth rate during film growth, it should still be an adequate

assumption that growth rate is consistent throughout growth. Variations in growth rate throughout a single growth will be discussed later in Section 4.7.

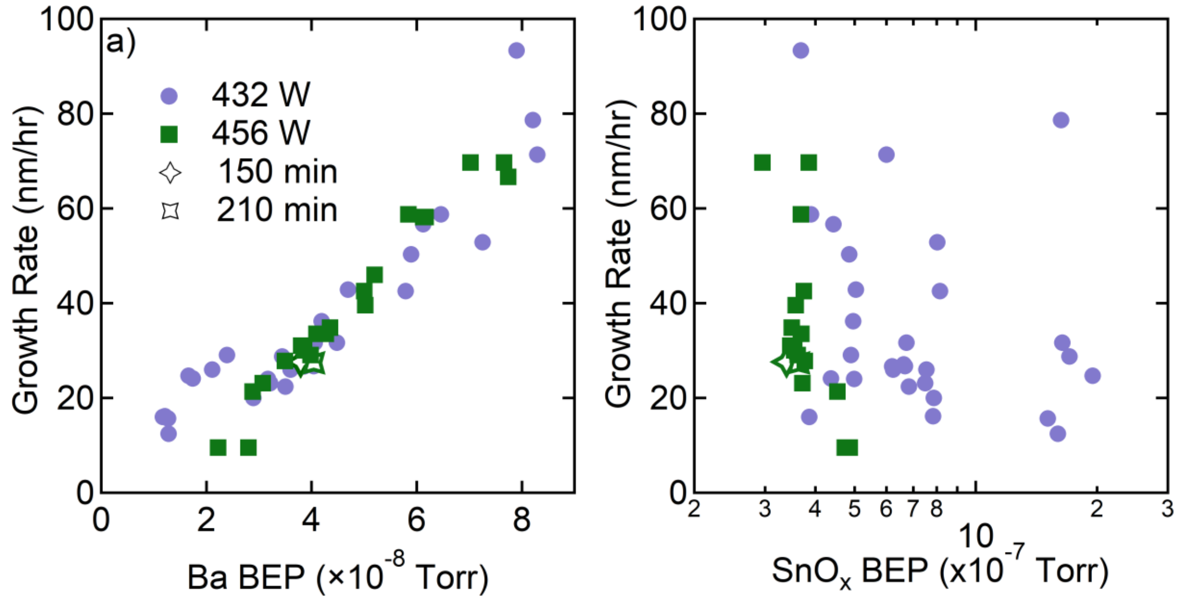

Figure 4-1: $BaSnO_3$ growth rate as a function of a) Ba flux and b) SnO_2 flux for samples grown on $DyScO_3$ with substrate heater power of 432 or 456 W. The growth rate increases linearly with Ba flux, and it does not change systematically with SnO_x flux. While most samples were grown for 90 minutes, samples grown for 150 and 210 minutes are also marked (indicated in the legend). Samples were grown and measured by Santosh Raghavan and Omor Shoron.

Because growth rate is controlled strongly by the Ba flux, we say that $BaSnO_3$ is in a Ba-limited growth regime. This suggests that the SnO_x species is volatile enough to desorb from the growth surface and agrees with other evidence for the existence of a growth window with nominally self-limiting stoichiometry [76]. While the stoichiometry may be somewhat self-limiting, it is important to note that this desorption is not sufficient proof of perfectly self-limiting stoichiometry. In direct contrast with analogous growth systems, such as GaAs (where excess As can desorb and

growth rate is Ga-limited), we have not observed a plateau in the $BaSnO_3$ growth rate with respect to Ba flux. Before the plateau is observed, higher Ba flux first causes mobility to dramatically drop, then the cubic perovskite no longer grows single-phase, as described in Section 4.4.

4.2 Identifying cation stoichiometry by SnO_x/Ba Ratio

In GaAs growth, the linear increase in growth rate with gallium flux eventually plateaus [131]. At this transition, the extra gallium supplied to the surface no longer contributes to growth of GaAs and is incorporated as a separate gallium phase. By increasing arsenic flux, the growth rate at which this plateau occurs can be proportionally raised. We expect the growth rate of $BaSnO_3$ to be analogous to GaAs. Despite investigating a wide range of both Ba and SnO_x fluxes, we have yet to see evidence of such a plateau in $BaSnO_3$ growth rate. Since it is difficult to precisely measure stoichiometry, we estimate it based on maximum electron mobility, in combination with other characterization such as lattice parameter measurements. While many factors besides stoichiometry contribute to mobility (see Section 1.3), the introduction of point defects from non-stoichiometry causes significant scattering. Room temperature mobilities in oxides are typically strongly limited by phonon scattering at room temperature. As discussed in Section 1.3.2, the room temperature scattering rate in $BaSnO_3$ single crystals has nearly equal contributions from electron-phonon scattering and from point defects related to doping. Because the room-temperature phonon scattering in $BaSnO_3$ is comparatively low, even room temperature

mobilities remain sensitive to non-stoichiometry. We concede that the interactions between different scattering mechanisms, such as the point defects from non-stoichiometry and line defects from the relaxation of $BaSnO_3$ under high strain may yield a maximum mobility that may not necessarily be located at perfectly stoichiometric conditions. The similarities and differences between two measures of film quality, electronic and structural, are discussed further in Sections 4.3 and 4.4. Nevertheless, electronic mobility is often used as a metric for finding nominally stoichiometric growth conditions for $BaSnO_3$ [76], [77]. This section specifically focuses on the relationship between source fluxes and film stoichiometry as measured by electron mobility.

For typical solid-source MBE without a growth window (i.e. with molecular flux species having very low vapor pressure near growth temperatures), growth must always be done as close as possible to the transition between which flux species is limiting the growth. Any deviation from 1:1 fluxes should translate directly to non-stoichiometry [99]. However, the drop in $BaSnO_3$ mobility when even remotely approaching 1:1 relative flux ratio, along with the linear increase in growth rate with Ba flux (without roughening the surface), provides further evidence [76] of an adsorption-limited growth mode. This can lead to the opening of a growth window, where stoichiometry is self-limiting, like with GaAs [98] or $SrTiO_3$ [100] grown by HMBE. As will be discussed below, this does not appear to be the case for $BaSnO_3$.

In moving forward and getting more consistent growths, it is constructive to find a descriptor for what gives stoichiometric growth. For $SrTiO_3$, we use TTIP/Sr flux ratio

to describe where the growth window occurs. This is a useful metric despite being more qualitatively useful than quantitatively. We can also use it in the context of changing growth parameters to better explain the growth. For instance, increasing substrate temperature leads to an increase in the ability of TTIP and its biproducts to desorb if there is Ti excess. This leads to an opening of the growth window that allows stoichiometric growths at higher TTIP/Sr flux ratios.

For $BaSnO_3$, the natural first guess for a way to directly influence the stoichiometry is SnO_x/Ba flux ratio. However, this leads to some inconsistencies when considering growths over a wide SnO_x flux range. In Figure 4-2(a), the plot of mobility as a function of SnO_x/Ba flux appears to show two regions of high mobility growths – with one peak at a ratio of 10 and another at 45. When plotting the same data as a function of Ba flux (Figure 4-2(b)), these 'separate' peaks overlap much more closely. This is surprising in light of the change in SnO_x BEP by nearly an order of magnitude, from around 5×10^{-7} at the lower temperature (T_{SnO2} = 1070 °C) to 2.5×10^{-6} at higher temperature (T_{SnO2} = 1250 °C). While Ba flux alone is not sufficient to identify the stoichiometry conditions for growth, it is a better descriptor than SnO_x/Ba flux ratio under the set of conditions used in these growths.

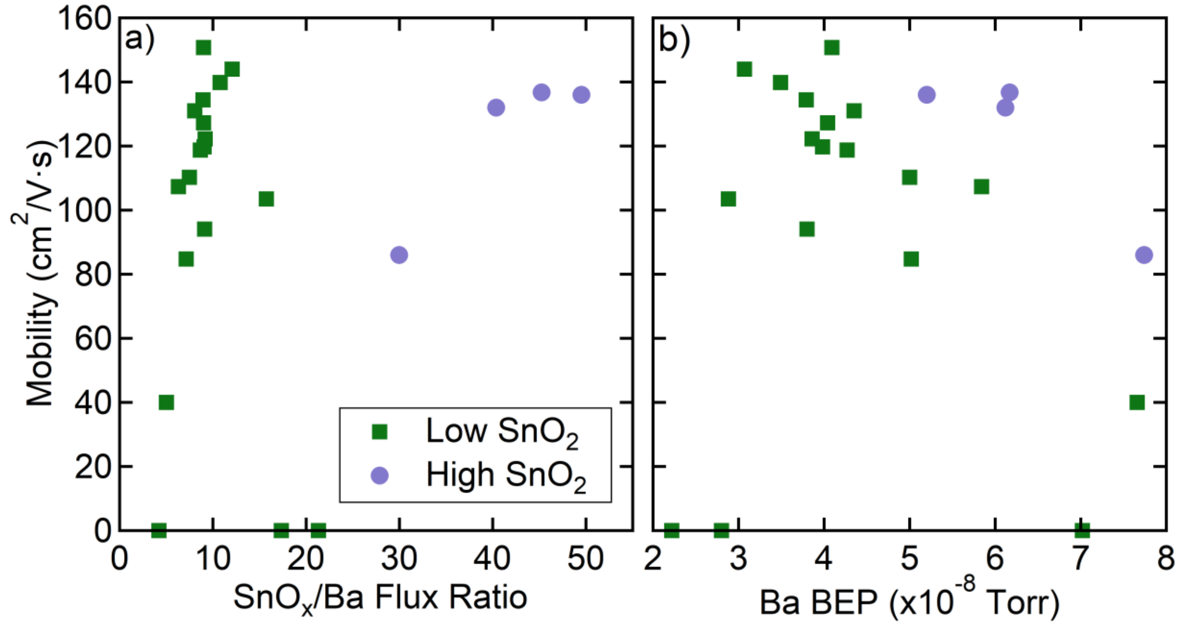

Figure 4-2: Electron mobility of $BaSnO_3$ on $DyScO_3$ (001) as a function of a) SnO_x/Ba flux ratio and b) Ba flux with a substrate output power of 456 W. Note that SnO_x flux is not held constant for these growths. Selected samples grown with higher SnO_x flux are highlighted in both (High ~ 2.5×10^{-6}, Low ~ 5×10^{-7}). Samples were grown and measured by Santosh Raghavan and Omor Shoron.

For the samples in Figure 4-2(b) grown under higher SnO_x flux (in blue), the mobility is moderately higher than others at the same Ba flux, but the rise is not accurately described by the change in SnO_x flux alone. This is could be due to the complex temperature dependence of the compounds comprising the SnO_x flux (Figure 2-4), suggesting that raising the absolute SnO_x flux might only provide a small increase in the partial pressure of the important compound(s) for the $BaSnO_3$ perovskite growth. Alternatively, the higher vapor pressure may simply reduce the desorption rate of SnO such that it is more available to react, thereby increasing the incorporation. The near-independence of film stoichiometry on SnO_x flux is likely also related to the strongly

Ba-limited growth rate. For growths done under similar SnO_x fluxes, SnO_x/Ba flux ratio should serve as a rough indirect measure of stoichiometry, as in this case it is effectively the same as Ba flux. Under a wide range of SnO_x fluxes, clearly SnO_x/Ba flux ratio does not give a complete measure of stoichiometry.

4.3 Separating effects of thickness and stoichiometry

While the growth series discussed up to this point investigates a significant number of variables in the growth, many are correlated and require another study to properly separate the effects. The most problematic coupling is Ba flux with film thickness, such that films which are more *A*-rich are also thicker. Because of increased scattering at the $BaSnO_3$/substrate interface, the thinner films will also tend to have lower mobility. This can be seen in Figure 4-3, demonstrating that none of the measured films with thicknesses below 25 nm were conducting. This finding is also consistent with all other samples we have grown on $DyScO_3$, $GdScO_3$, $SrTiO_3$, or $PrScO_3$. As a result of the changing thickness with changing stoichiometry, it is impossible to separate the effects of both on depletion or mobility.

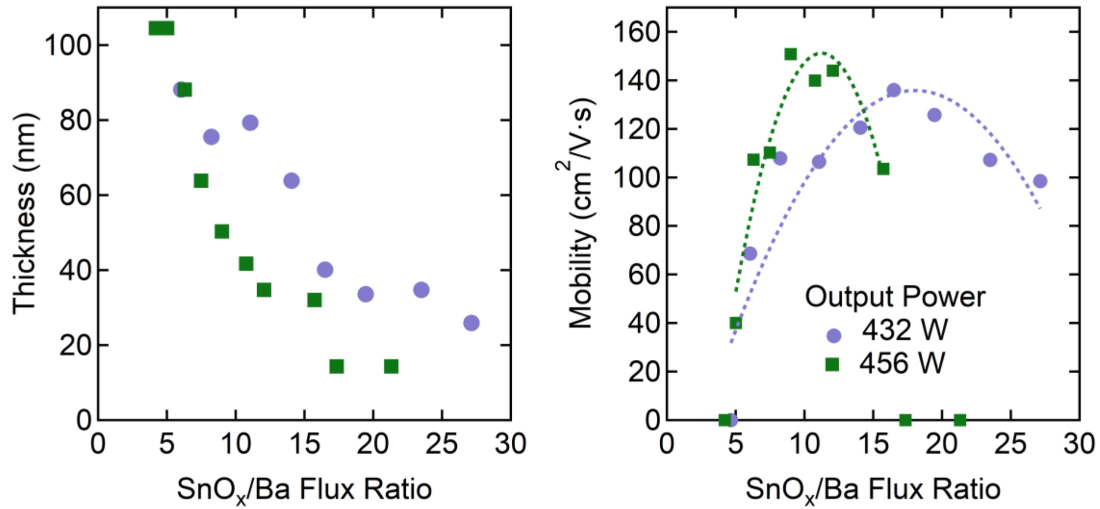

Figure 4-3: Sample thickness and electron mobility as a function of flux ratio for $BaSnO_3$ samples grown on $DyScO_3$ (001) by Santosh Raghavan and Omor Shoron.

To better understand how stoichiometry affects mobility and carrier compensation, I grew another series, this time at a consistent thickness of around 70 nm (approximately 47 nm La-doped $BaSnO_3$ on 23 nm UID $BaSnO_3$) and at a consistent La doping of around 4×10^{19} cm^{-3}. These samples were grown at the same SnO_x cell temperature/flux in order to avoid confounding the results with changing composition of the flux (Figure 2-4). As such, SnO_x/Ba flux ratio in this case is adequate to indirectly denote stoichiometry. Figure 4-4 shows the mobility as a function of the stoichiometry with a SnO_x beam-equivalent pressure (BEP) of approximately 6×10^{-7} at a SnO_2 cell temperature of 1090 °C. The substrate temperature was set by fixed output power to approximately 456 W (38% of max 1200 W), giving a pyrometer reading between 594-600 °C. The pyrometer reading was lower than normal for this series because the pyrometer viewport was coated with material. (The high pressures from the oxygen

plasma and SnO_2 cell during growth lead to deposition onto the viewport despite it not facing any cells)

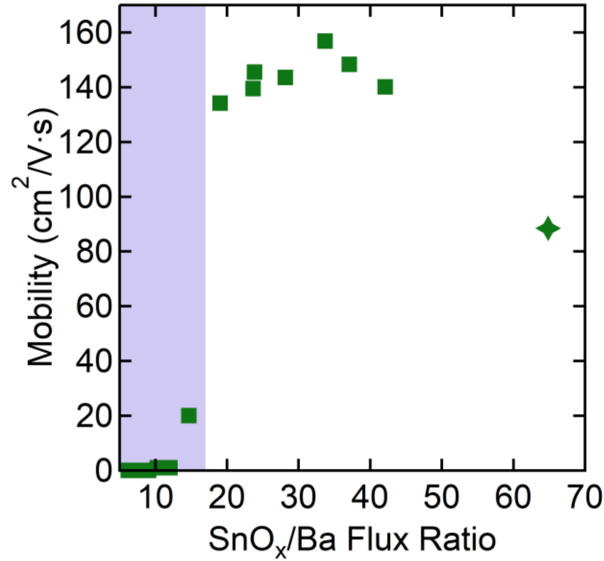

Figure 4-4: Mobility for the $BaSnO_3$ series grown attempting to keep thickness and doping constant. Ba-rich conditions are indicated by the blue shading. The sample denoted with a star had a lower thickness (see Figure 4-5), explaining a portion of the reduction in mobility.

For this series, there is a maximum in mobility of 157 cm^2/V·s at a SnO_x/Ba flux ratio of 33, which is a much higher ratio than any of the series grown prior. This is partly be explained by increasing the growth time for high-ratio samples such that the total thickness remains above 25 nm. As before, there is a drop-off in mobility for the highest SnO_x/Ba ratios, but the drop-off is much less pronounced in this series. For the sample grown at a ratio near 65, the Ba temperature was set incorrectly, giving a lower Ba flux than intended for the growth time used. As a result, this sample had a thickness of only 32 nm, as shown in Figure 4-5. It is likely primarily due to this thickness drop that this sample has lower sheet carrier density and mobility than the rest of the series. (Note

that the doping was set to give constant 2D carrier density, so we should expect to see a higher 3D density since the carriers are spread over less thickness). Regardless, there is strong evidence that growing samples under more Sn-rich conditions degrades the mobility significantly less than Ba-rich conditions.

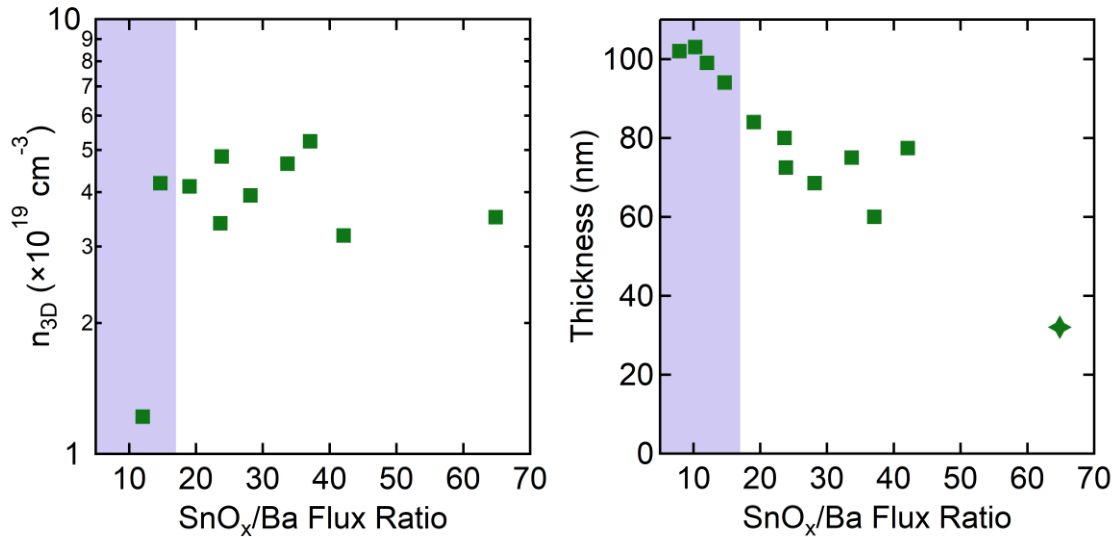

Figure 4-5: Carrier density and total thickness for the $BaSnO_3$ series grown on at relatively consistent thickness and doping (grown on $DyScO_3$ (001)). The Ba-rich condition with low mobility (see Figure 4-4) is highlighted at the right in blue.

A much more dramatic change happens to the transport under Ba-rich conditions. As seen from Figure 4-4, the mobility diminishes slowly below a ratio of 33, then drops dramatically below a ratio of 17 (shaded in blue). However, Figure 4-5 indicates that this drop in mobility happens before a significant change in carrier concentration occurs. As such, these scattering centers are either caused by fixed-charge defects or neutral impurities, since there is no increase in depletion. Multiple theoretical works suggest that under Ba-rich conditions, La may begin incorporating onto the Sn site rather than just the Ba site, effectively negating the doping and interfering with conduction that is

heavily dependent upon the Sn 5s states [71], [132]. This unintentional compensation is further exacerbated under Sn-deficient conditions, which may be the case based on the difficulties observed with Sn incorporation.

4.4 Structural Quality

Another important measure of stoichiometry is x-ray diffraction. Since it is only sensitive to relatively large volumes, it will not necessarily detect defects from only slight non-stoichiometry. For $SrTiO_3$, it can measure stoichiometry quite accurately due to a lattice expansion stemming from the point defects that form when it grows non-stoichiometric [133]. No such lattice expansion has been reported for $BaSnO_3$. Instead, wide-angle scans demonstrate additional phases that begin forming when growth conditions are far from the fluxes yielding optimized mobility. Figure 4-6 shows XRD patterns for $BaSnO_3$ that is roughly stoichiometric, Ba rich, and Sn rich.

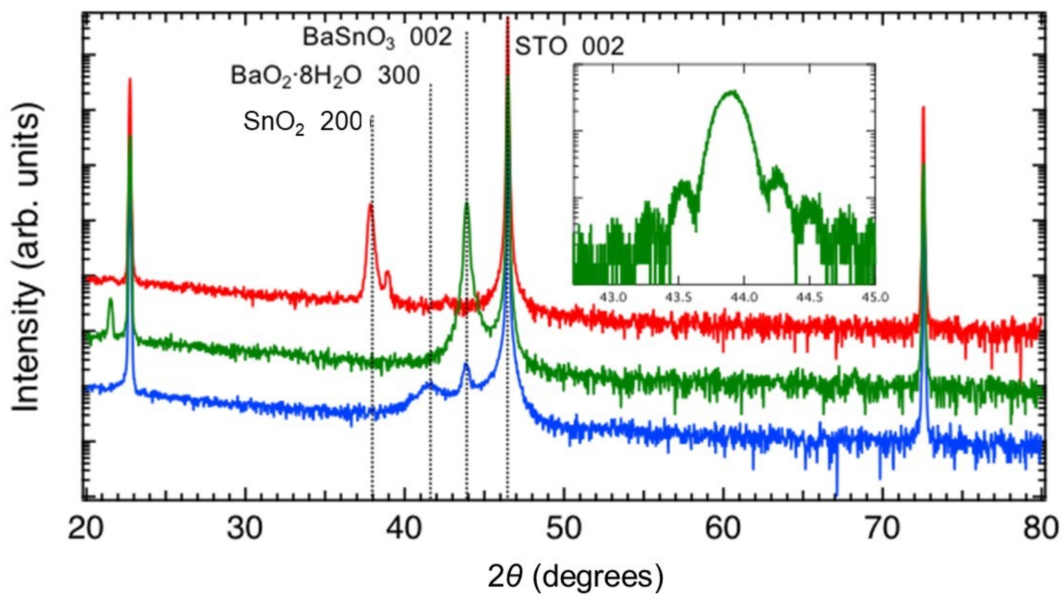

Figure 4-6: X-ray diffraction of Ba-rich (blue), stoichiometric (green), and Sn-rich (red) $BaSnO_3$ on $SrTiO_3$. Samples grown and measured by Santosh Raghavan and Timo Schumann.

As seen from the XRD, the stoichiometric $BaSnO_3$ has a strong 002 reflection with multiple Laue oscillations stemming from the smoothness of the interfaces. There is no evidence of extra peaks that would indicate significant formation of extra phases. In contrast, additional peaks occur in the samples with both Ba-excess and Sn-excess. To match peak positions to indexes, multiple compounds were considered. On the Sn-rich side, SnO_2 and SnO were considered. SnO_2 has the rutile crystal structure ($P4_2/mnm$), which is tetragonal with a = 4.74 Å and c = 3.18 Å [134]. SnO is also tetragonal, but with the litharge crystal structure ($P4/nmm$) with a = 3.84 Å and c = 4.83 Å. While a good portion of the SnO appears to evaporate off from the surface based on its relatively high vapor pressure, other reactions may also be responsible for some of the observed desorption. It is well-known that SnO is metastable and dissociates into SnO_2 and Sn through a process including an intermediate suboxide [108]. However, the composition

and structure is widely debated, with similar numbers of papers suggesting Sn_2O_3 [106], [108] or Sn_3O_4 [107], [108]. Other MBE-grown $BaSnO_3$ has reported additional peaks in Sn-rich conditions indicative of Sn_2O_3 [77], but this is concerning given the relative instability of this compound. A brief description of these compounds is given here for completeness.

Both suboxides have reported triclinic unit cells, though due to difficulties keeping them stable and the non-equilibrium process that forms them, there is chance for variation from the measured parameters. For Sn_2O_3 and Sn_3O_4, lattice parameters are reported in Ref. [106]. Theoretical papers have predicted structures of the suboxides as well, suggesting tetragonal $P2_1/c$ [134]. Diffraction patterns for both suggested suboxides are highly comparable [135].

In Figure 4-6, we see a peak at $2\theta = 38.0°$, which could come from SnO_2 (200). The smaller peak at $2\theta = 39.0°$ could come from SnO_2 (111). Under Ba-rich conditions, BaO and BaO_2 were considered. BaO is a cubic crystal with the rock salt structure and a lattice constant of 5.536 Å at 298 K [136]. BaO_2 is a tetragonal crystal ($I4/mmm$) with a = 3.806 Å and c = 6.822 Å at 298 K [137]. Neither of these structures properly predict the extra peak that appears at $2\theta = 41.6°$. However, BaO_2 is known to absorb a significant amount of water, such that a significant change in the crystal structure occurs. $BaO_2 \cdot 8\,H_2O$ is also a tetragonal crystal ($P4/mmc$) with a = 6.51 Å and c = 11.50 Å [138]. This structure has a (300) peak at $2\theta = 41.6°$. While there is not sufficient water inside the growth chamber to hydrate this BaO_2 phase, exposure to air upon removal from the growth chamber supplies enough water from the air. While the XRD peak position

points to (300) BaO_2, there are several inconsistencies. For one, if the (300) peak is present, one might also expect to see other order peaks from this structure, such as (100) or (200). However, the absence of these peaks is less concerning than the known decomposition of BaO_2 into BaO and O_2 at elevated temperature. In oxygen environment, this happens rapidly above 800 °C, with decomposition starting even below 700 °C [137]. As such, the BaO_2 should not survive the high-temperature rapid thermal anneal (RTA) at 900 °C under 1 L/s oxygen flow for 10 minutes. Indeed, pre- and post-RTA $BaSnO_3$ samples similar to these have shown a strong reduction in peak intensity or disappearance of the BaO_2 peak.

Note that there is insufficient evidence to differentiate between Ba rich/Sn deficient or Ba deficient/Sn rich conditions. While a seemingly minor distinction, the differences manifest in the formation of different defects, which can influence the carrier compensation and scattering. There are several theoretical works which predict how these distinctions affect the defect formation, and therefore defect compensation, under various differences in chemical potentials [71], [132].

To compare with these results, Figure 4-7 shows wide-angle XRD of some of the samples in this series with similar thickness and doping. Conducting samples with mobilities above 30 $cm^2/V{\cdot}s$ are shown in green. Unlike in the previous series, all samples with decent mobility have extra peaks stemming from SnO_2 (110) and (001). Previously, the extra peak in the Sn-rich growth was from SnO_2 (200), as seen in Figure 4-6. In this series, there is no extra peak arising from Ba-containing defect phases, despite the poor transport properties seen for the Ba-rich samples. It also appears there

is an artifact peak at 2θ = 34.1°, since despite having relatively large peak intensity in some of the scans, the peak is always vanishingly narrow. There are also no defect phases considered with peaks in this position.

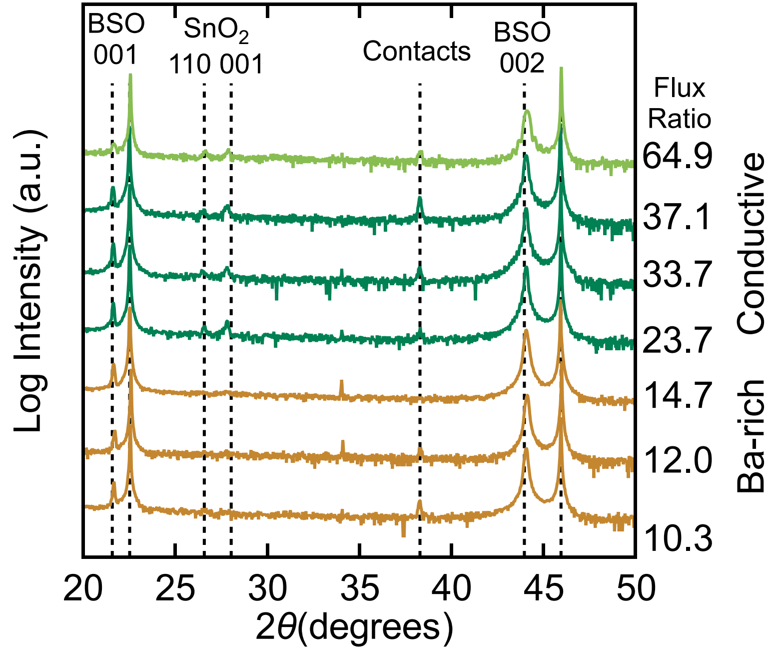

Figure 4-7: Wide-angle XRD scans of $BaSnO_3$ grown with near-constant thickness and doping. Samples within the growth window, as defined by mobility (see Figure 4-4), are shown in green. Unlabeled peaks are from the $DyScO_3$ substrate 002 and 004 reflections.

4.4.1 Using rocking curves to measure structural quality

Another metric that is sensitive to non-stoichiometry, XRD rocking curves [77], suggests that crystal quality indeed changes in both Ba- and Sn-rich conditions. Figure 4-8 shows rocking curves (ω-scans) around the $BaSnO_3$ 002 reflection for several samples in this series. The breadth of these scans, as measured by the peak width, is a direct indication of crystal quality. At intensities closer to the peak's maximum (for example, at half maximum), the width of the curves gives a measure of lateral

coherence, which can be affected by structural imperfections such as mosaicity [139]. At lower intensities (1/10th or 1/20th of max), the peak width is more strongly affected by diffuse scattering from point defects. Thus, for measuring non-stoichiometry based on the prevalence of point defects, we are more concerned with the width at lower intensities.

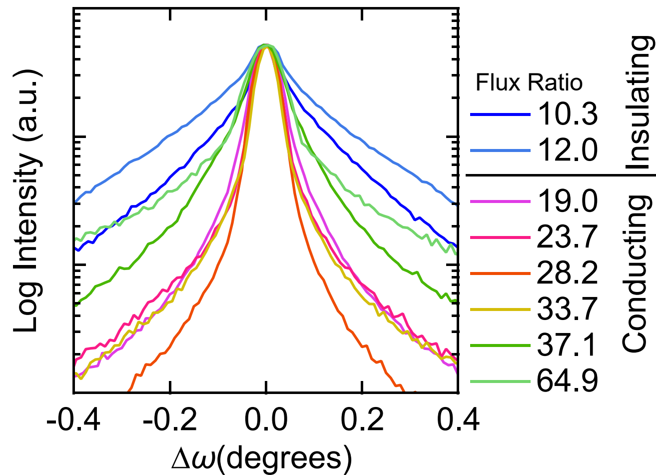

Figure 4-8: Rocking curve of $BaSnO_3$ (002) peaks for the growth series with thickness and doping held constant. Intensities shifted to have same peak intensity to facilitate comparison.

As seen from these rocking curves, the peaks do not dramatically broaden until below half of the maximum. This is indicative of comparable lateral coherence within the sample series, but dramatically different diffuse scattering. To more clearly illustrate the differences within the series, the curve width at 1/20th of max ($\tau_{1/20}$) is plotted along with sample mobilities in Figure 4-8. As expected, there is a negative correlation between $\tau_{1/20}$ and thin film mobilities. Note also that growing under "Ba-rich" conditions yields a sharp drop in mobility, while Sn-rich" conditions have less of an impact, despite significant broadening in $\tau_{1/20}$ for both. Interestingly, the sample with the lowest $\tau_{1/20}$ (SnO_x/Ba = 28.2) does not have the highest mobility (SnO_x/Ba = 33.7),

with rocking curve width being maximized at slightly lower flux ratio than mobility. We note again that although discussing flux ratios here, the SnO_x flux was held constant as to avoid the inconsistencies seen in Section 4.2. As such, this flux ratio can also be viewed as 1/Ba multiplied by a constant.

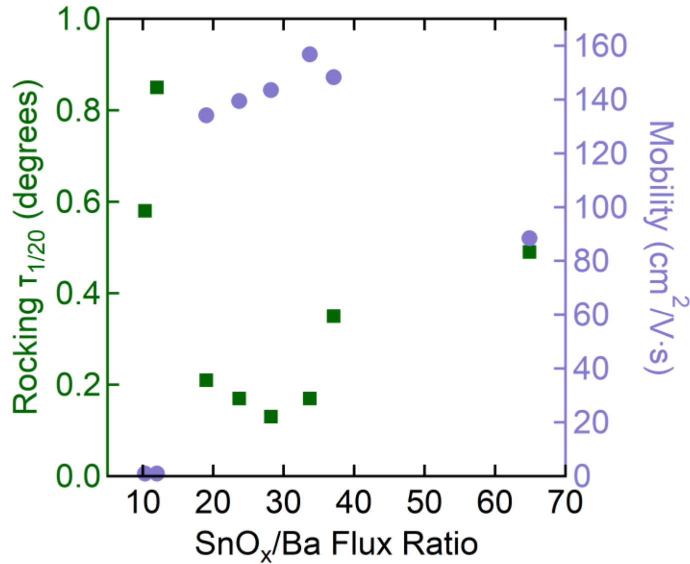

Figure 4-9: Plot showing the rocking curve width at 1/20th of the maximum for the rocking curves shown in Figure 4-8.

4.4.2 Deviation in lattice constant from bulk

Though difficult to see in the 2θ-ω scans in Figure 4-7, there is a slight shift in the $BaSnO_3$ (002) peak from the bulk position indicated by the dotted line. Lattice constants from high-resolution XRD are depicted in Figure 4-10. While there is relatively little scatter, even for the non-stoichiometric growths, the measured value is far from the bulk value of 4.116 Å. This has been observed in other works [77], [105] as well as our own. In some cases, we have observed consistently higher mobilities in growth series that have lattice constants far from the bulk value. While the other works

observe lattice constants higher than expected, we typically observe lower lattice constants, which would not be explained by residual in-plane strain. Figure 4-11 summarizes three growth series grown at different substrate temperatures, depicting a lower-than-bulk lattice constant for samples grown below 840 °C. Notice, however, that mobilities are highest for the series grown at 820 °C. For the series shown in Figure 4-10, the substrate temperature should be very similar to the series grown at 840 °C. However, there is clearly a difference in the growth, as the previous series had lower mobilities, a lattice constant closer to that of bulk, and no evidence of SnO_2 (110) or (002) peaks in XRD.

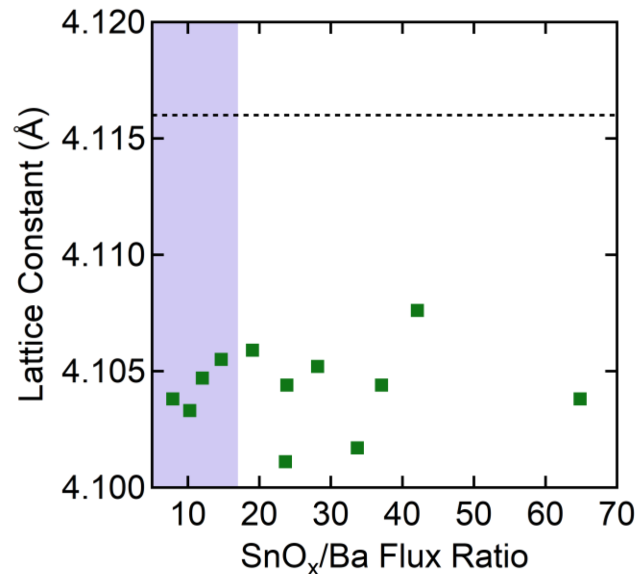

Figure 4-10: Lattice constant as a function of flux ratio for the growth series holding thickness and doping constant. The Ba-rich condition (determined from mobility) is shown in blue. The bulk value of 4.116 Å is indicated with the dashed line.

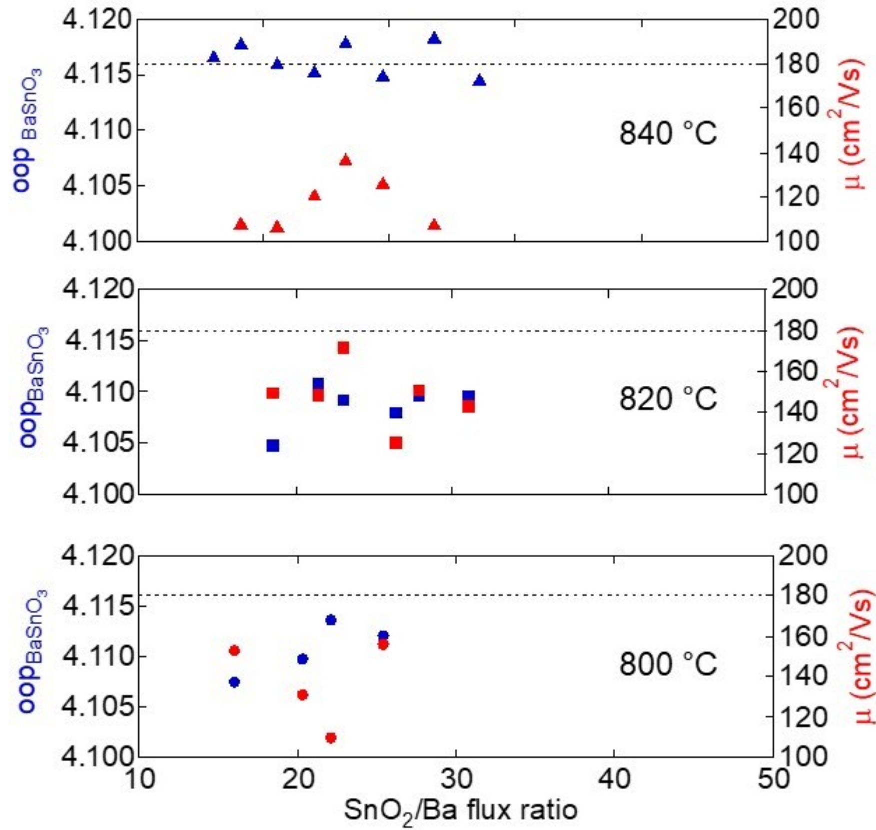

Figure 4-11: Out-of-plane lattice constant as measured by XRD and mobility as a function of flux ratio for various substrate temperatures. Samples grown and measured by Santosh Raghavan, Timo Schumann, and Omor Shoron.

4.5 Changing doped thickness with constant total thickness

As discussed in Section 4.3, it is non-trivial to grow thin $BaSnO_3$ with high mobility. However, for the fabrication of transistors, a thinner channel is important to optimize gating by keeping charges closer to the gate (target $BaSnO_3$ characteristics and the reasons for those targets are discussed previously in Section 1.3.5). Ideally, the channel would be very thin δ-doped $BaSnO_3$ with carrier density around mid-10^{13} cm^{-2}. To understand what causes the mobility of samples thinner than 25 nm (with

approximately 17 nm La-doped) to plummet, we look at changing the doped thickness at a constant total thickness, as shown in Figure 4-12. For these samples, a total of 50-60 nm $BaSnO_3$ was grown, and the proportion of the film that is La-doped is varied. In order to exclude effects from charges screening defects, the 3D dopant concentration is fixed for this series to approximately 3×10^{19} cm^{-2} within the doped portion (based on doping densities from previous growths which were 2/3 doped and 1/3 unintentionally doped). As such, the apparent 2D carrier density should change with the proportion of the film that is doped. In this series, samples were grown with doped proportions of 2/3, 1/3, 1/6, and 1/12 (by growth time).

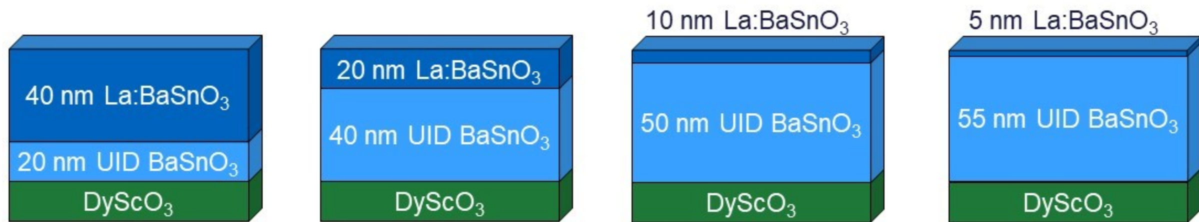

Figure 4-12: Sample structures for investigating potential causes of reduced mobility for thin samples.

Figure 4-13 shows that both 2D carrier density and mobility for each sample decrease as the proportion of the film that is doped decreases. While 2D carrier density is expected to drop for lower doped thickness, it does not change as much as expected. This line is predicted based on the relationship between La temperature and carrier concentration for previous growths with the top 2/3 of the film doped. If carrier density is based directly on La concentration, the 2D doping density should linearly increase with a slope similar to that of the dashed green line, which crosses through the origin. Instead, we see dramatically higher carrier concentrations than expected at low doped

thicknesses. One potential explanation could be that carrier activation is dependent upon the dopant atom's location in the film.

A previous study of our films indicated at least 90% dopant activation at a sample thickness of only 25 nm, and at much higher doping densities of 1.6×10^{20} cm^{-3} [68]. There is evidence of increased depletion for thinner samples, which is likely related to either the substrate-film interface or the surface. If the surface were the significant source of depletion, we would expect lower carrier density than the dashed line predicts for the samples with less doped thickness. This study suggests it is more likely a result of the substrate-film interface, since the samples with more depletion are the same ones with doping that extends much closer to that interface. However, this does not adequately explain the huge amount of depletion that would be required for the trend seen here. For the 25 nm doped sample with 1.6×10^{20} cm^{-3} doping, the worst-case scenario of 10% non-activated carriers gives a maximum depletion of 4.4×10^{13} cm^{-2}. If we extrapolate the expected carrier density from the sample with 8.3% of the thickness doped, this gives an expected carrier density of 5.8×10^{14} cm^{-2} at 66% doped. This requires a depletion over an order of magnitude higher than seen previously, of 4.7×10^{14} cm^{-2}. This requires over 80% of the carriers to be trapped or non-activated, which is unprecedented. Instead, it seems likely that there is another source of mobile carriers in addition to the La doping. The source of these carriers is unknown, especially since oxygen vacancies should be populated during the 900 °C rapid thermal anneal in oxygen for 10 minutes that is conducted after growth. Previously, our unintentionally-doped (UID) $BaSnO_3$ films were found to be insulating after this oxygen anneal.

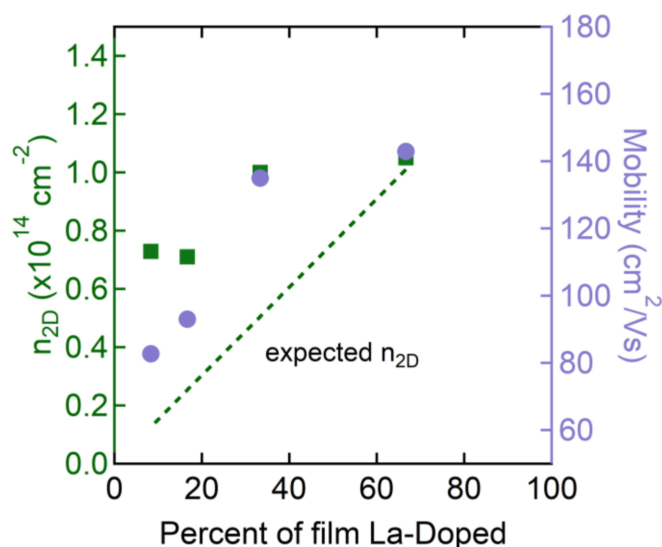

Figure 4-13: Variation of mobility and 2D carrier density based upon how much of the 60 nm $BaSnO_3$ film is doped. Doped film percentage based on growth times for UID and doped layers. The dashed line indicates the expected n_{2D} based on La content.

While the trend in carrier density is difficult to explain, the change in mobility with doped thickness appears more reasonable. Carriers should spread to the undoped portions, since there is no barrier, and the total thickness is relatively low. As 3D carrier density drops moderately with doped thickness, mobility also drops. This is to be expected as having more carriers allows screening of other carriers from scattering sites. Other work on thin films has seen that mobility drops quickly below carrier densities around 2×10^{19} cm^{-3} [76] from around 160 cm^2/V·s to 120 cm^2/V·s at 1×10^{19} cm^{-3}. In this study, the carrier density (calculated as spread evenly through the $BaSnO_3$ film) increases from 1.4×10^{19} cm^{-3} to 2.1×10^{19} cm^{-3} as doped thickness increases. The drop in mobility seen here is more dramatic than the mentioned study, but not unprecedented.

4.6 Strain compensation in $BaSnO_3$ on $DyScO_3$

As discussed previously in Section 1.3.1, substrates with less than 2% mismatch to $BaSnO_3$ are not commercially available. This necessitates a significant strain compensation in thin films, as has been studied previously on $SrTiO_3$ (-5.1%) and $PrScO_3$ (-2.3-2.7% based on substrate orientation). $DyScO_3$ (4-4.1%) is more-readily available than $PrScO_3$ and has lower mismatch than $SrTiO_3$. As such, it should be a better substrate for probing the properties of $BaSnO_3$. Indeed, the current record mobility for thin-film $BaSnO_3$ (around 180 $cm^2/V{\cdot}s$, though based on the discussion in Section 1.3.4 there may be significant systematic error) was achieved on $DyScO_3$ (001) [76], while films on $SrTiO_3$ have not exceeded 120 $cm^2/V{\cdot}s$. Still, 4% mismatch is extremely large for epitaxial growth, and relieving this strain requires significant structural accommodations. The strain here is large enough that the film likely grows relaxed.

Figure 4-14 shows plan-view transmission electron microscopy (TEM) of $BaSnO_3$ grown on $DyScO_3$ (001). Figure 4-14(a) shows overall high film quality with the exception of small areas with low brightness. Figure 4-14(b) zooms into an area with these areas, demonstrating from the Burger's circuit that they are threading dislocation cores with edge character having Berger's vector $a_{BSO}{\cdot}\{100\}$. TEM analysis measures a dislocation density of $3.0{\times}10^{11}$ cm^{-2} on $DyScO_3$ (001), which is comparable to another work's reported density of $1.2{\times}10^{11}$ cm^{-2} [76]. The dislocation line direction $\vec{t}$ for these threads lies along the growth direction, meaning the extra plane of atoms terminates within the film rather than along the film-substrate interface. These threading

dislocations likely form from the coalescence of multiple nucleation sites on the substrate as the film begins growing. This is supported by the RHEED patterns at the onset of film growth shifting from streaky (substrate) to slightly spotty (film nucleation), and back to streaky (film coalescence). The absence of a large density of misfits also suggests that the $BaSnO_3$ likely grows relaxed from the start.

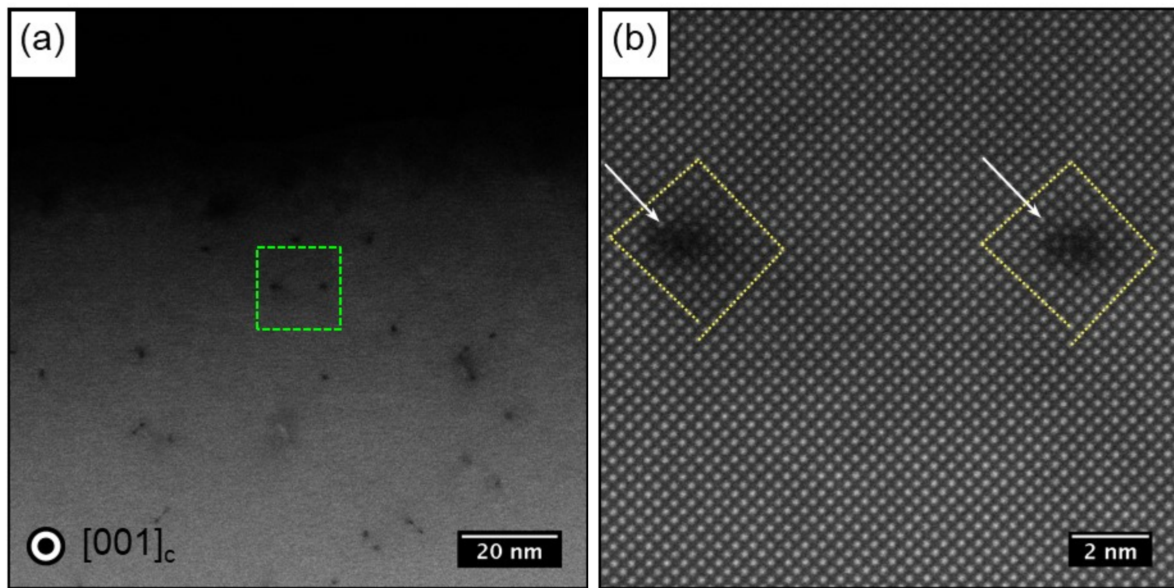

Figure 4-14: Plan-view transmission electron microscopy of 50 nm $BaSnO_3$ grown on $DyScO_3$ $(001)_o$. Dislocation cores are marked by white arrows. TEM courtesy of Honggyu Kim.

There also exists an additional component of shear mismatch between the orthorhombic substrate and cubic film. That is, the orthorhombic crystal structure of the $DyScO_3$ $(001)_o$ substrate gives pseudo-cubic in-plane directions $[100]_{pc}$ and $[010]_{pc}$ (corresponding to $[110]_o$ and $[1\bar{1}0]_o$) which are not orthogonal. Instead, the angle between them is only 87.7°. If growth initiates via nucleation and coalescence, some $BaSnO_3$ nucleation sites should align to $DyScO_3$ $[110]_o$ while other sites align to the $[1\bar{1}0]_o$. This appears to be the case in cross-section TEM based on changes in contrast

with electron probe alignment, as shown in Figure 4-15. While not easily visible in plan-view TEM, in cross-section there are regions within the film of high brightness and low brightness. By rotating the electron probe in the plane of the film, the brightness of each domain can be maximized (indicating better alignment). As such, this indicates a clear in-plane rotation between these two domains, which are misaligned 1-2° from each other (The exact angle is difficult to determine exactly in the TEM). This corresponds closely to the 2.3° offset from orthogonal in $DyScO_3$ $(001)_o$.

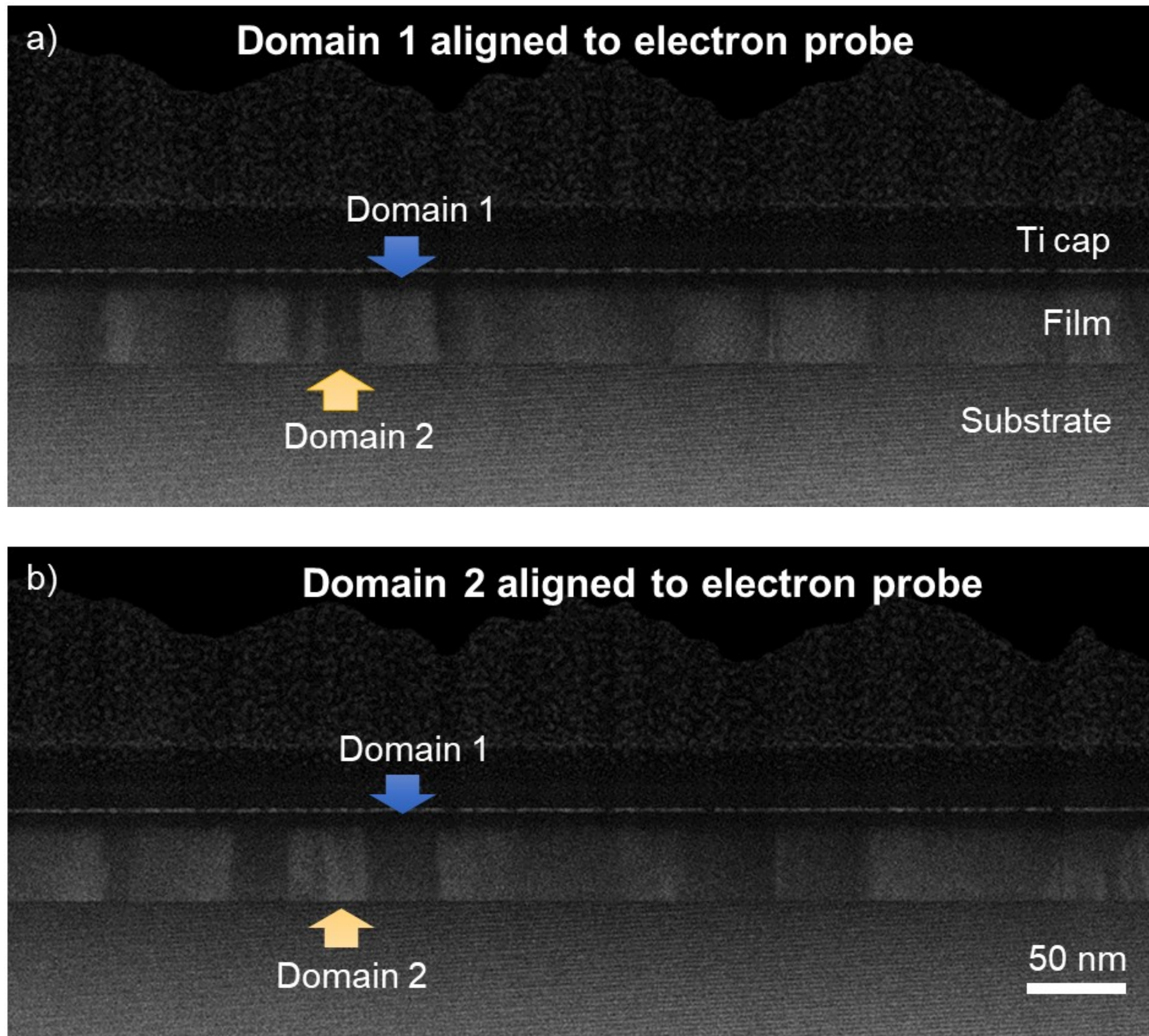

Figure 4-15: Cross-section transmission electron microscopy of 50 nm $BaSnO_3$ grown on $DyScO_3$ $(001)_o$. TEM courtesy of Honggyu Kim.

It is important to contrast the growth mode described here (grain nucleation and coalescence) with that of $BaSnO_3$ on $SrTiO_3$. In that system, work here at UCSB has demonstrated that relaxation occurs through the formation of misfit dislocations at the interface [78]. This is despite mismatch strain being moderately higher on $SrTiO_3$ (5.1% vs. 4.0%). Growth on $SrTiO_3$ behaves as expected, with expected dislocation densities from a simple strain calculation in close agreement with measured spacing (~8 nm

between misfits) [78]. Even for growth on $PrScO_3$ $(110)_o$, with ~2% mismatch, misfit dislocations are seen at the film-substrate interface to relieve strain.

While the extended defects seen here in TEM are present at relatively high densities, the mobilities of these films are among the highest observed in thin films. Moreover, despite the difference in dislocation density between films on $DyScO_3$ and $PrScO_3$, measured mobilities are comparable – around 150 $cm^2/V\cdot s$. This is despite the lower dislocation density for $BaSnO_3$ grown on $PrScO_3$.

4.7 Variations in growth rate within a single growth

Initial data has suggested that growth rate remains fairly consistent throughout growth. For example, the data shown in Figure 4-1 includes several samples grown for much longer than 90 minutes to increase the thickness. Despite having much longer growth times (up to 210 minutes), these samples still follow a very similar trend in growth rate with Ba flux, and are difficult to pick out from the rest of the series. This suggests that, at least in the growths shown in Figure 4-1, the growth rate does not change significantly with how long the growth has been running. Additionally, there is typically very little change in Ba beam flux measurements from day to day.

4.8 Inconsistency and non-uniformity in Hall measurements

Irregularities in the Hall measurements for some of these $BaSnO_3$ films are a cause for concern that should be addressed. For Hall measurements, symmetry in the sample is required, such that a 90° rotation of the current and voltage probes around the magnetic field axis should yield the same results. If this is not the case, the Hall

measurement should not be considered reliable. For some $BaSnO_3$ samples, this asymmetry is observed. However, special care was taken for the series discussed in Section 4.3 where film thickness was held more consistent. Nevertheless, some samples still exhibited this asymmetry. The measurements taken are shown for sheet resistance and Hall resistance along two directions in Figure 4-16. Note that there are two samples with ratio between 23 and 24 (~23.6 and 23.9), which overlap slightly. The sample with ratio 23.6 (shown with hollow markers) shows some disagreement in the longitudinal resistance between the two directions, though the Hall resistance is consistent. For this reason, the sample with ratio 23.9 was grown to confirm that this sample could be grown without this issue. While this sample was more consistent Other than the sample with ratio 23.6, the only ones with disagreement in the longitudinal resistance were those with poorest stoichiometry, either Ba- or Sn-rich (ratios above 60 or below 15).

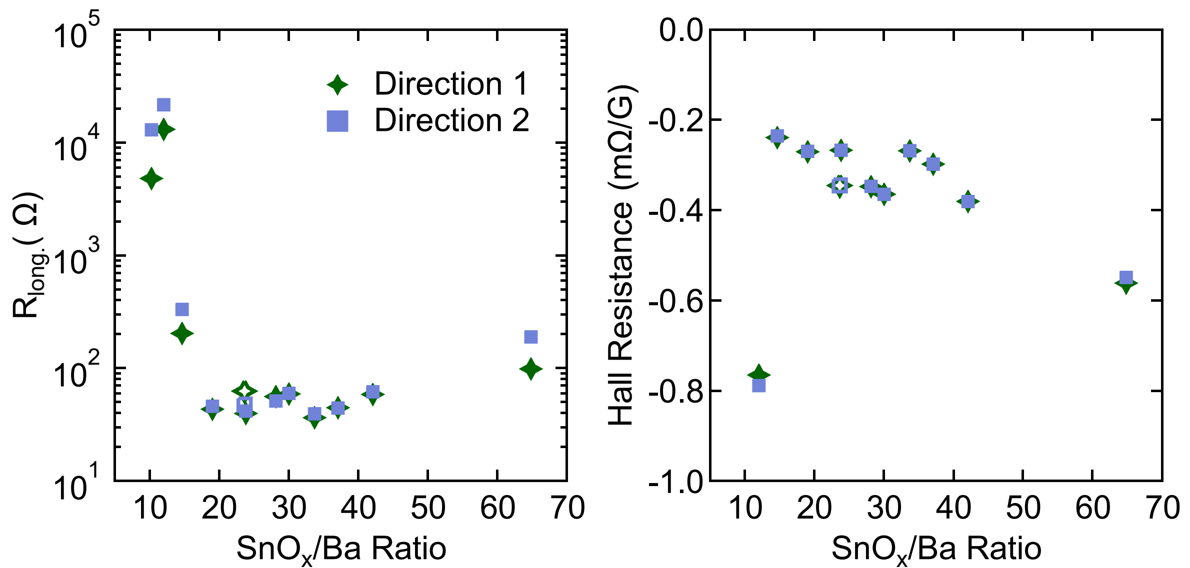

Figure 4-16: Asymmetry in the sheet resistance and Hall resistances for $BaSnO_3$ films on $DyScO_3$ (001). The 23.6 ratio sample with anisotropic $R_{longitudinal}$ is shown with hollow markers.

For the Hall resistance, there was less disagreement than the sheet resistance in general. The two showing the most disagreement were those with ratios around 12 and 65. Again, these are outside of the range with good stoichiometry, which may explain this asymmetry. While the samples shown here are relatively consistent in the two directions, this is not necessarily the case for all of the $BaSnO_3$ films, especially those grown during the beginning stages of development discussed in Sections 4.1 and 4.2. This large error in longitudinal resistance leads to errors at least as large in the sheet resistance, which is directly proportional to mobility. As such, with cases like the sample with ratio 23.6, disagreement in lateral resistances by 30% can lead to huge errors in Hall mobility.

4.9 Conclusions

Even though the growth of $BaSnO_3$ has proven challenging, this work has come a long way in better understanding the growth and how it can be utilized in devices. For the general growth of $BaSnO_3$, it has been demonstrated that

- **all** growths so far have a Ba-limited growth rate
- films' electrical properties degrade at high Ba flux
- increasing SnO_x flux only moderately counters this degradation

This suggests that despite high SnO_x flux, Sn incorporation is a limiting factor. This may be due to the volatility of SnO, which reportedly leads to the opening of a growth window. In order to increase growth rate, this desorption needs to be limited. One such

manner of doing so is the reduction of substrate temperature, but below a certain limit (around 750 °C), the perovskite structure no longer forms.

The primary aim of this work was not only to improve the consistency of $BaSnO_3$ growth, but also to improve the electron mobility for making devices. While maximum room-temperature mobility remains relatively unchanged, this work has nevertheless clarified several questions about the transport in $BaSnO_3$:

- Growing under high Ba flux leads to a 'Ba-rich' condition, which significantly reduces mobility and then carrier density
- There appears to be no drop in mobility under 'Sn-rich' conditions (high SnO_x flux and low Ba flux)
- Activated oxygen flux should be maximized to achieve the best mobility
- Localizing dopants near the top surface leads to lower mobility, but less depletion

5 HETEROSTRUCTURES WITH $BaSnO_3$ FOR CHARGE MODULATION/GATING

As discussed in Section 1.3.5, one draw for the use of $BaSnO_3$ in transistors is the ability to incorporate other perovskite oxides with useful properties, such as the extreme dielectric constant of $BaTiO_3$, or interfacing with (polar) rare earth titanates for the insertion of a high-density two-dimensional electron gas. This chapter deals with initial efforts to leverage the interfacing with other perovskite structures with the hope of demonstrating some of these capabilities.

5.1 Attempts to modulation dope $BaSnO_3$ with $La:SrTiO_3$

Modulation doping has long been a pivotal factor in achieving record mobilities in III-V systems. The fundamental concept is that dopants in the crystal lattice have a different charge than the atoms they replace. This charge disrupts the periodicity locally and introduces a scattering site that interacts more readily with flowing electrons [60]. Modulation doping is a means to separate the scattering center (i.e. the charged dopant ion) from the free carriers it is meant to introduce. By interfacing the intended charge channel (undoped) with a system having a higher conduction band level (doped), electrons can fall into the conduction band of the intended channel material. This is depicted in Figure 1-24.

Mobility in single-crystal samples is believed to be limited by both ionized impurity scattering (from dopants) and electron-phonon scattering with the LO phonon [60]. The mobility of 300 $cm^2/V{\cdot}s$ at room temperature is believed to be limited by nearly equal contributions from both mechanisms. This suggests that a reduction of ionized impurity scattering could yield room-temperature mobilities of 600 $cm^2/V{\cdot}s$. For thin films, however, mobilities below 200 $cm^2/V{\cdot}s$ suggest an additional scattering mechanism is at play. One clear contributor is scattering due to dislocations, which have very high density in $BaSnO_3$ films due to the large substrate-film lattice mismatch. While these additional contributions to scattering in thin films suggest that modulation doping may not dramatically increase mobility, modulation doping still holds major benefits for transistor properties. Namely, modulation doping may allow for a thinner $BaSnO_3$ layer, which could conceivably be thin enough to be partially or fully strained

to the other layers in the structure. In addition to reducing dislocations if the $BaSnO_3$ layer is not fully relaxed, the applied strain could serve to further increase the mobility. The localization of charges closer to a gate can also provide stronger charge modulation.

For a first test, La:$SrTiO_3$ was tested as a source of carriers for modulation doping $BaSnO_3$. As mentioned, a conduction band offset is required to force carriers from the injection layer ($SrTiO_3$) into the $BaSnO_3$. According to theoretical calculations [94], the $SrTiO_3$ conduction band is offset 1.14 eV above that of $BaSnO_3$. This calculation, however, relies on the O 2p level moving significantly in $BaSnO_3$, which would be contrary to all former understanding of these perovskite structures. For a 2Å doping thickness spaced 2 nm from the $SrTiO_3/BaSnO_3$ interface, this offset would permit confinement of 8×10^{13} cm^{-2} without spillover. Other work, however, has experimentally demonstrated smaller band offsets of only 0.4 eV ± 0.2 eV [95]. Even if only a portion of the dopants are injected into the $BaSnO_3$ layer, measured mobility should be elevated above that of $SrTiO_3$ (about 10 $cm^2/V\cdot s$ at room temperature [140]). This was further discussed in Section 1.3.5.

First, approximately 30 nm of undoped $BaSnO_3$ was grown on $GdScO_3$ (110), followed by 20 nm of heavily La-doped $SrTiO_3$. $GdScO_3$ was chosen due to its mismatch with $BaSnO_3$ being relatively small compared to other commercially available substrates (See Section 1.3.1). To further increase lanthanum doping, $SrTiO_3$ growth rate was reduced to approximately 60 nm/hr (typically it is grown near 140 nm/hr). This is done instead of increasing lanthanum cell temperature because, in the past, significant damage has been done to a lanthanum cell above 1300 °C. In an effort to extend the life

of the cell, this is now the highest temperature used. This is expected to yield a lanthanum doping concentration of ~ 1×10^{14} cm^{-2}. This high carrier density was chosen to compensate for the considerable surface depletion that is known to occur in $SrTiO_3$, primarily due to pinning of the Fermi level at the surface [141].

Post-growth atomic force microscopy showed a large degree of non-uniformity across the sample surface (Figure 5-1). Additionally, some regions appear to have cracks in the surface. This is likely due to the large tensile mismatch in the $SrTiO_3$, which in oxides is known to relax by forming cracks rather than nucleating dislocations. On $GdScO_3$, $SrTiO_3$ has been found to crack at thicknesses below 30 nm, but the mismatch between $SrTiO_3$ and $BaSnO_3$ is even higher. Furthermore, there is a significant density of what appears to be pinholes in the $SrTiO_3$ layer, though the depths cannot be resolved by the AFM tip. These pinholes could point to a wetting issue of $SrTiO_3$ on $BaSnO_3$, or be related to the large lattice mismatch.

If wetting of $SrTiO_3$ on $BaSnO_3$ is an issue based on their relative surface energies, this requires that the inverse should not have the same problem. In addition, the growth of $SrTiO_3$ on $BaSnO_3$ has not been as high quality as $SrTiO_3$ growths on bare substrates. For instance, no RHEED oscillations are visible (which are typically observed), and the post-growth RHEED showed no surface reconstructions, despite being relatively smooth in AFM. This could be caused by either the wetting issue or the rough post-growth $BaSnO_3$ relative to the bare substrates. If differences in surface energies lead to the poor growth of $SrTiO_3$ on $BaSnO_3$, the reverse case should yield better growths. This

is clearly true based on the number of successful growth studies of $BaSnO_3$ on $SrTiO_3$ substrates.

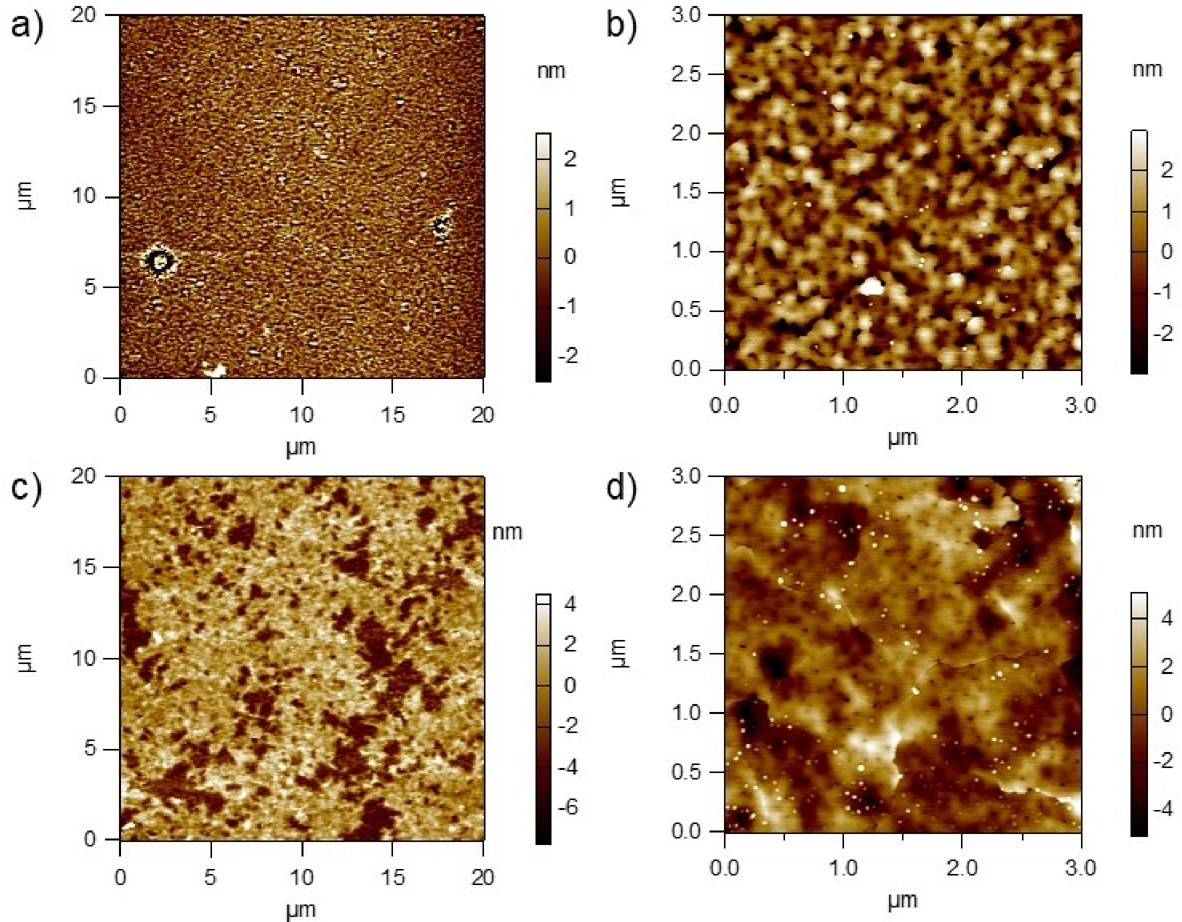

Figure 5-1: Atomic Force Microscopy images of multiple regions (a and b vs. c and d) of a $GdScO_3$/~25 nm $BaSnO_3$/~20 nm La:$SrTiO_3$ sample, demonstrating non-uniformity in the growth. There is also a large density of pinholes, and in some regions there appears to be cracking.

5.2 Heterostructures with $BaTiO_3$ for gating

While modulation doping is not immediately necessary for the fabrication of transistors with $BaSnO_3$, the growth of heterostructures for gating is. As discussed in

Section 1.3.5, $BaTiO_3$ not only allows for gating above 10^{14} cm^{-2}, it also can have the additional affect of reducing lateral fields within the device due to its high dielectric constant. With its comparatively lower mismatch of 3%, it should have a critical thickness on $BaSnO_3$ on the order of 10 nm. In order to combat the leakiness that was likely to occur as a result of the dislocations already threading through the $BaSnO_3$ into the $BaTiO_3$, a gate oxide thickness of 20 nm was chosen on 30 nm $BaSnO_3$. For these $BaSnO_3$ layers, only the top 10 nm were doped, with a 20 nm UID buffer between this and the substrate. Based on similar $BaSnO_3$ films grown under the same conditions, a carrier density of 1×10^{14} cm^{-2} was expected. AFM of the surface is shown in Figure 5-2. X-ray diffraction is also shown for the same structure in Figure 5-3. While the surface looks relatively smooth, the diffraction pattern shows highly asymmetric peaks, as well as two peaks between 44° and 45° that are not well-explained by any of the phases expected. It does appear the $BaTiO_3$ peak is shifted towards the substrate as a result of the tensile strain applied by the relaxed $BaSnO_3$ below it.

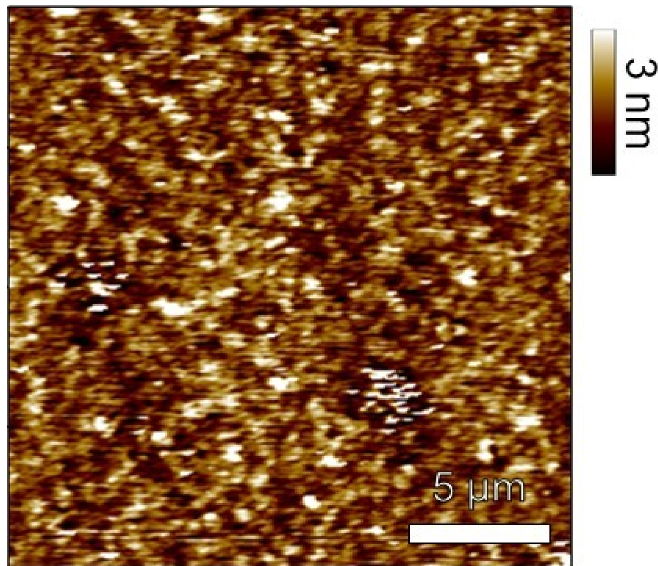

Figure 5-2: Atomic force micrograph of the heterostructure with 20 nm $BaTiO_3$/30 nm $BaSnO_3$/$DyScO_3$.

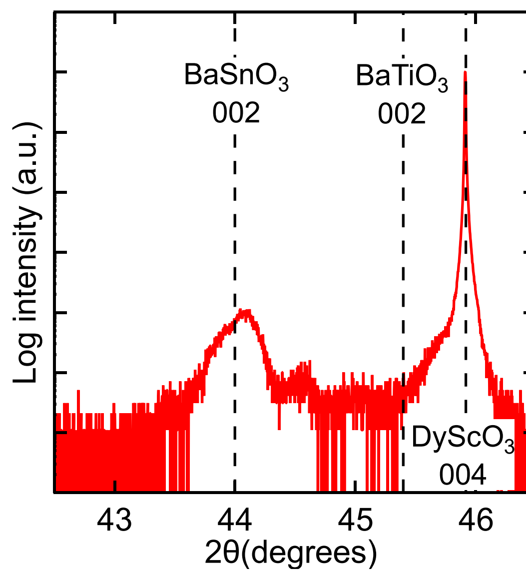

Figure 5-3: X-ray diffraction pattern for the 20 nm $BaTiO_3$/30 nm $BaSnO_3$/$DyScO_3$ (001) heterostructure

In collaboration with Rajan Group at the Ohio State University, devices were fabricated with this sample [92]. By scratching through the $BaTiO_3$ layer and placing indium dots, electrical contact was made to the $BaSnO_3$ layer. Upon measuring, a carrier

density of 2.7×10^{13}cm^{-2} was measured, which is well below the expected 1×10^{14} cm^{-2}. This is likely due to a combination of the free surface pinning the Fermi energy of $BaTiO_3$ (a well-known effect in $SrTiO_3$ [141]) and the ferroelectricity of the $BaTiO_3$ film. Given the known polarization of $BaTiO_3$ at room temperature of 0.16 C/cm^2, this could potentially yield a charge modulation of up to 10^{18}/cm^2 [25]. Clearly the observed modulation is much smaller, which indicates that the $BaTiO_3$ is not fully ferroelectric out-of-plane. There may be multiple ferroelectric domains with different polarization directions, including in-plane, which explains some of the diminished effect. Upon putting a gate metal onto the structure, another change in carrier density to 8×10^{13} cm^{-2} was observed. This modulation is likely explained by the electrical contact of the Pt metal gate contact altering the surface potential of the $BaTiO_3$ layer to give the anticipated Schottky barrier of around 1.2 eV [59]. A transistor structure was fabricated, as described in Ref. [92]. With this device, the measured on-off ratio was almost 500 at room temperature, and breakdown voltage was 65 V.

To further improve performance, charge within the channel should be reduced for more effective gating. To do this, another structure was grown, this time with 50 nm of UID $BaSnO_3$ instead of 20 nm. Because of the drop in mobility seen at lower thicknesses and lower doping densities, the hope was that by increasing thickness, the drop to lower carrier density would not degrade mobility as badly. For this structure, a doping density of 7×10^{13} cm^{-2} was targeted. Referencing bare $BaSnO_3$ samples from this series with the same thickness as the channel layer in these heterostructures, this should give a mobility of ~85 cm^2/V·s. Figure 5-4 shows AFM of this structure after growth.

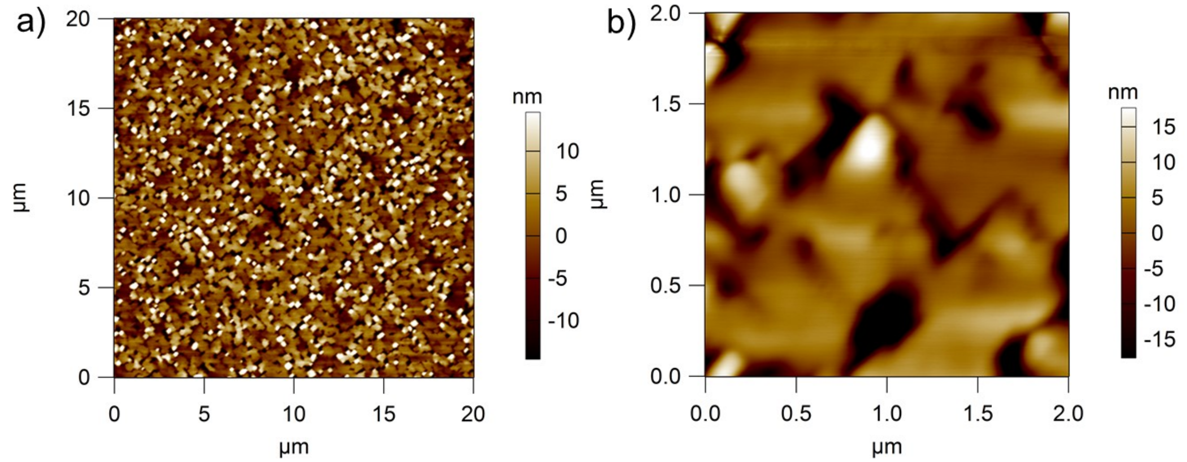

Figure 5-4: Atomic force microscopy of a representative $BaTiO_3$/La:$BaSnO_3$/$DyScO_3$ heterostructure. $BaTiO_3$ thickness is 20 nm on ~60 nm of $BaSnO_3$.

As seen from the AFM, there are large pits that are approximately the same thickness as the $BaTiO_3$ layer (20 nm). This is rather surprising, since there was no evidence of any de-wetting or pitting in the film observed in Figure 5-2. This is especially surprising due to the improved roughness of the $BaSnO_3$ layers between the first heterostructures and this set. Figure 5-5 shows atomic force microscopy of a bare $BaSnO_3$ film grown in the same series as the heterostructure in Figure 5-4. For this sample, the roughness is much lower than typical for $BaSnO_3$. In this film, however, there are clearly pinholes forming, though the aspect ratio is potentially too high for AFM to resolve.

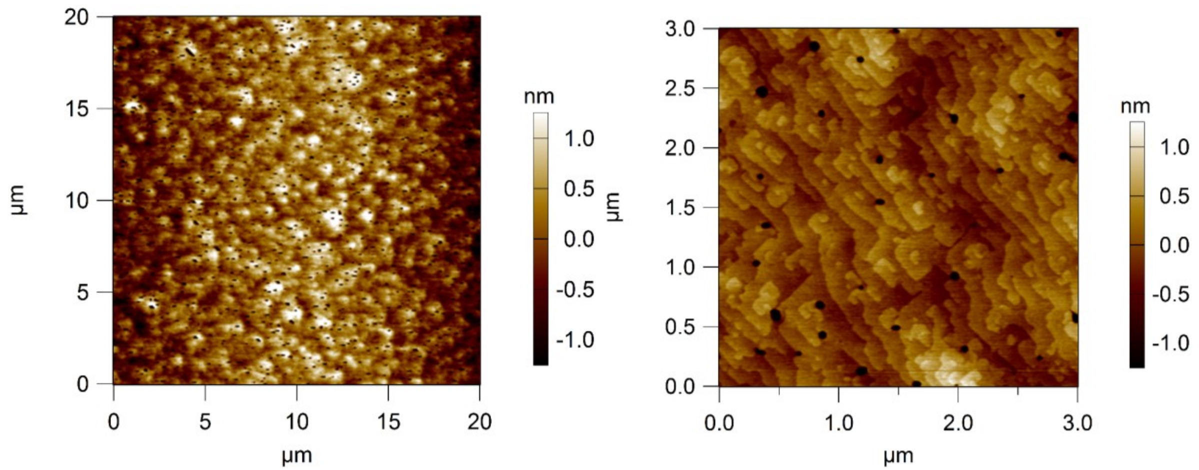

Figure 5-5: Atomic force microscopy of a bare 60 nm $BaSnO_3$ film grown under the same conditions as the heterostructure shown in Figure 5-4.

At this point in the growth series, there was a problem with the SnO_2 cell, which prevented further growths of $BaSnO_3$. In order to grow more heterostructure samples for gating experiments, previously-grown $BaSnO_3$ films on $SrTiO_3$ substrates were used as a starting point to regrow a $BaTiO_3$ top gate. For these samples, $BaSnO_3$ thickness ranged from 20-25 nm. Atomic force microscopy of one of the sample surfaces is shown in Figure 5-6. As with the heterostructures grown on $DyScO_3$, film coalescence seems to be an issue. For these samples, however, it does not appear that the pits are nearly as deep, as seen by the much smaller scale bar. This is possibly related to the lateral size of the pits, which are narrower for these samples. It remains unclear why this was not a problem for the first series of $BaTiO_3$/$BaSnO_3$ heterostructures. This appears to be a wetting problem similar to what was seen for $SrTiO_3$ on $BaSnO_3$. One would expect this issue could be mitigated by increasing growth rate or decreasing substrate temperature at the start of growth to help with the coalescence of the $BaTiO_3$ layer. However, this first heterostructure set was actually grown at a substrate temperature of 920 °C, while

the later sets were grown at a (slightly) lower temperature of 900 °C. The success of the first set does, however, give hope that the wetting problem can be avoided again in the future.

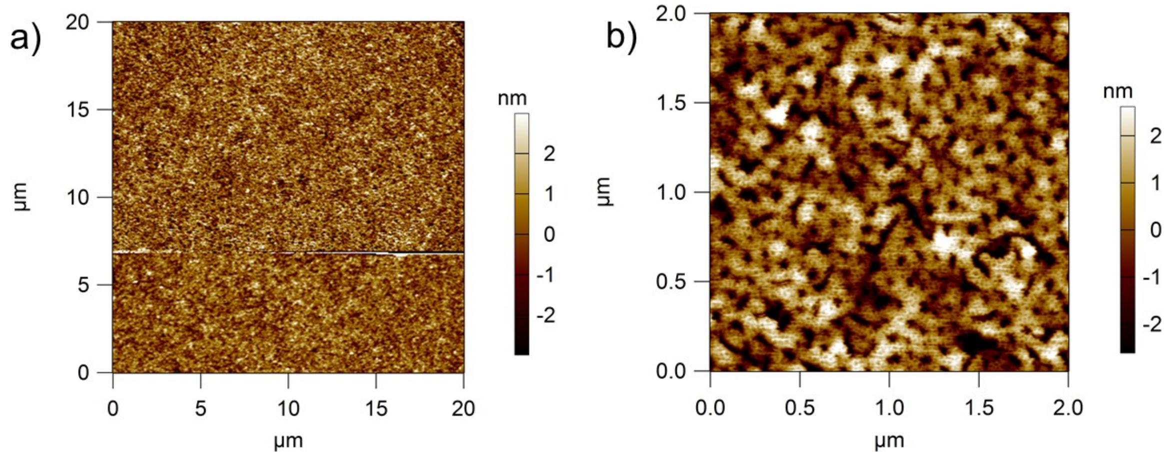

Figure 5-6: Sample surface of 20 nm $BaTiO_3$ grown on previously measured La:$BaSnO_3$ films on $SrTiO_3$ substrates by atomic force microscopy.

Characteristic x-ray diffraction patterns for the two sets of the samples with pits are shown in Figure 5-7. While the surfaces are much rougher than the first set grown, the diffraction patterns look much better than for the sample shown in Figure 5-3. No strong thickness oscillations are seen for the low-roughness $BaSnO_3$ or $BaTiO_3$ layers, but this is not entirely surprising given the pitting problem. Once again, the $BaTiO_3$ peak appears shifted from the bulk value. This indicates that it is at least partially strained to the $BaSnO_3$ layer underneath, though the fully strained peak position would be expected around $2\theta = 46.5°$.

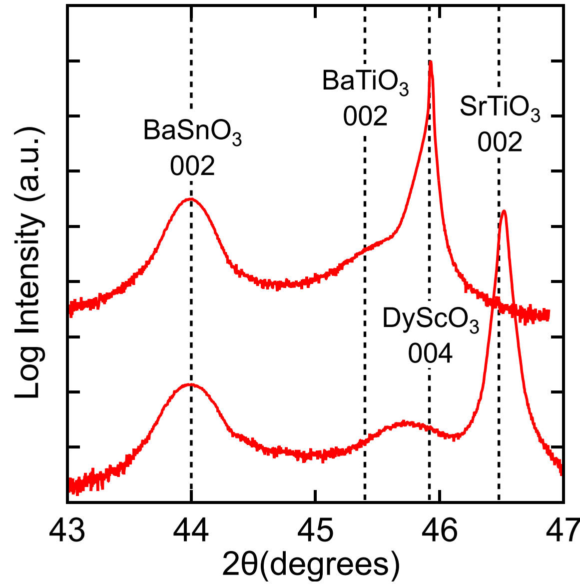

Figure 5-7: X-ray diffraction patterns for $BaTiO_3$/La:$BaSnO_3$/$DyScO_3$ (top) and for $BaTiO_3$/La:$BaSnO_3$/$SrTiO_3$ (bottom) heterostructures.

5.3 Conclusions

The growth of heterostructures with $BaSnO_3$ will be essential for the eventual fabrication of useful transistor devices. Fortunately, there are a number of perovskite systems with advantageous properties for fabricating more effective transistors. One key factor is conduction band offset, of which both $SrTiO_3$ and $BaTiO_3$ have. While $SrTiO_3$ was tested as a source of modulation doping, initial tests were unsuccessful. Both $BaTiO_3$ and $SrTiO_3$ seem to create difficulties when grown on top of $BaSnO_3$, exhibiting a roughening of the surface and de-wetting that either forms deep pits in the film or prevents complete coalescence. Nevertheless, successful heterostructures of $BaTiO_3$/$BaSnO_3$ were grown on $DyScO_3$ (001). While there is no clear evidence for what caused the success of one set of heterostructures while the others de-wetted, it provides

hope that de-wetting can be avoided again in the future to enable high-quality heterostructures.

6 SUMMARY AND FUTURE DIRECTIONS

6.1 Summary of BST varactor work

Previously, it was demonstrated that the performance of $Ba_xSr_{1-x}TiO_3$ tunable capacitors could be dramatically improved by leveraging a hybrid MBE growth process. This work has demonstrated some of the causes of this performance increase by investigating two main factors: film stoichiometry and film-contact interfacial quality. As expected, BST stoichiometry is an important factor in achieving high Q at zero bias. However, optimum real device performance may not require perfect stoichiometry, since the serviceable bias range grows when growing (Sr,Ba)-rich films. The importance of high interface cleanliness and quality is also emphasized, as it improves device tunability and allows for lower biases to be used. This work also demonstrated a method

by which to extract interfacial capacitance from fits to the measured dielectric constant as a function of field. Device performance was further improved by improving the roughness of the BST/top contact interface, and this, in combination with a minimally-damaging mesa etch, appear to have reduced the effects that are typically seen which degrade performance of smaller devices. Our collaborators' work continues focusing on processing and passivation to reduce leakage through the BST surface, as well as confirming this high-performance from low-frequency measurements into the RF regime. After this point, the biggest remaining hurdle for the adoption of BST tunable capacitors is the cost of the MBE process.

6.1.1 Designing high-frequency parallel plate capacitors

Because device behavior is dramatically different at RF frequencies, a number of additional considerations are required. One of the most significant differences over the parallel plate capacitors used in this study is simply shrinking device size in order to reduce capacitance to push the $1/\omega R_s C$ series roll off to higher frequencies (as described in Section 1.2.3.2). This requires device sizes at or below 2×2 μm^2. For GSG probes, this represents an incredibly small pad to contact. Our collaborators have designed a mask which offsets the top contact pad from the BST surface with minimal effect on series resistance. This is primarily through the use of thick gold deposited in addition to the Pt contacts deposited by sputtering at high temperatures.

While depositing thick gold to reduce series resistance is effective, there is a limit to this effectiveness because of the skin effect. This is caused by eddy currents, which are

induced by the changing magnetic field that results from the applied AC current. This causes the current density to decrease exponentially moving inward from the surface. The general formula for skin depth is given below.

$$\delta = \sqrt{\frac{2\rho}{\omega\mu}}\sqrt{\sqrt{1+(\rho\omega\epsilon)^2}+\rho\omega\epsilon} \tag{6-1}$$

For gold at 10 GHz, the skin depth is only 0.7 μm. As a result, any thicker contacts will not greatly reduce the series resistance measured in the device.

As mentioned in Section 3.5.2, reducing device size also tends to reduce Q. While unclear if this effect is dramatic in our devices, efforts still need to be made to mitigate it. One simple way to reduce P/A and achieve the same capacitance is to change device mesa/contact shapes to circles rather than squares. The gains here will be small, however. Device area could also be increased at constant capacitance by growing thicker BST films, since $C = \epsilon A/d$. For more dramatic size changes, devices with larger device area (and capacitance) could be used, but connected together in series. Because total capacitance adds inversely in series, this would reduce total capacitance, but the individual capacitor Qs would be higher.

6.2 Summary of $BaSnO_3$ work

While there has been no real improvement in $BaSnO_3$ thin film mobilities, there is certainly a better understanding of the film growth and stoichiometry of these films. We have demonstrated the relative tolerance of $BaSnO_3$ mobility to the addition of excess Sn, even in such excess that an additional SnO_2 phase is present in XRD. This suggests that a closer look needs to be taken into what others have called an adsorption-

limited growth, where stoichiometry is supposed to be self-limiting. This work indicates that a relatively consistent mobility for a range of growth conditions may not necessarily indicate perfect stoichiometry.

Efforts were also made to understand the cause of depletion and reduced mobility in thinner films. While still unclear, it is evident that dopants do not behave uniformly through the thickness of the film. Because the interfaces between the film and air/substrate remain spaced the same, this suggests some kind of complexing or passivation that changes activation of the dopants differently through the film thickness.

Many hurdles still stand in the way of making reliable, high-performance $BaSnO_3$ transistor devices, but there is a clear path forward. That path starts with understanding the charge depletion and mobility reduction observed when growing $BaTiO_3$ on $BaSnO_3$, as discussed in Section 5.2. Efforts also need to be made to better understand consistency between growth series, which appears to largely be a challenge due to the SnO_2 powder source. A reduction in the dislocation density should also be further investigated

6.2.1 Consistency of $BaSnO_3$ growths

To improve reliability between growth series, there needs to be a better understanding of how source fluxes or temperatures relate to final growth conditions. This is a challenging problem to tackle, since the contents and chemistry of the SnO_2 crucible changes over time as material evaporates. This is especially difficult for a

ceramic (alumina) crucible, where the temperature profile through the crucible/material is also then changing as material evaporates. Ideally, there would be some correlation between the compounds in cell flux and some other parameter that could be measured, which could be used to recalibrate the growth conditions over time. In the absence of this, a reduced crucible lifetime may be needed, similar to the way sputter targets requiring high-consistency growths are only considered useful when their material is between around 30-70% depleted. While there is never a desire to open a functioning MBE system more frequently, this path should at least be considered if it can improve the consistency of growths.

Moreover, there are still additional problems with the growths, even once suitable conditions have been found. For instance, the presence of an additional SnO_2 peak in x-ray diffraction for nominally stoichiometric $BaSnO_3$ is troubling, and indicates that there is still a lot about the growth that is not understood. Fortunately, the mobility seems highly tolerant to this additional phase. Nevertheless, these phases will certainly be detrimental to the mobility, and need to be addressed.

6.2.2 Buffer layers to reduce misfits in and $BaSnO_3$

Another significant challenge for the growth of high-mobility $BaSnO_3$ is the high dislocation density, which results from a lack of closely lattice-matched substrates. While efforts are being made to grow single-crystal $BaSnO_3$, the largest crystal sizes are around 2 mm, making their use as substrates a challenge. Their use is limited further by the need for the crystals to be undoped, such that film properties could be probed

rather than just substrate properties. In the absence of a suitable substrate, buffer layers with closer lattice mismatch can be an effective alternative. There have been efforts to grow a $BaTiO_3$ buffer for $BaSnO_3$ that are not described in this work. This work, however was unsuccessful in improving the film properties of $BaSnO_3$, possibly related to the interesting effects currently seen at the interface between $BaSnO_3$ and $BaTiO_3$ (See Section 5.2).

Another interesting buffer choice would be $SrZrO_3$, the growth of which has been successfully demonstrated with a hybrid MBE growth method [103]. With a wide band gap of 5.6 eV, and a lattice constant of 4.103 Å, this is an interesting material to use as a back barrier for $BaSnO_3$ as well. Moreover, $SrZrO_3$ can be alloyed with $SrTiO_3$ to create a solid solution between the two. This opens up an opportunity not only for tuning the conduction band offset to $BaSnO_3$. More importantly, it can be used as a graded buffer, which has been used with great success in GaN growth [142], [143], to further reduce dislocations in the active $BaSnO_3$ layer. $SrZrO_3$ could also be alloyed with $BaZrO_3$, with a lattice constant of 4.19 Å, to apply moderate tensile strain. Care has to be taken in this case though, since oxide films crack under moderate tensile strain.

6.2.3 $SrSnO_3$ buffers for modulation doping $BaSnO_3$

While work has been done to grow $SrSnO_3$ by the same MBE process used to grow $BaSnO_3$ here [65], progress has been limited. This is primarily due to difficulties with doping $SrSnO_3$ films, which elsewhere have been demonstrated with good conduction and mobilities above 50 $cm^2/V\cdot s$ [144]. $SrSnO_3$ has a calculated band offset of 1.05 eV to

$BaSnO_3$ [3]. This compares well with the measured band gap of 3.93 eV for $SrSnO_3$ [145]. This offset, in combination with comparable lattice spacing compared to other available substrates, makes $SrSnO_3$ yet another candidate as a back barrier or to modulation dope $BaSnO_3$.

Transmission electron microscopy gives a clear indication of why the $SrSnO_3$ films grown by our MBE process cannot currently be doped. Figure 6-1 shows transmission electron microscopy of one of the films, which has an extremely high density of antiphase boundaries. These appear to originate at the substrate, and travel vertically through the thickness of the film. As seen from Figure 6-1b, this antiphase boundary is the result of a ½ unit cell shift. This is the same shift for Ruddlesden-Popper type stacking faults seen as a way to incorporate excess Sr in $SrTiO_3$ [146]. This may be caused by poor registry between the film and substrate, since these defects appear to originate very close to this interface. If this truly is a problem of substrate-film registry, this should be resolved by growing a few monolayers of $BaSnO_3$, in which these defects are not observed, prior to the growth of $SrSnO_3$. This, however, is a challenge in itself because $BaSnO_3$ tends to grow rough at the beginning of growth, then smooth after the first few monolayers. While $SrSnO_3$ could still be grown on a thicker $BaSnO_3$ layer, care needs to be taken to avoid excessive tensile strain in the $SrSnO_3$. Additionally, it is likely many of the excess dislocations associated with the larger mismatch of $BaSnO_3$ to a substrate will thread through to the $SrSnO_3$ layer as well. It is also likely that higher substrate temperatures, or a pause shortly after beginning the $SrSnO_3$ growth, would

allow more adatom motion on the surface which may reduce the density of these defects.

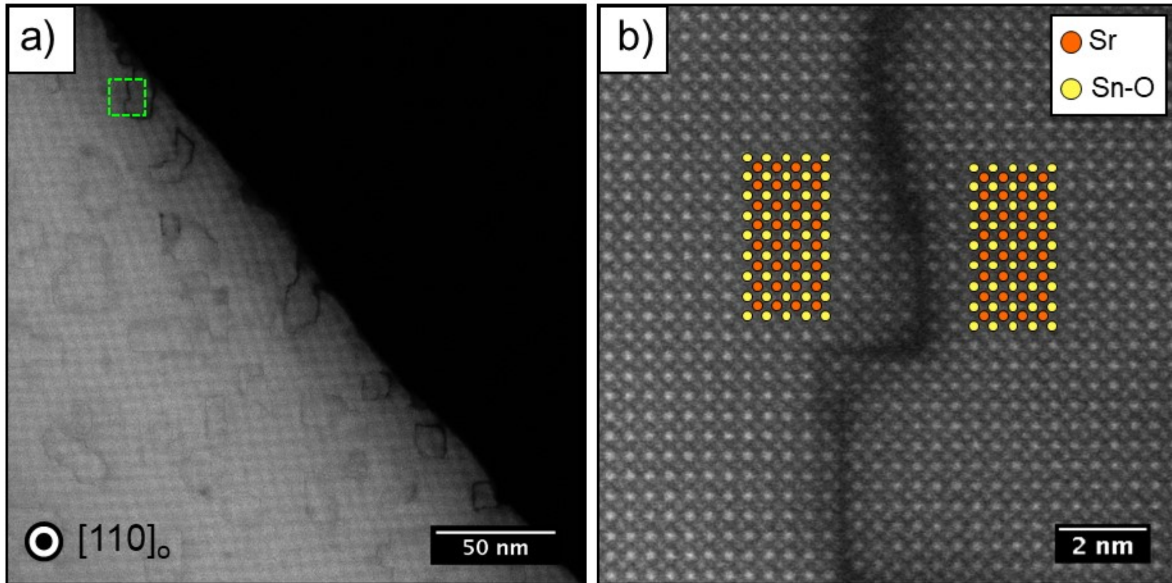

Figure 6-1: Plan-view transmission electron microscopy (courtesy of Honggyu Kim) of a non-conductive La:$SrSnO_3$ film grown on $DyScO_3$ (110) by MBE. The micrograph presents an extremely high density of antiphase boundaries with significant disorder at the boundary.

APPENDIX A: XRD FITTING IN MATLAB

While XRD spectra are frequently used to characterize films quantitatively, we have not historically used a consistent tool for interpretation of the data. While capable tools exist, I have found none which also include the spatial offset in crystal structure between the substrate and film, as discussed in Ref. [120]. To that end, I have written a basic Matlab code for interpretation of the XRD spectra we take which functions for both homoepitaxial or heteroepitaxial films which consist of a single layer on a substrate. This script can, in principle, be extended to heterostructures with multiple film layers as well, though it will add extra fit parameters. The relative simplicity of the fit algorithm means it would likely need to be changed to accommodate these more complicated structures and converge those fits. The functional form for this calculation is

$$E = F_f \frac{1-\exp(-iq_z c_f N)}{1-\exp(-iq_z c_f)} + F_s \frac{\exp[-iq_z(c_f N+\delta)]}{1-\exp(-iq_z c_s)}. \quad \text{(B-0-1)}$$

To calculate XRD measured intensity, we use $I \propto |E|^2$. The wavevector q_z is, by definition, $4\pi\sin(\theta)/\lambda$. Note that this ignores absorption and extinction [120]. The only thing that needs to be changed in this code to perform fits is the definition of the initial-guess parameter matrix (P_i), for which the components are described in the section labeled "`First-guess for numbers that will change in the fit`." The lattice constant of the substrate (here using the pseudocubic d_{110} of $DyScO_3$ (110)) also needs to be defined in the previous section labeled "`Constants that don't change in the fit`." In the initial parameter matrix, you define initial guesses for:

- c_f: the out-of-plane lattice constant of film (in Å)
- n: number of unit cells of film (this number must be an integer)
- δ (delta): the offset between substrate and film (in Å, as described in [120])
- F_f: the ratio of structure factors of the film/substrate
- scale: multiplier for rescaling calculated intensity to measured data
- σ_N (sigN): roughness of the film surface in number unit cells (assumes a gaussian distribution)
- *x*offset: error in twotheta (this should be left as zero in almost all cases)
- *y*offset: offset in intensity (e.g. background)

To account for roughness, the expected intensity curve is calculated for a range of thicknesses. Each calculated curve is then rescaled according to its thickness and the value of the gaussian at that point (centered around N and with standard deviation σ_N defined in the initial guess matrix). These rescaled curves are then summed together to give the expected diffracted intensity. This result is then convolved with a detector function (defined in "`Detector parameters for convolution`").

To perform the fit, the initial parameter matrix P_i is perturbed based on the 'resistance to change' matrix, M, which can define a different 'resistance' for each fit parameter. This is currently defined manually, and the higher the number, the higher the resistance to change. The script then recalculates the intensity curve, and if the goodness of fit is improved, keeps the new parameter matrix. This process continues until the script repeats 5000 times without improving the goodness of fit.

```
function heteroepitaxyXRDfits()
% Fits XRD pattern according to
          http://aip.scitation.org/doi/pdf/10.1063/1.3243696
% Created 11/30/2017 CRF

clc, clear all

%% Define path to 'name'.xrdml data file for XRD intensities

path = <insert directory path here>;
name = <insert filename here>; % use .xrdml file, but don't
          include the extension in name

%%  Structure Factors
%   BaSnO3: 56.115 + j3.627     (0 0 2) BSO on DSO ~4.0997
%   SrTiO3: 54.468 + j3.619     (0 0 2)
%   DyScO3: 226.302 + j43.974   (0 0 4)
%   DyScO3: 164.3 + j32.561     (2 2 0)
%   GdScO3: 224.552 + 51.745    (0 0 4)
%   GdScO3: 183.955 + j38.679   (2 2 0)

%% lattice constants (out of plane)
btotet = 4.036; % this is for c-axis out of plane
btocub = 3.996;
dso001 = 3.945;
dso110 = 3.941;
lsat = 3.868;
pso001 = 4.005;
pso110 = 4.021;
sto = 3.905;
szo001 = 4.098;
szo110 = 4.103;

%% Constants that don't change in the fit
cs = dso110; % lattice constant of substrate
lambda = 1.5406;
fs = 1; % Unit cell structure factor for substrate (leave as 1
          to do ratio of ff/fs)

%% First-guess for numbers that will change in the fit
% cf = lattice constant of film
% n = number of unit cells of film (MUST BE AN INTEGER)
% delta = thickness of layer between substrate and film (Ang)
% ff = ratio of structure factors of film/substrate
% scale = arbitrary prefactor for rescaling intensity to data
% sigN = top surface roughness in # unit cells (gaussian)
% xoffset = error in twotheta
```

```
% yoffset = offset in intensity

%                  cf          n     delta        ff     scale
          sigN   xoffset    yoffset
Pi = str2num('4.1160  106.0000    0.0000    2.1400    6.5000
          2.0000    0.0000          00'); % BSO on DSO
% Pi = str2num('4.1160   39.0000         0    1.2674    7.9042
          2.0000    0.0000          0'); % BSO on STO
% Pi = str2num('3.9866   25.0000    0.5462    1.4122    8.5970
          2.0000    0.0000          0'); % BTO on DSO


%% Imports XRD data from 'name'.xrdml
cd ([path]);
XRD = xml2struct([name, '.xrdml']);

twothetamin =
          str2double(XRD.xrdMeasurements.xrdMeasurement.scan.d
          ataPoints.positions{1, 1}.startPosition.Text);
twothetamax =
          str2double(XRD.xrdMeasurements.xrdMeasurement.scan.d
          ataPoints.positions{1, 1}.endPosition.Text);

int =
          str2num(XRD.xrdMeasurements.xrdMeasurement.scan.data
          Points.intensities.Text);
int = int+0.1; % so that 0’s can be plotted on a log scale
N = length(int);
twotheta = linspace(twothetamin, twothetamax, N);

% semilogy(twotheta,int) % uncomment to plot measured data

%% This section defines the fit and loops through it
count = 0; % number of times a new fit has been tested without
          improving goodness of fit
% P is the parameter matrix (i.e. fit parameters)
% Pi is initial test matrix, which the program modifies
          slightly (to Pf) and calculates a goodness of fit.
          If the goodness of fit is better for the modified
          function, the program keeps it and resets count.
%     P(1    2   3     4  5     6    7     )
% Pi = [cf    n   delta ff scale sigN Xoffset]
Pf = Pi;
M = [10000 000 50 1000 500 10 10000];   % M = resistance to
          change
```

```
test(1,:) = simfit(twotheta,cs,Pi); % calculated fit to Pi
chi2i = sum((log(test)-log(int)).^2); % goodness of fit for Pi

figure(1)
semilogy(twotheta,int,'k-',twotheta,test,'r-')

while 1 % loops through the fit
% by commenting lines out, you prevent the fit from modifying
    Pf(1) = Pi(1).*(1+randn/M(1));
    Pf(2) = Pi(2) + round(randn);
%     Pf(3) = Pi(3).*(1+randn/M(3));
    Pf(4) = Pi(4).*(1+randn/M(4));
    Pf(5) = Pi(5).*(1+randn/M(5));
%     Pf(6) = Pi(6) + round(randn);
%     Pf(7) = Pi(7) + randn/M(7);

    test(1,:) = simfit(twotheta,cs,Pf); % calculated fit to Pf
    chi2f = sum((log(test)-log(int)).^2); % goodness of fit Pf
    count = count + 1;

    if chi2f < chi2i % is new fit better? If so, this keeps it
        testf = test;
        Pi = Pf;
        chi2i = chi2f;
        Pf
        count = 0;
        figure(1)
        semilogy(twotheta,int,'k-',twotheta,test,'r-')
        pause(.01)
    end
    if count == 5000 % ends the program after # tries without
          improved goodness of fit
        count
        break
    end
end

% Print results of improved fit (and measured data)
semilogy(twotheta,int, twotheta,testf)
Pi
chi2i

% Transfer variables to base workspace
assignin('base','test',testf)
assignin('base','fitparams',Pi)

end
```

```
%% Calculates Fit to data
%       1    2   3     4  5     6    7       8
% Pi = [cf   n   delta ff scale sigN xoffset yoffset];

function test = simfit(twotheta,cs,P)
dt = twotheta(2)-twotheta(1); % step size in two theta
box = -3:dt:3;                            % convolves fit with
          gaussian/Lorentzian for the detector
lbox = length(box);
ltwot = length(twotheta);
twoTnew = (twotheta(1) - lbox*dt/2):dt:(twotheta(ltwot) +
          lbox*dt/2);
if(3 * P(6) < P(2))                       % for roughness
          calculation
    N = floor(P(2) - 3*P(6)):1:ceil(P(2) + 3*P(6));
else
    N = 1:1:ceil(P(2) + 3*P(6));
end
lN = length(N);

% calculates a fit for each thickness value defined by the
          roughness and weights according to a gaussian
gaussR = exp(-((N - P(2))/P(6)).^2/2);      % relative
          intensity at each thickness
gnorm = sum(gaussR);
gaussR = gaussR/gnorm; % normalizes gaussR so the sum is 1

twoTnew = twoTnew-P(7);
qz = 4*pi/1.5406*sin(twoTnew*pi/360);

%%  calculates test func. at every roughness, normalizes
          intensity by a gaussian distribution with thickness
 clear temptest;
for i = 1:lN
    temptest(:,i) = gaussR(i)*(0.0001*P(5)*abs(P(4)*(1-exp(-
          j*qz*P(1)*N(i)))./(1-exp(-j*qz*P(1)))+1*exp(-
          j*qz*(P(1)*N(i)+P(3)))./(1-exp(-j*qz*cs))).^2);
end

test = sum(temptest,2);

%%  Calculates test function with no roughness considered
          (much faster)
% test = P(5)*abs(P(4)*(1-exp(-j*qz*P(1)*P(2)))./(1-exp(-
          j*qz*P(1)))+1*exp(-j*qz*(P(1)*P(2)+P(3)))./(1-exp(-
          j*qz*cs))).^2;
```

```
%%  Detector parameters for convolution

% % MRD II Triple Axis - Chi^2 = 9.1238
% %      gfrac dsigma convoffset
% det = [0.834 0.0025 -0.0002];

% MRD II Rocking Detector - Chi^2 = 11.492
%      gfrac dsigma convoffset
det = [0.929 0.0110 -0.0039];

% % Random Guesses for detector - Chi^2 = made up
% %      gfrac dsigma convoffset
% det = [0.929 0.0050 0];

%%  Convolves 'test' function & detector response function (<-
          - can be fit with <XRDdetectorFits.m>)
dsigma = det(2);      % sigma/gamma for detector gauss/lorentz
gbox = exp(-((box-det(3))/det(2)).^2/2);
lbox = 1./(1+(box./det(2)).^2);

gbox = gbox/(sum(gbox)*dt);
lbox = lbox/(sum(lbox)*dt);
gfrac = det(1);       % detector function %gaussian (rest =
          lorentzian)
box = (1-gfrac)*lbox + gfrac*gbox;
test = conv(test,box,'valid');  % Convolution here. 'valid'
          cuts size of box, so it must be made larger above
test = test + P(8);
end
```

REFERENCES

[1] M. Schmidbauer, A. Kwasniewski, and J. Schwarzkopf, “High-precision absolute lattice parameter determination of $SrTiO_3$, $DyScO_3$ and $NdGaO_3$ single crystals,” *Acta Crystallogr. Sect. B Struct. Sci.*, vol. 68, no. 1, pp. 8–14, Feb. 2012.

[2] K. van Benthem, C. Elsässer, and R. H. French, “Bulk electronic structure of SrTiO3: Experiment and theory,” *J. Appl. Phys.*, vol. 90, no. 12, pp. 6156–6164, Dec. 2001.

[3] L. Bjaalie, B. Himmetoglu, L. Weston, A. Janotti, C. G. Van de Walle, and G. C. Van de Walle, “Oxide interfaces for novel electronic applications,” *New J. Phys.*, vol. 16, no. 2, p. 025005, Feb. 2014.

[4] C. L. Wang, “Theories and Methods of First Order Ferroelectric Phase Transitions,” in *Ferroelectrics*, I. Coondoo, Ed. InTech, 2010.

[5] F. Gebhard, “1 . Metal – Insulator Transitions,” in *The Mott Metal-Insulator Transition: Models and Methods*, vol. 48, Springer, 1997, pp. 1–48.

[6] M. Mochizuki and M. Imada, “Orbital physics in the perovskite Ti oxides,” *New J. Phys.*, vol. 6, pp. 154–154, Nov. 2004.

[7] R. J. Cava, B. Batlogg, R. B. van Dover, D. W. Murphy, S. Sunshine, T. Siegrist, J. P. Remeika, E. A. Rietman, S. Zahurak, and G. P. Espinosa, “Bulk superconductivity at 91 K in single-phase oxygen-deficient perovskite $Ba_2YCu_3O_{9-\delta}$,” *Phys. Rev. Lett.*, vol. 58, no. 16, pp. 1676–1679, Apr. 1987.

[8] R. E. Newnham, *Properties of Materials*. Oxford University Press, 2013.

[9] M. Dawber, K. M. Rabe, and J. F. Scott, “Physics of thin-film ferroelectric oxides,” *Rev. Mod. Phys.*, vol. 77, no. 4, pp. 1083–1130, Oct. 2005.

[10] K. A. Muller and H. Burkard, “$SrTiO_3$: An intrinsic quantum paraelectric below 4K,” *Phys. Rev. B*, vol. 19, no. 7, pp. 3593–3602, 1979.

[11] V. Berbenni and A. Marini, “Synthesis of $Sr_xBa_{1-x}TiO_3$ solid solutions from the mechanically activated system $BaCO_3$ - $SrCO_3$ - TiO_2,” *Z. Naturforsch*, vol. 57, no. b, pp. 859–864, 2002.

[12] A. K. Tagantsev, V. O. Sherman, K. F. Astafiev, J. Venkatesh, and N. Setter, “Ferroelectric Materials for Microwave Tunable Applications,” *J. Electroceramics*, vol. 11, no. 1–2, pp. 5–66, 2003.

[13] R. A. York, “Tunable Dielectrics for RF Circuits,” in *Multifunctional Adaptive Microwave Circuits and Systems*, New York, 2009, pp. 1–54.

[14] M. G. S. Ali, N. Z. Elsyed, A. M. Abdel Fattah, and G. A. Ali, “Loss mechanisms in piezoceramic materials,” *J. Comput. Electron.*, vol. 11, no. 2, pp. 196–202, Jun. 2012.

[15] B. Cseppento, T. Berceli, and Z. Szabo, “Comparison of Tunable Microwave Bandpass Filters,” in *2018 11th International Symposium on Communication Systems, Networks & Digital Signal Processing (CSNDSP)*, 2018, pp. 1–3.

[16] G. N. Saddik, D. S. Boesch, S. Stemmer, and R. A. York, “DC electric field tunable bulk acoustic wave solidly mounted resonator using SrTiO3,” *Appl. Phys. Lett.*, vol. 91, no. 4, p. 043501, 2007.

[17] S. Suzuki, T. Yamamoto, H. Suzuki, K. Kawaguchi, K. Takahashi, and Y. Yoshisato,

"Fabrication and characterization of $Ba_{1-x}K_xBiO_3$/Nb-doped $SrTiO_3$ all-oxide-type Schottky junctions," *J. Appl. Phys.*, vol. 81, no. 10, p. 6830, May 1997.

[18] D. R. Chase and R. A. York, "Modeling the capacitive nonlinearity in thin-film BST varactors," *IEEE Trans. Microw. Theory Tech.*, vol. 53, no. 10, pp. 3215–3220, Oct. 2005.

[19] A. K. Tagantsev and K. F. Astafiev, "Quasi-Debye microwave loss in perovskite ferroelectrics," *Integr. Ferroelectr.*, vol. 39, no. 1–4, pp. 251–260, Jan. 2001.

[20] K. F. Astafiev, A. K. Tagantsev, and N. Setter, "Quasi-Debye microwave loss as an intrinsic limitation of microwave performance of tunable components based on $SrTiO_3$ and $Ba_xSr_{1-x}TiO_3$ ferroelectrics," *J. Appl. Phys.*, vol. 97, no. 1, p. 014106, Dec. 2005.

[21] J. D. Baniecki, R. B. Laibowitz, T. M. Shaw, P. R. Duncombe, D. A. Neumayer, D. E. Kotecki, H. Shen, and Q. Y. Ma, "Dielectric relaxation of $Ba_{0.7}Sr_{0.3}TiO_3$ thin films from 1 mHz to 20 GHz," *Appl. Phys. Lett.*, vol. 72, no. 4, p. 498, Jan. 1998.

[22] C. R. Freeze and S. Stemmer, "Role of film stoichiometry and interface quality in the performance of $(Ba,Sr)TiO_3$ tunable capacitors with high figures of merit," *Appl. Phys. Lett.*, vol. 109, no. 19, p. 192904, Nov. 2016.

[23] N. K. Pervez, J. Park, J. Lu, S. Stemmer, and R. A. York, "High Frequency Loss Modeling Using Dielectric Relaxation," *Integr. Ferroelectr.*, vol. 77, pp. 87–92, 2005.

[24] J. Hao, W. Li, J. Zhai, and H. Chen, "Progress in high-strain perovskite piezoelectric ceramics," *Mater. Sci. Eng. R Reports*, vol. 135, pp. 1–57, Jan. 2019.

[25] A. von Hippel, “Ferroelectricity, Domain Structure, and Phase Transitions of Barium Titanate,” *Rev. Mod. Phys.*, vol. 22, no. 3, pp. 221–237, Jul. 1950.

[26] J. Shieh, J. H. Yeh, Y. C. Shu, and J. H. Yen, “Hysteresis behaviors of barium titanate single crystals based on the operation of multiple 90° switching systems,” *Mater. Sci. Eng. B*, vol. 161, no. 1–3, pp. 50–54, Apr. 2009.

[27] M. B. Smith, K. Page, T. Siegrist, P. L. Redmond, E. C. Walter, R. Seshadri, L. E. Brus, and M. L. Steigerwald, “Crystal structure and the paraelectric-to-ferroelectric phase transition of nanoscale BaTiO3,” *J. Am. Chem. Soc.*, vol. 130, no. 22, pp. 6955–6963, 2008.

[28] E. Dul’kin, J. Zhai, and M. Roth, “Relaxor-ferroelectric crossover seen via characteristic temperatures of Ba<x>Sr<1-x>TiO<3> ferroelectrics detected by acoustic emission,” *Phys. status solidi*, p. n/a-n/a, May 2015.

[29] T. Riste, E. J. Samuelsen, K. Otnes, and J. Feder, “Critical behaviour of SrTiO3 near the 105°K phase transition,” *Solid State Commun.*, vol. 9, no. 17, pp. 1455–1458, Sep. 1971.

[30] A. Grzechnik, G. H. Wolf, and P. F. McMillan, “Raman scattering study of SrTiO3 at high pressure,” *J. Raman Spectrosc.*, vol. 28, no. 11, pp. 885–889, Nov. 1997.

[31] M. Guennou, P. Bouvier, J. Kreisel, and D. Machon, “Pressure-temperature phase diagram of SrTiO3 up to 53 GPa,” Oct. 2009.

[32] H. V. Alexandru, C. Berbecaru, A. Ioachim, L. Nedelcu, and A. Dutu, “BST solid solutions, temperature evolution of the ferroelectric transitions,” *Appl. Surf. Sci.*, vol. 253, no. 1, pp. 354–357, Oct. 2006.

[33] M. T. Lanagan, “Microwave dielectric properties of antiferroelectric lead zirconate,” The Pennsylvania State University, 1987.

[34] A. Khalfallaoui, L. Burgnies, K. Blary, G. Vélu, D. Lippens, and J.-C. Carru, “Downscaling at Submicrometer Scale of the Gap Width of Interdigitated Ba<0.5>Sr<0.5>TiO<3> Capacitors,” *IEEE Trans. Ultrason. Ferroelectr. Freq. Control*, vol. 62, no. 2, pp. 247–253, 2015.

[35] C. J. G. Meyers, C. Freeze, S. Stemmer, X. Lan, L. Chau, and R. A. York, “Two-port tunable interdigital capacitors fabricated on low-loss MBE-grown Ba0.29Sr0.71TiO3,” in *2016 IEEE MTT-S International Microwave Symposium (IMS)*, 2016, pp. 1–4.

[36] C. J. G. Meyers, C. R. Freeze, S. Stemmer, and R. A. York, “Effect of BST film thickness on the performance of tunable interdigital capacitors grown by MBE,” *Appl. Phys. Lett.*, vol. 111, no. 26, p. 262903, Dec. 2017.

[37] C. J. G. Meyers, C. R. Freeze, S. Stemmer, and R. A. York, “(Ba,Sr)TiO_3 tunable capacitors with RF commutation quality factors exceeding 6000,” *Appl. Phys. Lett.*, vol. 109, no. 11, p. 112902, Sep. 2016.

[38] W. Chang, J. S. Horwitz, A. C. Carter, J. M. Pond, S. W. Kirchoefer, C. M. Gilmore, and D. B. Chrisey, “The effect of annealing on the microwave properties of $Ba_{0.5}Sr_{0.5}TiO_3$ thin films,” *Appl. Phys. Lett.*, vol. 74, no. 7, p. 1033, Feb. 1999.

[39] Z. Q. Zeng, A. Podpirka, S. W. Kirchoefer, T. J. Asel, and L. J. Brillson, “Direct correlation and strong reduction of native point defects and microwave dielectric loss in air-annealed (Ba,Sr)TiO3,” *Appl. Phys. Lett.*, vol. 106, no. 18, p. 182903, May

2015.

[40] J. Krupka, R. G. Geyer, M. Kuhn, and J. H. Hinken, “Dielectric properties of single crystals of Al<2>O<3>, LaAlO<3>, NdGaO<3>, SrTiO<3>, and MgO at cryogenic temperatures,” *IEEE Trans. Microw. Theory Tech.*, vol. 42, no. 10, pp. 1886–1890, 1994.

[41] N. M. Alford, J. Breeze, X. Wang, S. J. Penn, S. Dalla, S. J. Webb, N. Ljepojevic, and X. Aupi, “Dielectric loss of oxide single crystals and polycrystalline analogues from 10 to 320 K,” *J. Eur. Ceram. Soc.*, vol. 21, no. 15, pp. 2605–2611, Jan. 2001.

[42] T. Konaka, M. Sato, H. Asano, and S. Kubo, “Relative permittivity and dielectric loss tangent of substrate materials for high-T c superconducting film,” *J. Supercond.*, vol. 4, no. 4, pp. 283–288, Aug. 1991.

[43] V. Bovtun, M. Kempa, S. Kamba, V. Pashkov, V. Molchanov, Y. Poplavko, and Y. Yakymenko, “Microwave characterization of dielectric substrates for thin films deposition,” in *2013 IEEE XXXIII International Scientific Conference Electronics and Nanotechnology (ELNANO)*, 2013, pp. 17–20.

[44] D. J. Tao, H. X. Wu, X. D. Xu, R. S. Yan, F. Y. Liu, A. P. B. Sinha, X. P. Jiang, and H. L. Hu, “Czochralski growth of (La,Sr)(Al,Ta)O3 single crystal,” *Opt. Mater. (Amst).*, vol. 23, no. 1–2, pp. 425–428, Jul. 2003.

[45] S. C. Tidrow, A. Tauber, W. D. Wilber, R. T. Lareau, C. D. Brandle, G. W. Berkstresser, A. J. Ven Graitis, D. M. Potrepka, J. I. Budnick, and J. Z. Wu, “New substrates for HTSC microwave devices,” *IEEE Trans. Appl. Supercond.*, vol. 7, no. 2, pp. 1766–1768, Jun. 1997.

[46] S. Schmidt, Y.-W. Ok, D. O. Klenov, J. Lu, S. P. Keane, and S. Stemmer, "Microstructure of Epitaxial $SrTiO_3$/Pt/Ti/ Sapphire Heterostructures," *J. Mater. Res.*, vol. 20, no. 09, pp. 2261–2265, Sep. 2005.

[47] J. Son, J. Cagnon, and S. Stemmer, "Strain relaxation in epitaxial Pt films on (001) $SrTiO_3$," *J. Appl. Phys.*, vol. 106, no. 4, p. 043525, Aug. 2009.

[48] T. J. Jackson and I. P. Jones, "Nanoscale defects and microwave properties of $(BaSr)TiO_3$ ferroelectric thin films," *J. Mater. Sci.*, vol. 44, no. 19, pp. 5288–5296, Jun. 2009.

[49] C. Chen, E. L. Hu, W. V Schoenfeld, and P. M. Petroff, "Metallization-induced damage in III – V semiconductors," *J. Vac. Sci. Technol. B Microelectron. Nanom. Struct.*, vol. 16, no. 6, pp. 3354–3358, 1998.

[50] R. A. York, A. S. Nagra, P. Periaswamy, O. Auciello, S. K. Streiffer, and J. Im, "Synthesis and characterization of $(Ba_xSr_{1-x})Ti_{1+y}O_{3+z}$ thin films and integration into microwave varactors and phase shifters," *Integr. Ferroelectr.*, vol. 34, no. 1–4, 2001.

[51] J. Im, O. Auciello, P. K. Baumann, S. K. Streiffer, D. Y. Kaufman, and A. R. Krauss, "Composition-control of magnetron-sputter-deposited $(Ba_xSr_{1-x})Ti_{1+y}O_{3+z}$ thin films for voltage tunable devices," *Appl. Phys. Lett.*, vol. 76, no. 2000, pp. 625–627, 2000.

[52] N. K. Pervez, "Investigation of Loss Mechanisms in Thin Film Barium Strontium Titanate Capacitors," University of California - Santa Barbara, 2006.

[53] M. Didomenico, D. A. Johnson, and R. H. Pantell, "Ferroelectric Harmonic

Generator and the Large-Signal Microwave Characteristics of a Ferroelectric Ceramic," *J. Appl. Phys.*, vol. 33, no. 5, pp. 1697–1706, May 1962.

[54] O. G. Vendik, E. K. Hollmann, A. B. Kozyrev, and A. M. Prudan, "Ferroelectric Tuning of Planar and Bulk Microwave Devices," *J. Supercond.*, vol. 12, no. 2, pp. 325–338, 1999.

[55] T. Ayguavives, A. Tombak, J.-P. Maria, G. T. Stauf, C. Ragaglia, J. Roeder, A. Mortazawi, and A. I. Kingon, "Physical properties of (Ba,Sr)TiO_3 thin films used for integrated capacitors in microwave applications," in *ISAF 2000. Proceedings of the 2000 12th IEEE International Symposium on Applications of Ferroelectrics (IEEE Cat. No.00CH37076)*, 2000, vol. 1, pp. 365–368.

[56] E. Mikheev, B. D. Hoskins, D. B. Strukov, and S. Stemmer, "Resistive switching and its suppression in Pt/Nb:$SrTiO_3$ junctions.," *Nat. Commun.*, vol. 5, p. 3990, Jan. 2014.

[57] E. Mikheev, A. P. Kajdos, A. J. Hauser, and S. Stemmer, "Electric field-tunable $Ba_xSr_{1-x}TiO_3$ films with high figures of merit grown by molecular beam epitaxy," *Appl. Phys. Lett.*, vol. 101, no. 25, p. 252906, Dec. 2012.

[58] C.-H. Lee, N. D. Orloff, T. Birol, Y. Zhu, V. Goian, E. Rocas, R. Haislmaier, E. Vlahos, J. A. Mundy, L. F. Kourkoutis, Y. Nie, M. D. Biegalski, J. Zhang, M. Bernhagen, N. A. Benedek, Y. Kim, J. D. Brock, R. Uecker, X. X. Xi, V. Gopalan, D. Nuzhnyy, S. Kamba, D. a Muller, I. Takeuchi, J. C. Booth, C. J. Fennie, and D. G. Schlom, "Exploiting dimensionality and defect mitigation to create tunable microwave dielectrics.," *Nature*, vol. 502, no. 7472, pp. 532–6, Oct. 2013.

[59] R. Schafranek, S. Payan, M. Maglione, and A. Klein, "Barrier height at (Ba,Sr)TiO_3/Pt interfaces studied by photoemission," *Phys. Rev. B*, vol. 77, no. 19, p. 195310, May 2008.

[60] W.-J. Lee, H. J. Kim, J. Kang, D. H. Jang, T. H. Kim, J. H. Lee, and K. H. Kim, "Transparent Perovskite Barium Stannate with High Electron Mobility and Thermal Stability," *Annu. Rev. Mater. Res.*, vol. 47, no. 1, pp. 391–423, Jul. 2017.

[61] P. Singh, B. J. Brandenburg, C. P. Sebastian, P. Singh, S. Singh, D. Kumar, and O. Parkash, "Electronic Structure, Electrical and Dielectric Properties of $BaSnO_3$ below 300 K," *Jpn. J. Appl. Phys.*, vol. 47, no. 5, pp. 3540–3545, May 2008.

[62] A. Ohtomo, K. Tamura, K. Saikusa, K. Takahashi, T. Makino, Y. Segawa, H. Koinuma, and M. Kawasaki, "Single crystalline ZnO films grown on lattice-matched ScAlMgO4(0001) substrates," *Appl. Phys. Lett.*, vol. 75, no. 17, p. 2635, Oct. 1999.

[63] R. L. Weiher, "Electrical Properties of Single Crystals of Indium Oxide," *J. Appl. Phys.*, vol. 33, no. 9, pp. 2834–2839, Sep. 1962.

[64] S. Ismail-Beigi, F. J. Walker, S.-W. Cheong, K. M. Rabe, and C. H. Ahn, "Alkaline earth stannates: The next silicon?," *APL Mater.*, vol. 3, no. 6, p. 062510, Jun. 2015.

[65] T. Schumann, S. Raghavan, K. Ahadi, H. Kim, and S. Stemmer, "Structure and optical band gaps of (Ba,Sr)SnO3 films grown by molecular beam epitaxy," *J. Vac. Sci. Technol. A Vacuum, Surfaces, Film.*, vol. 34, no. 5, p. 050601, Sep. 2016.

[66] Z. Lebens-Higgins, D. O. O. Scanlon, H. Paik, S. Sallis, Y. Nie, M. Uchida, N. F. F. Quackenbush, M. J. J. Wahila, G. E. E. Sterbinsky, D. A. Arena, J. C. C. Woicik, D.

G. G. Schlom, and L. F. J. F. J. Piper, “Direct Observation of Electrostatically Driven Band Gap Renormalization in a Degenerate Perovskite Transparent Conducting Oxide,” *Phys. Rev. Lett.*, vol. 116, no. 2, p. 027602, Jan. 2016.

[67] K. Krishnaswamy, B. Himmetoglu, Y. Kang, A. Janotti, and C. G. Van de Walle, “First-principles analysis of electron transport in BaSnO3,” *Phys. Rev. B*, vol. 95, no. 20, p. 205202, May 2017.

[68] S. James Allen, S. Raghavan, T. Schumann, K.-M. Law, and S. Stemmer, “Conduction band edge effective mass of La-doped $BaSnO_3$,” *Appl. Phys. Lett.*, vol. 108, no. 25, p. 252107, Jun. 2016.

[69] B. C. Luo, X. S. Cao, K. X. Jin, and C. L. Chen, “Determination of the effective mass and nanoscale electrical transport in La-doped BaSnO3 thin films,” *Curr. Appl. Phys.*, vol. 16, no. 1, pp. 20–23, Jan. 2016.

[70] W. Nunn, A. Prakash, A. Bhowmik, R. Haislmaier, J. Yue, J. M. Garcia Lastra, and B. Jalan, “Frequency- and temperature-dependent dielectric response in hybrid molecular beam epitaxy-grown BaSnO3 films,” *APL Mater.*, vol. 6, no. 6, p. 066107, Jun. 2018.

[71] L. Weston, L. Bjaalie, K. Krishnaswamy, and C. G. Van de Walle, “Origins of n-type doping difficulties in perovskite stannates,” *Phys. Rev. B*, vol. 97, no. 5, p. 054112, Feb. 2018.

[72] H. M. Kim, U. Kim, C. Park, H. Kwon, and K. Char, “Thermally stable pn-junctions based on a single transparent perovskite semiconductor $BaSnO_3$,” *APL Mater.*, vol. 4, no. 5, p. 056105, May 2016.

[73] H. M. Ng, D. Doppalapudi, T. D. Moustakas, N. G. Weimann, and L. F. Eastman, "The role of dislocation scattering in n-type GaN films," *Appl. Phys. Lett.*, vol. 73, no. 6, p. 821, Aug. 1998.

[74] H. J. Kim, U. Kim, H. M. Kim, T. H. Kim, H. S. Mun, B.-G. Jeon, K. T. Hong, W.-J. Lee, C. Ju, K. H. Kim, and K. Char, "High Mobility in a Stable Transparent Perovskite Oxide," *Appl. Phys. Express*, vol. 5, no. 6, p. 061102, May 2012.

[75] H. J. Kim, U. Kim, T. H. Kim, J. Kim, H. M. Kim, B. G. Jeon, W. J. Lee, H. S. Mun, K. T. Hong, J. Yu, K. Char, and K. H. Kim, "Physical properties of transparent perovskite oxides (Ba,La)$SnO_3$with high electrical mobility at room temperature," *Phys. Rev. B - Condens. Matter Mater. Phys.*, vol. 86, no. 16, 2012.

[76] H. Paik, Z. Chen, E. Lochocki, A. Seidner H., A. Verma, N. Tanen, J. Park, M. Uchida, S. Shang, B.-C. Zhou, M. Brützam, R. Uecker, Z.-K. Liu, D. Jena, K. M. Shen, D. A. Muller, and D. G. Schlom, "Adsorption-controlled growth of La-doped $BaSnO_3$ by molecular-beam epitaxy," *APL Mater.*, vol. 5, no. 11, p. 116107, Nov. 2017.

[77] A. Prakash, P. Xu, X. Wu, G. Haugstad, X. Wang, and B. Jalan, "Adsorption-controlled growth and the influence of stoichiometry on electronic transport in hybrid molecular beam epitaxy-grown $BaSnO_3$ films," *J. Mater. Chem. C*, vol. 5, no. 23, pp. 5730–5736, 2017.

[78] S. Raghavan, T. Schumann, H. Kim, J. Y. Zhang, T. A. Cain, and S. Stemmer, "High-mobility $BaSnO_3$ grown by oxide molecular beam epitaxy," *APL Mater.*, vol. 4, no. 1, p. 016106, Jan. 2016.

[79] C. Hamaguchi, *Basic Semiconductor Physics*, 1st ed. Berlin: Springer, 2010.

[80] A. Prakash, P. Xu, A. Faghaninia, S. Shukla, J. W. Ager, C. S. Lo, and B. Jalan, "Wide bandgap BaSnO3 films with room temperature conductivity exceeding 104 S cm−1," *Nat. Commun.*, vol. 8, p. 15167, May 2017.

[81] A. Verma, A. P. Kajdos, T. A. Cain, S. Stemmer, and D. Jena, "Intrinsic Mobility Limiting Mechanisms in Lanthanum-Doped Strontium Titanate," *Phys. Rev. Lett.*, vol. 112, no. 21, p. 216601, May 2014.

[82] H. Sakaki, T. Noda, K. Hirakawa, M. Tanaka, and T. Matsusue, "Interface roughness scattering in GaAs/AlAs quantum wells," *Appl. Phys. Lett.*, vol. 51, no. 23, pp. 1934–1936, Dec. 1987.

[83] C. T. Sah, T. H. Ning, and L. L. Tschopp, "The scattering of electrons by surface oxide charges and by lattice vibrations at the silicon-silicon dioxide interface," *Surf. Sci.*, vol. 32, no. 3, pp. 561–575, Sep. 1972.

[84] C. A. Niedermeier, S. Rhode, K. Ide, H. Hiramatsu, H. Hosono, T. Kamiya, and M. A. Moram, "Electron effective mass and mobility limits in degenerate perovskite stannate $BaSnO_3$," *Phys. Rev. B*, vol. 95, no. 16, p. 161202, Apr. 2017.

[85] L. J. van der Pauw, "A method of measuring specific resistivity and Hall effect of discs of arbitrary shapes," *Philips Res. Reports*, vol. 13, no. 1, pp. 1–9, 1958.

[86] L. J. van der Pauw, "A method of measuring the resistivity and Hall coefficient on lamellae of arbitrary shape," *Philips Tech. Rev.*, vol. 20, pp. 220–224, 1958.

[87] "Hall Effect Measurements | NIST." [Online]. Available: https://www.nist.gov/pml/engineering-physics-division/popular-links/hall-

effect. [Accessed: 28-Jan-2019].

[88] L. V. Prokof'eva, A. A. Shabaldin, V. A. Korchagin, S. A. Nemov, and Y. I. Ravich, "Lorentz number and Hall factor in degenerate semiconductors during resonance scattering of charge carriers," *Semiconductors*, vol. 42, no. 10, pp. 1161–1170, Oct. 2008.

[89] J. F. Lin, S. S. Li, L. C. Linares, and K. W. Teng, "Theoretical analysis of hall factor and hall mobility in p-type silicon," *Solid. State. Electron.*, vol. 24, no. 9, pp. 827–833, Sep. 1981.

[90] R. Chwang, B. J. Smith, and C. R. Crowell, "Contact size effects on the van der Pauw method for resistivity and Hall coefficient measurement," *Solid. State. Electron.*, vol. 17, no. 12, pp. 1217–1227, Dec. 1974.

[91] O. Shoron, M. Boucherit, C. A. Jackson, T. A. Cain, M. L. C. Buffon, C. Polchinski, S. Stemmer, and S. Rajan, "Modulation of over 1014 cm-2 electrons at the SrTiO3/GdTiO3 heterojunction," in *Device Research Conference - Conference Digest, DRC*, 2014, pp. 13–14.

[92] C. Wang, C. R. Freeze, N. K. Kalarickal, J. Cheng, Z. Xia, O. F. Shoron, W. Lu, S. Stemmer, and S. Rajan, "Extreme Dielectric Constant Engineered Perovskite Oxide Heterostructure Field Effect Transistors," *Under Rev.*

[93] U. K. Mishra and J. Singh, *Semiconductor Device Physics and Design*. Dordrecht: Springer Netherlands, 2007.

[94] K. Krishnaswamy, L. Bjaalie, B. Himmetoglu, A. Janotti, L. Gordon, and C. G. Van de Walle, "$BaSnO_3$ as a channel material in perovskite oxide heterostructures,"

Appl. Phys. Lett., vol. 108, no. 8, p. 083501, Feb. 2016.

[95] S. A. Chambers, T. C. Kaspar, A. Prakash, G. Haugstad, and B. Jalan, "Band alignment at epitaxial BaSnO3/SrTiO3(001) and BaSnO3/LaAlO3(001) heterojunctions," *Appl. Phys. Lett.*, 2016.

[96] J. Yue, A. Prakash, M. C. Robbins, S. J. Koester, and B. Jalan, "Depletion Mode MOSFET Using La-Doped BaSnO3 as a Channel Material," *ACS Appl. Mater. Interfaces*, vol. 10, no. 25, pp. 21061–21065, Jun. 2018.

[97] J. Y. Tsao, *Materials Fundamentals of Molecular Beam Epitaxy*. San Diego, CA: Academic Press, Inc., 1993.

[98] C. . Theis, J. Yeh, D. . Schlom, M. . Hawley, and G. . Brown, "Adsorption-controlled growth of PbTiO3 by reactive molecular beam epitaxy," *Thin Solid Films*, vol. 325, no. 1–2, pp. 107–114, Jul. 1998.

[99] J. H. Haeni, C. D. Theis, and D. G. Schlom, "RHEED Intensity Oscillations for the Stoichiometric Growth of SrTiO3 Thin Films by Reactive Molecular Beam Epitaxy," *J. Electroceramics*, vol. 4, no. 2–3, pp. 385–391.

[100] B. Jalan, P. Moetakef, and S. Stemmer, "Molecular beam epitaxy of $SrTiO_3$ with a growth window," *Appl. Phys. Lett.*, vol. 95, no. 3, p. 032906, 2009.

[101] B. Jalan, S. J. Allen, G. E. Beltz, P. Moetakef, and S. Stemmer, "Enhancing the electron mobility of $SrTiO_3$ with strain," *Appl. Phys. Lett.*, vol. 98, no. 13, p. 132102, 2011.

[102] "Supplemental Information."

[103] A. P. Kajdos, D. G. Ouellette, T. A. Cain, and S. Stemmer, "Two-dimensional

electron gas in a modulation-doped SrTiO3/Sr(Ti, Zr)O3 heterostructure," *Appl. Phys. Lett.*, vol. 103, no. 8, 2013.

[104] M. Y. Tsai, M. E. White, and J. S. Speck, "Plasma-assisted molecular beam epitaxy of SnO2 on TiO2," *J. Cryst. Growth*, vol. 310, no. 18, pp. 4256–4261, Aug. 2008.

[105] A. Prakash, J. Dewey, H. Yun, J. S. Jeong, K. A. Mkhoyan, and B. Jalan, "Hybrid molecular beam epitaxy for the growth of stoichiometric $BaSnO_3$," *J. Vac. Sci. Technol. A Vacuum, Surfaces, Film.*, vol. 33, no. 6, 2015.

[106] M. A. Mäki-Jaskari and T. T. Rantala, "Possible structures of nonstoichiometric tin oxide: the composition Sn_2O_3," *Model. Simul. Mater. Sci. Eng.*, vol. 12, no. 1, pp. 33–41, Jan. 2004.

[107] F. Gauzzi, B. Verdini, A. Maddalena, and G. Principi, "X-ray diffraction and mössbauer analyses of SnO disproportionation products," *Inorganica Chim. Acta*, vol. 104, no. 1, pp. 1–7, Oct. 1985.

[108] H. Giefers, F. Porsch, and G. Wortmann, "Kinetics of the disproportionation of SnO," *Solid State Ionics*, vol. 176, no. 1–2, pp. 199–207, Jan. 2005.

[109] F. Gauzzi and B. Verdini, "Analysis ofin-situ SnO disproportionation," *J. Mater. Sci. Lett.*, vol. 4, no. 12, pp. 1492–1494, 1985.

[110] M. S. Moreno, G. Punte, G. Rigotti, R. C. Mercader, A. D. Weisz, and M. A. Blesa, "Kinetic study of the disproportionation of tin monoxide," *Solid State Ionics*, vol. 144, no. 1–2, pp. 81–86, Sep. 2001.

[111] T. Watson, "Personal Communication." 2019.

[112] A. P. Kajdos and S. Stemmer, "Surface reconstructions in molecular beam epitaxy

of $SrTiO_3$," *Appl. Phys. Lett.*, vol. 105, no. 19, p. 191901, Nov. 2014.

[113] D. J. Keeble, B. Jalan, L. Ravelli, W. Egger, G. Kanda, and S. Stemmer, "Suppression of vacancy defects in epitaxial La-doped SrTiO<3> films," *Appl. Phys. Lett.*, vol. 99, no. 23, p. 232905, 2011.

[114] Y. Matsubara, K. S. Takahashi, Y. Tokura, and M. Kawasaki, "Single-crystalline $BaTiO_3$ films grown by gas-source molecular beam epitaxy," *Appl. Phys. Express*, vol. 7, no. 12, p. 125502, Dec. 2014.

[115] A. P. Kajdos, "Modulation-doped SrTiO3/SrTi1-xZrxO3 heterostructures," 2015.

[116] C. Basceri, "Electrical and dielectric properties of (Ba,Sr)TiO_3 thin film capacitors for ultra-high density dynamic random access memories," North Carolina State University, 1997.

[117] D. S. Boesch, J. Son, J. M. LeBeau, J. Cagnon, and S. Stemmer, "Thickness Dependence of the Dielectric Properties of Epitaxial $SrTiO_3$ Films on (001)Pt/$SrTiO_3$," *Appl. Phys. Express*, vol. 1, no. 9, p. 091602, Sep. 2008.

[118] B. Jalan, J. Cagnon, T. E. Mates, and S. Stemmer, "Analysis of carbon in $SrTiO_3$ grown by hybrid molecular beam epitaxy," *J. Vac. Sci. Technol. A Vacuum, Surfaces, Film.*, vol. 27, no. 6, p. 1365, 2009.

[119] C. Basceri, S. K. Streiffer, A. I. Kingon, and R. Waser, "The dielectric response as a function of temperature and film thickness of fiber-textured (Ba,Sr)TiO_3 thin films grown by chemical vapor deposition," *J. Appl. Phys.*, vol. 82, no. 5, p. 2497, Sep. 1997.

[120] J. M. LeBeau, R. Engel-Herbert, B. Jalan, J. J. Cagnon, P. Moetakef, S. Stemmer,

and G. B. Stephenson, "Stoichiometry optimization of homoepitaxial oxide thin films using x-ray diffraction," *Appl. Phys. Lett.*, vol. 95, no. 14, p. 142905, 2009.

[121] H. C. Li, W. Si, A. D. West, and X. X. Xi, "Near single crystal-level dielectric loss and nonlinearity in pulsed laser deposited $SrTiO_3$ thin films," *Appl. Phys. Lett.*, vol. 73, no. 2, pp. 190–192, 1998.

[122] J. T. Dawley and P. G. Clem, "Dielectric properties of random and <100> oriented $SrTiO_3$ and $(Ba,Sr)TiO_3$ thin films fabricated on <100> nickel tapes," *Appl. Phys. Lett.*, vol. 81, no. 16, pp. 3028–3030, 2002.

[123] W. Chang, S. W. Kirchoefer, J. M. Pond, J. S. Horwitz, and L. Sengupta, "Strain-relieved $Ba_{0.6}Sr_{0.4}TiO_3$ thin films for tunable microwave applications," *J. Appl. Phys.*, vol. 92, no. 3, p. 1528, 2002.

[124] B. Su, J. E. Holmes, C. Meggs, and T. W. Button, "Dielectric and microwave properties of barium strontium titanate (BST) thick films on alumina substrates," *J. Eur. Ceram. Soc.*, vol. 23, no. 14, pp. 2699–2703, 2003.

[125] N. K. Pervez, P. J. Hansen, and R. A. York, "High tunability barium strontium titanate thin films for rf circuit applications," in *Applied Physics Letters*, 2004, vol. 85, no. 19, pp. 4451–4453.

[126] M. E. Lines and A. M. Glass, *Principles and Applications of Ferroelectrics and Related Materials*. Oxford: Oxford University Press, 2001.

[127] N. K. Pervez and R. A. York, "Geometry-Dependent Quality Factors in $Ba_{0.5}Sr_{0.5}TiO_3$ Parallel-Plate Capacitors," *IEEE Trans. Microw. Theory Tech.*, vol. 55, no. 2, pp. 410–417, 2007.

[128] Agilent, *Agilent Impedance Measurement Handbook: A guide to measurement technology and techniques*, 4th ed. 2009.

[129] L. W. Finger, D. E. Cox, and A. P. Jephcoat, “A correction for powder diffraction peak asymmetry due to axial divergence,” *J. Appl. Crystallogr.*, vol. 27, no. 6, pp. 892–900, Dec. 1994.

[130] C. J. G. Meyers, C. R. Freeze, S. Stemmer, and R. A. York, “Voltage-Tunable Parallel-Plate Capacitors Fabricated on Low-Loss MBE-Grown BST,” in *2018 IEEE/MTT-S International Microwave Symposium - IMS*, 2018, pp. 739–742.

[131] F. Bastiman, “MBE Blog Contents Page | Dr. Faebian Bastiman.” [Online]. Available: https://faebianbastiman.wordpress.com/mbe-blog-contents-page/. [Accessed: 21-Oct-2018].

[132] D. O. Scanlon, “Defect engineering of $BaSnO_3$ for high-performance transparent conducting oxide applications,” *Phys. Rev. B*, vol. 87, no. 16, p. 161201, Apr. 2013.

[133] B. Jalan, R. Engel-Herbert, N. J. Wright, and S. Stemmer, “Growth of high-quality $SrTiO_3$ films using a hybrid molecular beam epitaxy approach,” *J. Vac. Sci. Technol. A Vacuum, Surfaces, Film.*, vol. 27, no. 3, p. 461, 2009.

[134] B. Eifert, M. Becker, C. T. Reindl, M. Giar, L. Zheng, A. Polity, Y. He, C. Heiliger, and P. J. Klar, “Raman studies of the intermediate tin-oxide phase,” *Phys. Rev. Mater.*, vol. 1, p. 14602, 2017.

[135] A. Seko, A. Togo, F. Oba, and I. Tanaka, “Structure and Stability of a Homologous Series of Tin Oxides,” *Phys. Rev. Lett.*, vol. 100, no. 4, p. 045702, Jan. 2008.

[136] S. M. Madelung O., Rössler U., “Barium oxide (BaO) crystal structure, lattice

parameters, thermal expansion," in *II-VI and I-VII Compounds; Semimagnetic Compounds*, O. Madelung, U. Rössler, and M. Schulz, Eds. Berlin, Heidelberg: Springer Berlin Heidelberg, 1999, pp. 1–3.

[137] J. L. Jorda and T. K. Jondo, "Barium oxides: equilibrium and decomposition of BaO2," *J. Alloys Compd.*, vol. 327, no. 1–2, pp. 167–177, Aug. 2001.

[138] F. A. Cotton, *Progress in Inorganic Chemistry, Volume 8*. John Wiley & Sons, Inc., 2009.

[139] B. E. Warren, *X-ray diffraction*. Dover Publications, 1990.

[140] E. Mikheev, B. Himmetoglu, A. P. Kajdos, P. Moetakef, T. A. Cain, C. G. Van De Walle, and S. Stemmer, "Limitations to the room temperature mobility of two- and three-dimensional electron liquids in $SrTiO_3$," *Appl. Phys. Lett.*, vol. 106, no. 6, 2015.

[141] A. Ohtomo and H. Y. Hwang, "Surface depletion in doped $SrTiO_3$ thin films," *Appl. Phys. Lett.*, vol. 84, no. 10, p. 1716, Mar. 2004.

[142] A. Able, W. Wegscheider, K. Engl, and J. Zweck, "Growth of crack-free GaN on Si(1 1 1) with graded AlGaN buffer layers," *J. Cryst. Growth*, vol. 276, no. 3–4, pp. 415–418, Apr. 2005.

[143] K. Cheng, M. Leys, S. Degroote, B. Van Daele, S. Boeykens, J. Derluyn, M. Germain, G. Van Tendeloo, J. Engelen, and G. Borghs, "Flat GaN epitaxial layers grown on Si(111) by metalorganic vapor phase epitaxy using step-graded AlGaN intermediate layers," *J. Electron. Mater.*, vol. 35, no. 4, pp. 592–598, Apr. 2006.

[144] T. Wang, L. R. Thoutam, A. Prakash, W. Nunn, G. Haugstad, and B. Jalan, "Defect-

driven localization crossovers in MBE-grown La-doped $SrSnO_3$ films," *Phys. Rev. Mater.*, vol. 1, no. 6, p. 061601, Nov. 2017.

[145] D. J. Singh, Q. Xu, and K. P. Ong, "Strain effects on the band gap and optical properties of perovskite $SrSnO_3$ and $BaSnO_3$," *Appl. Phys. Lett.*, vol. 104, no. 1, p. 011910, Jan. 2014.

[146] R. J. D. Tilley, "An electron microscope study of perovskite-related oxides in the Sr-Ti-O system," *J. Solid State Chem.*, vol. 21, no. 4, pp. 293–301, Aug. 1977.